

MATERIAL CHANGES OF BONE FOLLOWING ISCHEMIA
OF THE IMMATURE FEMORAL HEAD

by

OLUMIDE O. ARUWAJOYE

Presented to the Faculty of the Graduate School of
The University of Texas at Arlington in Partial Fulfillment
of the Requirements
for the Degree of

DOCTOR OF PHILOSOPHY
THE UNIVERSITY OF TEXAS AT ARLINGTON

December 2015

Copyright © by Olumide O. Aruwajoye 2015

All Rights Reserved



Acknowledgements

I am deeply grateful for my advisors, Dr. Pranesh Aswath and Dr. Harry Kim for their patience, support, and guidance throughout my research studies. I am also grateful for my committee members Dr. Fuqiang Liu, Dr. Liping Tang, and Dr. Kyungsuk Yum for their time, insight, and interest in the study.

I would also like to thank Texas Scottish Rite Hospital for its countless resources and helpful staff. I am very appreciative of Reuel Cornelia and Richard Banlaygas for technical expertise with related histology for this study. In addition, I would like to thank Keith Condon at Indiana University for microcrack sample preparation, and the technical assistance from staff at Canadian Light Source where the XANES experiments were performed. I am also grateful for the technical assistance and characterization made available at the Characterization Center for Materials and Biology at the University of Texas at Arlington and Texas A&M University Baylor College of Dentistry.

I would also like to thank all of the members of Dr. Aswath's and Dr. Kim's lab that have been a great resource throughout the course of my research. I would like to acknowledge Felipe Monte, Mihir Patel, Ami Shah, Vibhu Sharma, and Megen Velten for their support. In addition, I am also grateful to Mrs. Marjorie Ehrmann for her helpful review of my writing.

Finally, I would to thank my family and friends for their continual support.

November 23, 2015

Abstract

MATERIAL CHANGES OF BONE FOLLOWING ISCHEMIA
OF THE IMMATURE FEMORAL HEAD

Olumide O. Aruwajoye, PhD

The University of Texas at Arlington, 2015

Supervising Professor: Pranesh B. Aswath

Legg-Calvé-Perthes disease (LCPD) is a childhood hip disorder resulting from the loss of blood flow to the femoral head. In severe cases of the disease, the femoral head can develop a flattening deformity; additionally, if the disease is diagnosed at a later stage, it leaves most patients to develop early osteoarthritis of the hip. Due to a lack of pathological specimen from patients, an experimental piglet model of femoral head ischemia was developed. The model closely follows the radiographic changes seen in LCPD patients, where there is subchondral fracture, resorption, and a flattening deformity of the femoral head. After ischemia, the trabecular bone tissue in the femoral head is hypothesized to undergo material changes that predispose it to possible subchondral fracture and increased resorption. The increased resorption outpaces new bone formation resulting in overall bone loss. Successful treatment is largely dependent on maintaining sphericity while the femoral head is revascularized with new blood supply and reossified with new bone.

In order to elucidate the pathological events from femoral head ischemia, the material (i.e. nanomechanical and mineral) changes in trabecular bone were investigated. This study consists of three parts: 1) the avascular stage where there is no resorption or revascularization and prior to any fracture, 2) the revascular stage where there is

extensive resorption of the bone, and 3) the revascular stage where the femoral head has been treated with anabolic and anti-resorptive agents to restore the balance of bone resorption and bone formation. The bone was characterized using optical and fluorescence microscopy, nanoindentation, scanning electron microscopy, Raman spectroscopy, and X-ray absorbance near edge structure spectroscopy. Results show the nanoindentation properties of the trabecular bone are increased in the early stage of ischemic osteonecrosis of the immature femoral head and make it more susceptible to microcrack formation, while balanced repair aided by anabolic and anti-resorptive treatments help normalize the material properties.

This study provides a greater understanding of ischemia of the developing femoral head and the role of treatment on the material properties of bone. It identifies microstructural damage and compositional variance in ischemic bone that has been previously unavailable. In addition, it provides valuable insight on the quality of bone after treatment, and potentially provides further evidence for the use of anabolic and anti-resorptive treatments in LCPD patients.

Table of Contents

Acknowledgements	iii
Abstract	iv
List of Illustrations	x
List of Tables	xvi
Chapter 1 Introduction.....	1
1.1 Specific aims of the dissertation	2
1.1.1 Rationale	2
1.1.2 Aim 1	4
1.1.3 Aim 2	5
1.1.4 Aim 3	5
1.2 Structure of the dissertation.....	6
Chapter 2 2.1 Background	7
2.2 Hip Anatomy and Complications during Development.....	7
2.3 Bone vascularization	9
2.4 Cortical and trabecular bone	10
2.5 Composition and mineralization of bone	14
2.5.1 Collagen	14
2.5.2 Non-collagenous proteins and growth factors.....	15
2.5.3 Osteoblasts, osteoclasts, and osteocytes	18
2.6 Microdamage and fracture in bone.....	19
2.7 Juvenile osteonecrosis of the femoral head	21
2.7.1 Treatment of Legg-Calvé-Perthes Disease	22
2.7.2 Pathology of Legg-Calvé-Perthes Disease and Experimental Animal Model.....	23

2.8 Material Characterization Techniques	25
2.8.1 Nanomechanical Testing	26
2.8.2 Quantitative backscattered electron imaging	28
2.8.3 Spectroscopy	31
2.8.3.1 XANES	31
2.8.3.2 Raman	33
Chapter 3 Microcrack Density and Nanomechanical Properties in the	
Subchondral Region of the Immature Piglet Femoral Head following Ischemic	
Osteonecrosis	37
3.1 Abstract	37
3.1 Introduction	38
3.3 Materials and Methods	39
3.3.1 Histological Assessment	40
3.3.2 Microdamage Assessment	41
3.3.3 Quantitative Backscattered Electron Imaging	42
3.3.4 Nanoindentation	42
3.3.5 Statistical Analysis	45
3.4 Results	45
3.5 Discussion	56
Chapter 4 Bone Apatite Composition of Necrotic Trabecular Bone in the	
Femoral Head of Immature Piglets	60
4.1 Abstract	60
4.2 Introduction	60
4.3 Methods and Materials	62
4.3.1 Surgical induction of osteonecrosis	62

4.3.2 Histology, Micro-CT and Scanning Electron Microscopy (SEM)	63
4.3.3 X-ray Absorption Near Edge Structure (XANES)	63
4.3.4 Raman Spectroscopy	65
4.3.5 Statistical Analysis.....	65
4.4 Results	65
4.4.1 MicroCT, Histology and Scanning Electron Microscopy (SEM)	65
4.4.2 XANES analysis	68
4.4.2.1 Phosphorous L-edge FY and K-edge TEY spectra of model compounds and normal, necrotic, and newly ossified regions of the femoral head	69
4.4.2.2 Oxygen K-edge TEY and FY spectra of model compounds and normal, necrotic, and newly ossified regions of the femoral head.....	72
4.4.3 Raman Spectroscopy	75
4.5 Discussion	76
4.6 Conclusion	79
Chapter 5 Material properties of femoral head treated with local administration of anti-resorptive and bone anabolic agents following the induction of ischemic osteonecrosis: Experimental Investigation in Immature	
Pigs	81
5.1 Abstract.....	81
5.2 Introduction	82
5.3 Materials and Methods	84
5.3.1 Surgical induction of osteonecrosis.....	84
5.3.2 Histology.....	84
5.3.3 Quantitative Backscattered Electron Imaging (qBEI)	85

5.3.4 Raman Spectroscopy	86
5.3.5 Nanoindentation	86
5.3.6 Statistical Analysis.....	87
5.4 Results.....	88
5.5 Discussion	96
Chapter 6 Summary and Conclusion	100
References.....	104
Biographical Information	129

List of Illustrations

Figure 2.1 A schematic of a normal developing femoral head with related blood supply. Figure reproduced and modified from [1].....	8
Figure 2.2 (a) A femur with a (b) micro-CT reconstruction of a cylindrical specimen of extracted trabecular bone from the femoral head together with a (c) histological image of a diaphyseal mid shaft section and a magnification of cortical osteonal structure. Figure reproduced and modified from [2]	11
Figure 2.3 A collagen fibril found within bone which is composed of collagen protein molecules (tropocollagen) formed from three chains of amino acids and nanocrystals of hydroxyapatite (HA), and linked by an organic phase to form fibril arrays. Figure reproduced and modified from [3]	12
Figure 2.4 Three types of microdamage indicated by arrows. Left to right is microcrack damage, cross-hatching damage, and diffuse damage. Image reproduced from [4]	21
Figure 2.5 The various radiographic stages of the disease with an increasing flattening deformity and resorption/fragmentation over a one to two year period with eventual re- ossification and healing. The boxed regions indicate the affected femoral head. Image reproduced from Texas Scottish Rite Hospital.	24
Figure 2.6 The various radiographic stages of increasing flattening deformity and increasing areas of resorption/fragmentation at 3, 4, 6, and 8 weeks post ischemia induction of the femoral head in the experimental model with piglets. The figure was reproduced from [5].....	24
Figure 2.7 The load displacement data from an indentation experiment. The measure parameters shown are P_{max} , the peak indentation load, S , the initial unloading stiffness h_{max} , the indenter displacement at peak load, and, h_f , the final depth of the contact impression. Reproduced from [6].....	28

Figure 2.8 The calibration line based on standards of carbon (C) and aluminum (Al). Measured grey levels (GL) were verified with calculated a mean atomic number (Z) for magnesium fluoride (MgF₂), and fluorapatite (FA). Hydroxyapatite = HA, BE=Backscattered Electron. Reproduced from [7]. 30

Figure 2.9 An X-ray absorbance near edge structure (XANES) spectrum of Ti K-edge of Ba₂TiO₄ with the pre-edge, edge, and XANES regions identified. Image reproduced from [8]. 32

Figure 3.1 A scanning probe microscopy image with a dashed line depicting the plastic-bone interface. The plastic is on the left and the bony area is on the right. The numbers on the image indicate the reduced modulus in GPa units obtained at each respective location. 44

Figure 3.2 (A) The subchondral region of normal and ischemic bone stained with (H&E). An arrow indicates osteoblast lining the trabecular bone of the normal subchondral region. The ischemic side shows a lack of osteoblast lining the trabeculae. B) Normal and ischemic subchondral regions assessed with terminal deoxynucleotidyl transferase mediated dUTP biotin nick end labeling (TUNEL) assay. The normal subchondral region shows a negative TUNEL staining whereas the ischemic bone shows diffuse TUNEL staining of the cells in the bone and the marrow space. The original magnification is 100X (scale bar = 200µm). The boxed regions are at 400X magnification (scale bar = 50 µm). 46

Figure 3.3 (A) Fluorescent microscopy image of the ischemic femoral head stained with calcein captured at 20X magnification. The dashed white line indicates the subchondral region that was assessed for microcracks. (scale bar = 2 mm) (B) shows an image of an individual trabeculae captured at 200X magnification with a microcrack (indicated by an arrow). 47

Figure 3.4 Bar graphs showing (A) crack density and (B) crack surface density. These parameters were significantly greater in the ischemic subchondral region compared to the normal side. (*) $p < 0.01$, $n = 5$ per group 48

Figure 3.5 (A) Representative normal and (B) ischemic backscattered scanning electron microscopy images. The dashed line in both images separates the calcified cartilage region (CC) and the subchondral bone region (SB). The soft tissue and marrow space was removed by a common threshold and set to a gray level of zero (black). The brightness and contrast of both images were calibrated to show weight percent distribution of calcium. (C) Representative bone mineral density distributions of the calcified cartilage regions and (D) subchondral regions of both normal and ischemic bone. 50

Figure 3.6 (A) A graph showing representative load displacement curves of ischemic (double line) and the normal (single line) bone from the subchondral region. The load displacement curve for normal indentations typically show greater penetration depth compared to the ischemic indentation. (B) A representative scatter plot of the reduced moduli at different locations in both subchondral regions of normal (white diamond) and ischemic bone (black circle). A larger range of moduli is seen in the ischemic bone indentations compared to the normal bone indentations. (C) A graph showing the mean moduli \pm standard deviation of the normal and ischemic groups. The modulus was significantly increased in the ischemic subchondral region compared to the normal side. (*) $p < 0.05$, $n = 5$ per group (D) A graph showing the mean hardness \pm standard deviation of the normal and ischemic groups. The mean hardness was higher in the ischemic side but the difference was not statistically significant. 53

Figure 4.1 Scanning electron microscopy images of (a) normal and (b) necrotic trabecular bone at 2 weeks post-surgical induction of osteonecrosis. The arrows in the necrotic

region show discontinuous canaliculi. MicroCT of (c) normal and (d) necrotic femoral head following 8 weeks post ischemia induction. 66

Figure 4.2 Von Kossa and McNeal tetrachrome staining of normal and necrotic bone. (a) The normal coronal section of the femoral head captured at 5X magnification. (b) The necrotic femoral head captured at 5X magnification with resorbed (red arrows) and newly ossified regions (green arrow). Higher magnification of (c) normal trabecular bone with osteoblasts (blue arrows) lining the surface, (d) necrotic trabecular bone with osteoclastic pits (white asterisks), and (e) newly ossified bone with osteoblasts (blue arrows) lining the surface. All higher magnification images were captured at 600X 67

Figure 4.3 Backscattered electron images at 50X magnification of (a) normal femoral head, (b) necrotic portion of the femoral head, and (c) newly ossified regions of the experimental femoral head. Higher magnification images at 550X of (d) normal femoral head, (e) necrotic portion of the femoral head, and (f) newly ossified regions of the necrotic femoral head. The white arrows indicate location of the osteoid seam 68

Figure 4.4 (a) Phosphorous TEY L-edge XANES spectra of model compounds. (b) Phosphorous TEY L-edge XANES spectra of normal, necrotic and newly ossified regions of the femoral head. (c) Phosphorous TEY K-edge XANES spectra of model compounds. (d) Phosphorous TEY K-edge XANES spectra of normal, necrotic and newly ossified regions of the femoral head 71

Figure 4.5 (a) Oxygen K-edge TEY XANES spectra of model compounds. (b) Oxygen K-edge TEY XANES spectra of normal, necrotic and newly ossified regions of the femoral head. (c) Oxygen K-edge FY XANES spectra of model compounds. (d) Oxygen K-edge FY XANES spectra of normal, necrotic and newly ossified regions of the femoral head . 74

Figure 4.6 Representative Raman spectroscopy of normal, necrotic, and newly ossified bone. (b) Bar graphs of the carbonate (1070 cm^{-1}) to phosphate peaks u_1PO_4 (960 cm^{-1})

and (c) and u_2PO_4 (430 cm^{-1}) ratio pooled from 5 femoral pairs. The data is represented as mean \pm standard deviation. (* $p < 0.05$)..... 76

Figure 5.1(a) High magnification von Kossa and McNeal tetrachrome stained photomicrographs captured at 200X magnification of normal, no treatment (necrotic), bone morphogenetic protein-2 (BMP) treated, ibandronate (IB) treated, and BMP+IB treated trabecular bone. Osteoblasts (yellow arrow) line the surface of normal, BMP treated, and BMP+IB treated trabecular bone. Several osteoclasts (red arrow) line the surface of bone in the no treatment image. (b) High magnification hematoxylin and eosin stained photomicrographs captured at 200X of new bone formation surrounding necrotic bone (dotted line) in the BMP and BMP+IB treated trabecular bone. Diminished or absent lacunae staining was present in necrotic bone (white arrow). 89

Figure 5.2 Backscattered scanning electron images of normal, no treatment (necrotic), bone morphogenetic protein-2 (BMP) treated, ibandronate (IB) treated, and BMP+IB treated trabecular bone captured at 50X magnification. The BMP and BMP+IB treated trabecular bone appear thicker than the no treatment and IB treated bone. Scale bar = 1 cm..... 91

Figure 5.3(a) Carbonate to phosphate peak area ratio of normal trabecular bone was significantly lower than no treatment (necrotic) ($p = 0.001$)*, IB (ibandronate) treated ($p = 0.001$)*, and BMP+IB (bone morphogenetic protein + IB) treated bone ($p = 0.003$)**. (b) Carbonate to Amide I and (c) Mineral to Matrix peak area ratio of the normal group was significantly lower than no treatment ($p \leq 0.01$)*** and IB treated bone ($p \leq 0.004$)***. (n=5 per group) 93

Figure 5.4. Bar graphs of the (a) average reduced modulus and (b) hardness of the normal, no treatment (necrotic), bone morphogenetic protein-2 (BMP) treated, ibandronate (IB) treated, and BMP+IB treated trabecular bone. The reduced modulus of

the IB treated bone was significantly higher than normal healthy trabecular bone
(*p=0.024), and the IB treated group was significantly higher than the BMP and BMP+IB
treated groups (p≤0.02). (n=5 per group) 94

Figure 6.1 Overview of related material changes of necrotic bone with and without
treatment aided by BMP-2. 103

List of Tables

Table 2.1 Tissue Elastic Modulus of Trabecular Bone. Table Reproduced from [9].	13
Table 2.2 Immunolocalized noncollagenous proteins in adult human bone. Table modified from [10]. *Faint to strong immunostaining, —no immunostaining, BSP: bone sialoprotein, BMP-2: bone morphogenetic protein -2, TGF- β : transforming growth factor-1.	17
Table 2.3 Raman Spectroscopy band assignments for mineral and matrix components of bone. Table reproduced from [11].	34
Table 3.1 The weighted mean of the bone mineral density distribution (CaMean) and the weight percent value with the most frequency (CaPeak) from subchondral bone of each femoral head.	51
Table 3.2 The reduced modulus (E_r) from subchondral bone of each femoral head	54
Table 3.3 The hardness (H) from subchondral bone of each femoral head	55
Table 4.1 Experimental setup for spectral acquisition at respective beamlines.	64
Table 4.2 Carbonate to phosphate ratios of Total Electron Yield (TEY) and Fluorescent Yield (FY) Oxygen K edge XANES spectra from the Spherical Grating Monochromator Beamline	75
Table 5.1 The mean \pm standard deviation of weight percent calcium and nanomechanical properties of the treatment groups.	95

Chapter 1

Introduction

The skeletal system is a complex organization of bone and cartilage responsible for many roles to support the normal function in the body. This includes muscle attachment, hematopoiesis, mineral storage, structural support, and protection of vital organs. Bone, a component of the musculoskeletal system, is a heterogeneous and hierarchical composite structure composed of collagen and hydroxyapatite [12]. The material properties of bone, which include mechanical and compositional properties, are of particular focus in this report. More specifically, the bone within the hip is the focus to study the material properties following femoral head ischemia. Femoral head ischemia is a loss of blood flow to the femoral head which can lead to the cells within the bone tissue to die, also known as osteonecrosis (“bone death”).

Legg-Calvé-Perthes disease (LCPD) is a childhood hip disorder attributed to the loss of blood flow to the femoral head. If diagnosed when patients already have some deformity of the femoral head, patients can develop early osteoarthritis of the hip. Successful treatment is largely dependent on maintaining sphericity while the femoral head is revascularized with new blood supply and reossified with new bone. The study of this disease is limited due to few human pathological specimens; however, a piglet model of ischemic osteonecrosis of the femoral head was developed to study the pathology of the disease. The model demonstrates similarities between the pathology of LCPD diagnosed patients that develop a severe flattening deformity of the femoral head. The model also demonstrates that the femoral head goes through an initial avascular stage followed by a repair stage with new blood supply that brings an imbalance of bone formation and bone resorption. This report aims to determine the material changes of bone in the avascular and repair stages.

1.1 Specific aims of the dissertation

1.1.1 Rationale

Previous studies with necrotic bone show differences in the mechanical properties and structure compared to normal bone. In the piglet model of osteonecrosis, the repair process involves new blood supply and increased bone resorption by osteoclasts. The increased bone resorption leads to an overall net bone loss in the femoral head. Interestingly, before this process occurs, the macroscale mechanical properties from indentation and compression tests are significantly decreased even as the bone in the femoral head appears intact based on radiological findings [13,14]. Furthermore, a subchondral fracture can be later identified in the experimental model as the femoral progresses through its avascular stage [15]. The mechanism for subchondral fracture and decreased macroscale mechanical properties were undetermined and required a study that focused on the micro- and nano- material level properties of bone in the subchondral region during the avascular stage of ischemic osteonecrosis of the femoral head.

During the resorptive (i.e. repair) stage of the experimental model of femoral head osteonecrosis, the bone is hypermineralized [16]. In addition to bone resorption, at 8 weeks post ischemia the femoral head has been shown to initiate new bone formation in the periphery, but the newly ossified bone does not form in pace with the extensive resorption of the necrotic bone. Bisphosphonates are anti-resorptive agents that bind to the bone mineral (i.e. hydroxyapatite) in the bone tissue and inhibit bone resorption by osteoclasts. Targeted treatment of the necrotic bone with bisphosphonates has been shown to decrease osteoclast mediated resorption of necrotic bone compared to non-treated necrotic bone [17], but osteoclast number in the treated femoral head remains

significantly high compared to normal bone. Very little is known about the chemical changes to bone following ischemic osteonecrosis. Hydroxyapatite is a well-known mineral component to trabecular bone and it is known to be present in many forms due to ionic substitution. In fact, various ionic substitutions have been shown to influence osteoclast proliferation [18] and activity [19,20]. The hypermineralized state suggested chemical changes in necrotic bone that were undetermined and required a study to assess chemical changes that could have possible influence on excessive resorption of bone.

The repair process post ischemia is an imbalanced process that allows excessive bone resorption of bone and lacks sufficient bone formation. In the developing femoral head, the bone models and remodels over time though a complex process involving the optimal balance of bone formation and resorption. Treatment of ischemic bone aims to restore the balance by either decreasing bone resorption with anti-resorptive agents like bisphosphonates, increasing bone formation with anabolic agents like bone morphogenetic protein -2, or combining both agents to decrease resorption and increase bone formation. Therapies with bisphosphonates [17,21-23] and a combination of bisphosphonates and bone morphogenetic protein-2 [24,25] in experimental models of osteonecrosis were used to decrease excessive bone resorption, prevent femoral head collapse, and increase bone formation. In the experimental models, bisphosphonates preserves the femoral head structure by decreasing resorption by osteoclasts, and bone morphogenetic protein-2 promotes new bone formation. In osteoporotic patients, where net bone loss is also a problem, bisphosphonate treatment has been linked to decrease tissue heterogeneity, which is associated with increased brittleness and fracture risk [26-28]. The material properties of bone after treatment of femoral head ischemia was

undetermined, and required a study to investigate material changes during imbalanced remodeling.

Collectively, the research aims to determine material changes due to femoral head ischemia and provide a greater understanding of necrosis in the developing femoral head and the role of treatment on the material properties of bone. The dissertation focuses on three areas: 1) determining the nanomechanical and material changes of necrotic bone that precede trabecular fracture, 2) identifying the chemical changes in bone apatite composition during the repair stage, and 3) determining the effect of treatment with anti-resorptive and/or anabolic agents on the material properties of bone following femoral head ischemia. We hypothesized that femoral head ischemia alters trabecular bone composition and nanomechanical properties (e.g. mineral content, apatite chemistry, and modulus), and treatment of ischemic bone with anti-resorptive and osteogenic agents normalizes bone composition and nanomechanical properties with balanced bone formation and resorption. We identify unique microstructural damage and compositional variance in necrotic bone following ischemia that has been previously unavailable. In addition, we hope to provide valuable insight on the quality of bone after treatment, and potentially provide further evidence for the use of anabolic and anti-resorptive agents in young patients with femoral head ischemia. To test our hypothesis, the following aims were performed:

1.1.2 Aim 1

Determine the material changes that occur in necrotic bone that precede structural trabecular fracture [29]. This aim involved the study of avascular bone from an experimental model of femoral head osteonecrosis prior to any radiographic structural failure. In patients with Legg-Calvé-Perthes disease, a subchondral fracture is one of the

earliest radiographic signs identified [30]. We hypothesized ischemic osteonecrosis leads to early material and mechanical alterations in the bone of the subchondral region that predisposes it to fracture. The purpose of this aim was to assess the subchondral region for microcrack number, mineral content, and nanoindentation properties.

1.1.3 Aim 2

Identify the differences in the mineral apatite composition of necrotic bone during the repair stage versus areas of normal bone and newly formed bone [31]. This aim involved the study of revascularized bone from a piglet model of femoral head osteonecrosis after flattening deformity and increased resorption. In a piglet model of femoral head osteonecrosis, the bone at an 8 weeks post ischemia is hypermineralized [16]. Mineral composition has been previously shown to affect osteoclastic resorption. We hypothesized that the mineral apatite composition of bone is different in necrotic bone and possibly contribute to excessive resorption and structural collapse of the femoral head. This aim used X-ray absorbance near edge structure (XANES) and Raman spectroscopy to assess the microscopic and local phosphate composition of actively resorbed necrotic trabecular bone to isolate differences between areas of increased osteoclast resorption and normal bone formation.

1.1.4 Aim 3

Determine the effect of treatment with an anabolic agent, an anti-resorptive agent, and a combination of both anabolic and anti-resorptive agents on the materials properties of bone. After ischemia, the femoral head heals with an imbalance of bone formation and bone resorption (i.e. less bone formation and more bone resorption). BMP-2 is a well-known anabolic agent (stimulates the production of bone), and ibandronate is a well-

known bisphosphonate that acts as an anti-resorptive agent (decreases the amount of resorption by osteoclasts). Preclinical studies have shown an increase of bone formation and a decrease in bone resorption of the infarcted femoral head [24,25]. We hypothesized that treatment with bone morphogenic protein-2 and ibandronate post ischemia normalizes the material properties of the developing femoral head with balanced bone formation and resorption. The purpose of this aim was to determine compositional and nanomechanical properties of trabecular bone after treatment with BMP-2 and/or ibandronate. Raman spectroscopy, quantitative backscattered electron microscopy, and nanoindentation are used to evaluate the material properties.

1.2 Structure of the dissertation

The following chapter provides a contextual background to normal bone formation, disease due to an imbalance of bone formation and resorption, and various methods that can be applied to the study of disease. Each aim is addressed in its own respective chapter. Chapter 3 focuses on the avascular stage of the disease and determines the material changes in bone following osteonecrosis before and revascularization or repair occurs [29]. Chapter 4 focuses on the revascularized and repair stage of the disease where there is extensive repair by osteoclasts [31]. Chapter 5 focuses on anabolic and anti-resorptive treatments that aim to promote or inhibit remodeling and determines their effect on the material properties of bone. The final chapter summarizes and concludes the findings and discusses potential implications.

Chapter 2

2.1 Background

Bone is a highly vascularized tissue that models and remodels through skeletal maturity for structural support. When describing the material properties, the bone tissue is influenced by its composition. In fact, bone tissue is a composite material composed of many features that tightly regulate its process of modeling and remodeling. The purpose of this study is to measure the changes in the material properties of bone due to femoral head ischemia. To study the material changes, an immature piglet model of femoral head ischemia is used. The goal of this chapter is to provide a contextual background of normal bone formation and related material properties, to describe changes to bone with disease due to an imbalance of bone formation and bone resorption, and to discuss some of the methods that can be applied to study the material properties of bone to evaluate changes with disease.

2.2 Hip Anatomy and Complications during Development

The hip joint is a “ball and socket” joint composed of the proximal portion of the femoral head (“ball”) and the acetabulum (“socket”). The femoral head (Figure 2.1) is connected to the acetabulum by a ligament called the “ligamentum teres” and surrounded by a hip capsule, which is lined by the synovium. The articular cartilage is the portion of the femoral head that assists with smooth articulation of the surface of the femoral head to the acetabulum. The structural support provided by the hip joint allows people to engage in activities that require motion. For day to day activities (e.g. sitting, standing, walking and jogging), the hip can respond to loads around 2.4 to 5.5 times an individual's body weight [32,33]. Naturally, the femoral head needs to develop in a way that is able to respond to continuous loads to prevent dislocation or deformity. During early childhood

development, the hip joint allows for motion in many directions and can be impeded by complications associated with Legg-Calvé-Perthes disease [34]. Legg-Calvé-Perthes disease is associated with a loss of blood flow to the femoral head. Blood flow is of critical importance during the development of the femoral head for normal bone formation.

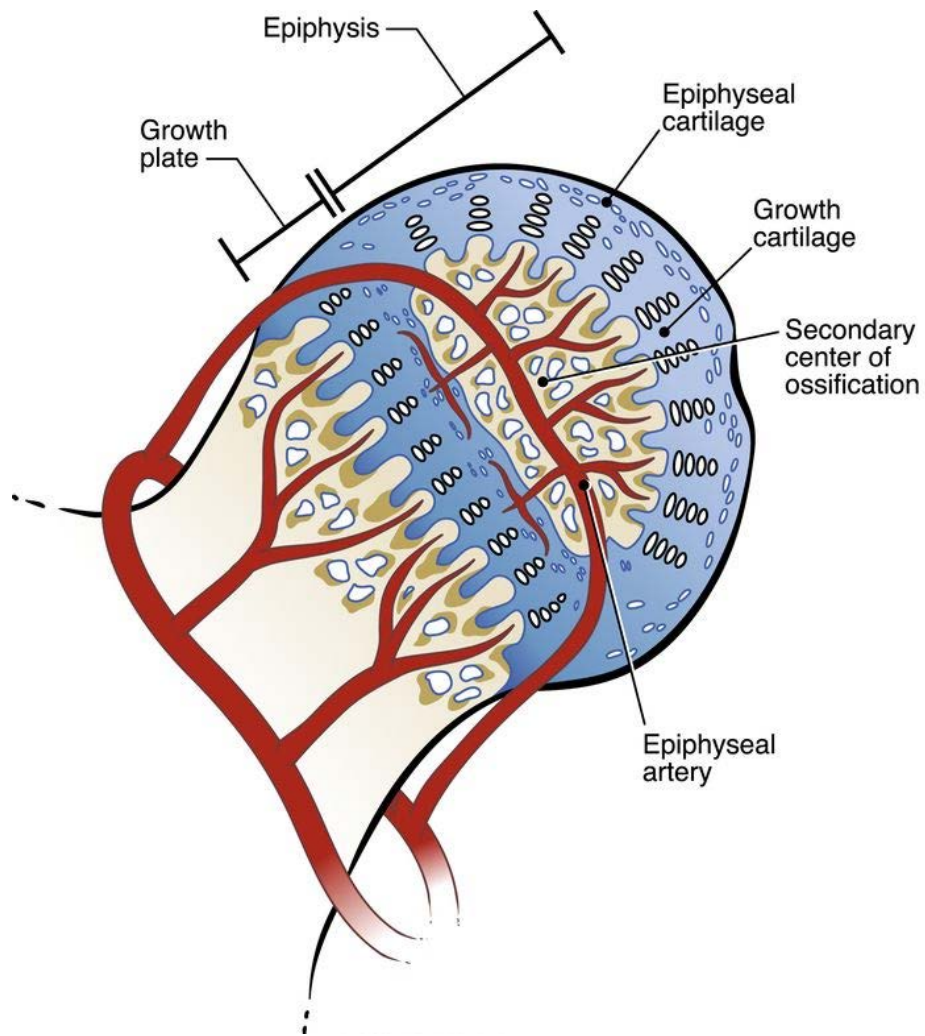


Figure 2.1 A schematic of a normal developing femoral head with related blood supply. Figure reproduced and modified from [1]

2.3 Bone vascularization

Bone is a highly vascularized organ with marrow responsible for producing blood cells during a process known as hematopoiesis, in addition to providing necessary precursors for bone remodeling. The blood supply to the developing femoral head is provided by two connected rings of arteries: an extracapsular and an intra-articular ring found near the cartilage neck junction [35,36], with additional blood supply coming from the artery of the ligamentum teres [37]. The blood supply from the arteries forms additional branches that are found within the cartilage and marrow of the developing femoral head. From fetal development to skeletal maturity (14 for girls, and 16 for boys), the marrow transitions, mostly in the appendicular skeleton, from red to yellow marrow, where the yellow marrow is influenced by the amount of fat cells and red marrow by the production and supply of red blood cells [38-40].

The blood supply within the femoral head assists with the modeling and remodeling of bone. During childhood development, there is an overall net gain in bone formation for overall growth and development called bone modeling, and over time the bone is also remodeled. Blood vessels that circulate within bone help support osteoprogenitors (which are necessary for bone formation) [41-43] and deliver osteoclast precursors (which are necessary for bone resorption) [44-46]. Contrary to mature adults, during development, bone and cartilage are both vascularized tissues. Cartilage canals have an important contribution to bone formation through a process called endochondral bone formation [47]. In developing femora of chicken, these canals penetrate and through the cartilage supplying stem cells for endochondral bone formation [48], and is proposed similarly in developing humans [49]. Endochondral bone formation uses the cartilaginous scaffold for bone formation by cells known as osteoblasts, which are to be later described.

2.4 Cortical and trabecular bone

The femur is composed of two types of bone: cortical and trabecular bone that contributes to the load and support within the hip (Figure 2.2). Both types of bone contain mineralized collagen (Figure 2.3), but can vary in mineral and organic matrix components, structure, and mechanical properties. Cortical bone has a dense compact structure that can be found along the diaphysis (i.e. shaft) of the femur, and trabecular bone has a porous structure that can be found in greater volume at the proximal and distal ends of the femur. The high porosity of trabecular bone contributes to its reduced mechanical strength when compared to cortical bone. Interestingly, when comparing the mechanical properties of individual trabeculae to similarly cut cortical bone, the trabeculae still has significantly less mechanical strength when compared to cortical bone [50]. Coincidentally, this may be due to the differences in mineral chemistry, since cortical bone has been previously measured to be more mineralized than trabecular bone [51,52]. In fact, increased mineralization has previously been linked to increased mechanical properties [53,54].

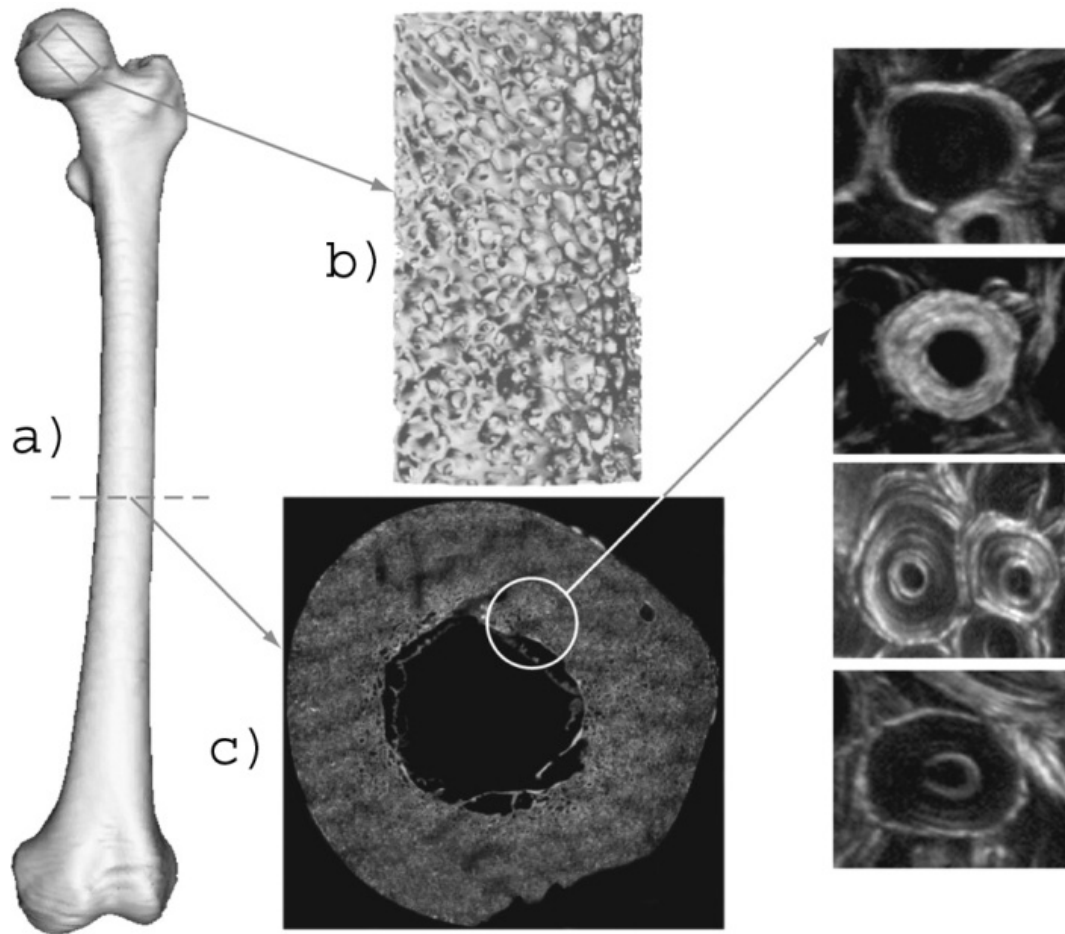


Figure 2.2 (a) A femur with a (b) micro-CT reconstruction of a cylindrical specimen of extracted trabecular bone from the femoral head together with a (c) histological image of a diaphyseal mid shaft section and a magnification of cortical osteonal structure. Figure reproduced and modified from [2]

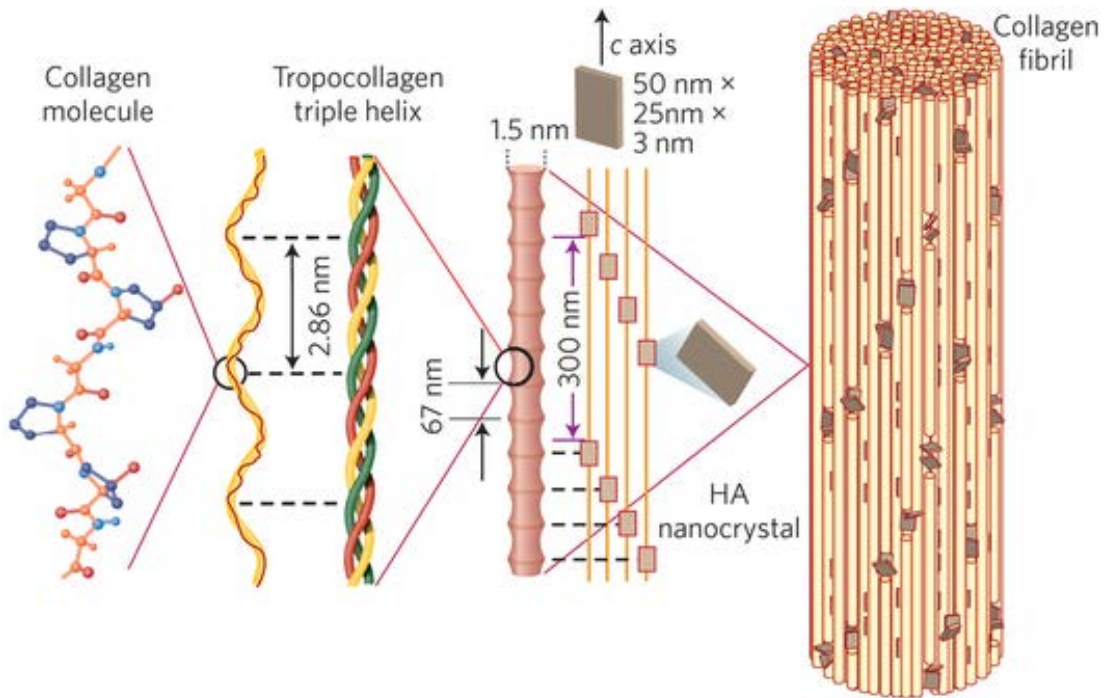


Figure 2.3 A collagen fibril found within bone which is composed of collagen protein molecules (tropocollagen) formed from three chains of amino acids and nanocrystals of hydroxyapatite (HA), and linked by an organic phase to form fibril arrays. Figure reproduced and modified from [3]

The trabecular bone is of particular focus due to its presence in the developing epiphysis of the femoral head. Trabecular bone, also known as cancellous or spongy bone, is composed of an amalgamation of thick and thin beams of bone that can have a plate or rod-like appearance. The space within the separation of the small beams of bone is accommodated by bone marrow. Structural parameters such as bone mass influence the mechanical properties of bone and measures of bone mineral density [55]; other morphometric parameters such as trabecular thickness, separation, and number are linked to mechanical properties of bone [56,57]. Additionally, the mechanical material properties can vary based on the anatomical location, wet vs. dry conditions, the type of mechanical test, and the species of animal tested (Table 1) [9]. It is at the material level

where local differences in composition and structure that can influence overall macroscale properties of bone. In addition to the mechanical properties of bone, much attention is placed on the composition of bone to describe bone quality.

Table 2.1 Tissue Elastic Modulus of Trabecular Bone. Table Reproduced from [9].

Testing technique	Bone type	Tissue modulus (GPa)
Buckling	Human proximal tibia	11.38 (wet), 14.13 (dry)
Experiment-FEA	Human proximal tibia	23.6 ± 3.34
	Human greater trochanter	24.4 ± 2.0
	Human femoral neck	21.4 ± 2.8
	Human femoral neck	18.0 ± 2.8
	Bovine proximal tibia	18.7 ± 3.4
	Human vertebra	6.6 ± 1.0
	Human vertebra	5.7 ± 1.6
	Human proximal femur	10 ± 2.2
	Bovine proximal tibia	6.54 ± 1.11
Ultrasonic technique	Human femur	13.0 ± 1.47
	Human femur	17.5 ± 1.12
	Bovine femur	10.9 ± 1.57
	Human tibia	14.8 ± 1.4
	Human vertebra	9.98 ± 1.31
Nanoindentation	Human femoral neck	11.4 ± 5.6
	Human distal femur	18.1 ± 1.7
	Human vertebra	13.4 ± 2.0

Table 2.1— *Continued*

	Human femural head	21.8 ± 2.9
	Human femur trochander	21.3 ± 2.1
	Human distal radius	13.75 ± 1.67
	Human vertebrae	8.02 ± 1.31
	Porcine femur	21.5 ± 2.1
	Human tibia/vertebrae	19.4 ± 2.3
	Sheep proximal femur	20.78 ± 2.4

2.5 Composition and mineralization of bone

Calcium phosphate, collagen, and non-collagenous proteins constitute the composition of the organic and inorganic components of bone which have been well reviewed [58]. The organic components of bone include type I collagen, proteoglycans, glycoproteins, and Gla-proteins. The inorganic component of bone is described as a calcium phosphate which is considered to be most analogous to hydroxyapatite ($\text{Ca}_{10}(\text{PO}_4)_6(\text{OH})_2$).

2.5.1 Collagen

Bone consists of highly organized collagen fibrils that are thought to act as a supportive matrix for mineral deposition and to help provide tensile strength. The organization of the fibrils are not well understood but are proposed to organize in a characteristic banding of 68-70 nm [59-61]. The organization of the fibrils are described to give rise to “dense zones”, where as many as 5 collagen molecules overlap, and “hole zones”, where only 4 molecules overlap. These “hole zones” are proposed nucleating centers for mineralization [62,63], where molecules are arranged to allow heterogeneous nucleation of crystalline structures. Indeed, attempts to show crystalline formation within

“hole zones” have proven successful in *in vitro* studies using a collagenous tendon [64], and in cases aided by non-collagenous proteins [65,66].

2.5.2 Non-collagenous proteins and growth factors

Non-collagenous proteins (NCPs) play an important role in the induction and regulation in the bone mineralization process. Many NCPs within the bone matrix have been previously summarized [58]. Bone sialoprotein, osteopontin, and osteonectin are glycoproteins that are commonly described. Osteopontin influences calcium phosphate by inhibiting growth and crystal formation [67-69]. Osteonectin inhibits crystal growth *in vitro* [70,71], and bone sialoprotein binds to calcium phosphate and cell surface integrins for nucleation during early mineralization [72-75]. Osteocalcin is a bone Gla-protein mostly found in mineralized bone matrix and has been linked to increased bone formation in osteocalcin deficient mice [76-78].

Proteoglycans include an array of various NCPs such as decorin and biglycan that are found within the matrix of mineralized tissue and can be commonly identified by their proteic core where glycosaminoglycans are covalently linked [58]. Decorin influences the assembly of collagen fibrils as high and low levels affect the thickness of fibrils, indirectly affecting mineralization [79,80]. Alterations in collagen formation are linked to a biglycan deficiency [81]. Collectively, proteoglycans, glycoproteins, and Gla-proteins coordinate with one another to modulate the mineralization by affecting crystal growth and formation within the collagen matrix.

Various non-collagenous proteins have been identified through immunolocalization and are detailed in the following table (Table 2) [10]. Among the proteins, are well known growth factors such as bone morphogenetic protein-2 (BMP-2) and transforming growth factor beta (TGF- β). BMPs are multifunctional growth factors that belong to the TGF- β superfamily and have been extensively studied since they were

identified approximately 50 years ago by Marshall Urist [82]. Protein extracts from bone that include BMP are described to stimulate bone formation through endochondral ossification [83]. Thus, BMP is extensively used in many biomaterial applications to induce bone formation [84-87]. BMP's role helps stimulate development of new blood vessels and bone cell differentiation, resulting in the formation of bone tissue [88].

Table 2.2 Immunolocalized noncollagenous proteins in adult human bone. Table modified from [10]. *Faint to strong immunostaining, —no immunostaining, BSP: bone sialoprotein, BMP-2: bone morphogenetic protein -2, TGF- β : transforming growth factor-1.

	Osteopontin	Osteocalcin	Osteonectin	BSP	Biglycan	Decorin	BMP-2	TGF- β	TGF- β 3	IGF-I
Osteoid	*	*	—	*	*	*	*	—	*	—
Osteoclasts	*	*	*	—	—	—	*	*	*	—
Osteoblasts	*	*	*	*	—	*	*	*	*	—
Osteocytes	*	*	—	—	—	—	—	—	—	—
Osteocyte lacunae	*	*	*	*	*	*	*	*	—	—
Canaliculi	*	—	*	—	—	*	*	*	*	*
Mineralized bone	*	*	*	*	*	*	*	*	*	*
Mineralization front	*	*	*	*	*	*	*	—	*	*
Calcified cartilage	—	*	*	*	*	*	*	—	—	—
Noncalcified cartilage	—	—	*	—	*	—	*	—	*	*

2.5.3 Osteoblasts, osteoclasts, and osteocytes

The bone tissue consists of three important cell types for formation and maintenance of bone: osteoblasts, osteoclasts, and osteocytes. Osteoblasts are known as bone forming cells that secrete collagen and mineral, the collagenous matrix that is secreted initially forms the osteoid. The osteoid also contains many non-collagenous proteins that help to modulate the mineralization by controlling collagen formation and affecting crystal growth. Osteoblasts line the surface of the bone and osteoid to create a mineralizing front. The exact mechanism for mineral formation remains unknown; however, mineral crystals are generally understood to originate from osteoblasts during normal bone formation. Recent studies with osteoblasts show intracellular formation of amorphous calcium phosphate and ionic calcium stored in mitochondrial granules and vesicles that are transported to the collagenous matrix before forming a more crystalline apatite [89].

Some osteoblasts, by an unknown mechanism, begin to embed within the osteoid and mineral matrix and become osteocytes [90]. The cells over time form canaliculi that channel dendritic projections that connect to cells that line the surface of bone in conjunction with other osteocytes within the bone matrix. Osteocytes are thought to play a role as mechanosensors that can respond to mechanical loading sensed by interstitial fluid flow within the bone matrix [91-93]. In addition, osteocytes are also sensitive to microdamage in bone and apoptosis (“programmed cell death”) of other osteocytes [94]. In fact, the osteocytes are shown to regulate the process in which bone is repaired and remodeled by osteoblasts and osteoclasts [95,96].

Osteoclasts are large multinucleated bone resorbing cells. They are able to form a seal around bone tissue, secrete acid, and secrete proteases such as cathepsin K, to dissolve mineral and degrade the collagenous matrix [97]. During normal bone

remodeling, osteoblasts, osteoclasts, and osteocytes work together to remodel or replace bone tissue that may be damaged or to remove bone tissue that is used less due to diminished mechanical loading. Bone remodeling is a balanced process that occurs throughout life. Specifically, older mineralized bone is resorbed by osteoclasts and is followed by osteoblasts for bone formation until the older bone is replaced [98]. Imbalance of the remodeling process can affect the rate at which older bone is replaced and new bone is formed. This is evident in bone disorders such as osteoporosis and juvenile osteonecrosis (bone death) of the femoral head, where net bone loss contributes problems like fracture in patients with osteoporosis or deformity in patients with osteonecrosis.

2.6 Microdamage and fracture in bone

Bone continually undergoes cyclical loading during day to day activities from walking and/or running. Microdamage is thought to develop from normal wear and tear and is repaired with bone remodeling. Osteocytes are sensitive to microdamage in bone have been recently shown to stimulate osteoclast response for resorption of damaged tissue. The exact mechanism of detection is unknown, but it has been linked to apoptotic osteocytes and nearby osteocytes that upregulate signals for osteoclastogenesis and eventual bone resorption [99,100]. Unfortunately, this has only been assessed in adult cortical bone. The process for detection of microdamage in the trabecular bone of the developing femoral head is unknown. However, the point of failure or damage in both cortical and trabecular bone is presumed to initiate at collagen fibrils, where there is collagen fiber-matrix debonding, disruption of the mineral collagen aggregate, and ultimate failure of the collagen fibril [101].

Microdamage in trabecular bone increases with age and disease. The macroscale mechanical properties in bone with microdamage are decreased compared to normal and younger bone with little to no microdamage [102,103]. Microdamage can be identified through a bulk staining technique where a dye can fill in various types of microdamage (Figure 2.4) [104]. Four types of microdamage are routinely described in literature: microcracks, diffuse damage, cross-hatching, and microfractures [105]. Briefly, microcracks are defects in bone with sharp borders. Diffuse damage is identified by patches of stained mineralized matrix disrupted by local deformation. Cross hatching are a web of small microcracks, and microfractures are fractured trabecular struts. All forms of damage can be present in trabecular bone, and an accumulation of microdamage *in vivo* makes bone more susceptible to further damage [106], which may be rationally presumed to lead to fractures in diseases like osteoporosis or osteonecrosis of the femoral head.



Figure 2.4 Three types of microdamage indicated by arrows. Left to right is microcrack damage, cross-hatching damage, and diffuse damage. Image reproduced from [4]

2.7 Juvenile osteonecrosis of the femoral head

Legg-Calvé-Perthes disease (LCPD) is a juvenile hip disorder attributed to the loss of blood flow to the bony epiphysis which causes osteonecrosis of the femoral head. The disease was first discovered approximately 100 years ago by three medical doctors, Legg, Calvé, and Perthes [107-109]. The disease affects 1 in 740 boys and 1 in 3500 girls between the ages of 2 to 14 [110]. The development of a permanent femoral head deformity is a common complication of LCPD, with 50% of patients having hip pain during early adulthood and developing disabling osteoarthritis before age 60 due to the femoral head deformity [111,112]. During healing, the bony epiphysis undergoes extensive remodeling and repair. Extensive resorption of necrotic bone is proposed to lead to

collapse of the femoral head; therefore, balanced bone formation is expected to help maintain shape of the femoral head during the healing process.

2.7.1 Treatment of Legg-Calvé-Perthes Disease

Current treatment options of juvenile femoral head osteonecrosis include surgical and non-surgical approaches with the goal of maintaining femoral head sphericity during revascularization. Typically this occurs by repositioning the femoral head epiphysis to prevent loading and deformation on the healing femoral head [113]. Surgical options include various types of osteotomies, where bone is cut, repositioned, and fixed with surgical hardware to prevent continued loading on the healing epiphysis. Non-surgical options include abduction-casting that also helps prevent continued loading.

Unfortunately, current strategies to treat the disease have led to a modest success rate of 40-70% [1]. But still unknown are the limiting factors that prevent successful healing and bone repair.

In patients, magnetic resonance imaging (MRI) and x-ray radiography are currently used to evaluate bone repair and shape by visualizing the amount of revascularization and re-ossification. Since the femoral head shape and congruency are considered to be important determinants to prevent degenerative arthritis of the hip and since the femoral head shape is determined by the amount of resorption of bone and the bone's ability to withstand load bearing [1,113], it is therefore important that any new ossification within the previously infarcted femoral head can withstand deformation and damage. Unfortunately, the material properties of bone in treated patients are lacking. However, experimental models of the pathological repair process after femoral head ischemia have been evaluated.

Recent therapies with bisphosphonates [17,21-23] and a combination of bisphosphonates and bone morphogenetic protein-2 [24,25] in experimental models of

osteonecrosis were used to decrease excessive bone resorption and prevent femoral head collapse. In the experimental models, bisphosphonates preserves the femoral head structure by decreasing resorption by osteoclasts, and bone morphogenetic protein-2 promotes new bone formation. Techniques in local and systemic delivery of the biological agents have been assessed. Systemic treatment with of bisphosphonates has previously been shown not to initially penetrate necrotic bone due lack of blood supply [21], while local treatment in the infarcted femoral head is retained [23]. While treatments with bisphosphonates and bone morphogenetic protein-2 aims to restore the imbalance of excessive bone resorption in the experimental model of osteonecrosis, the material properties of preserved necrotic bone within the femoral head structure by bisphosphonates versus new bone stimulated by bone morphogenetic proteins is undetermined and is of focus in chapter 5.

2.7.2 Pathology of Legg-Calvé-Perthes Disease and Experimental Animal Model

The pathology of LCPD goes through four stages: avascular, resorptive, re-ossification and residual (healed) (Figure 2.5) [114-116]. Briefly, the initial stage is the avascular stage where there is no blood flow to the femoral head. During this stage, the radiography of the infarcted femoral head can show a fracture in the region below the cartilage known as subchondral bone (not shown in the figure). Upon the return of blood flow, the resorptive phase involves a breakdown and fragmentation of the necrotic bone within the femoral head. The femoral head is continually loaded during this resorptive stage contributing to the breakdown and fragmentation of necrotic bone leading to a flattening deformity of the femoral head. The third stage is the re-ossification stage where new bone forms in the femoral head along the periphery near cartilaginous regions. The final stage is the healed stage where the bone within the femoral head is normal, and the head keeps its final shape.

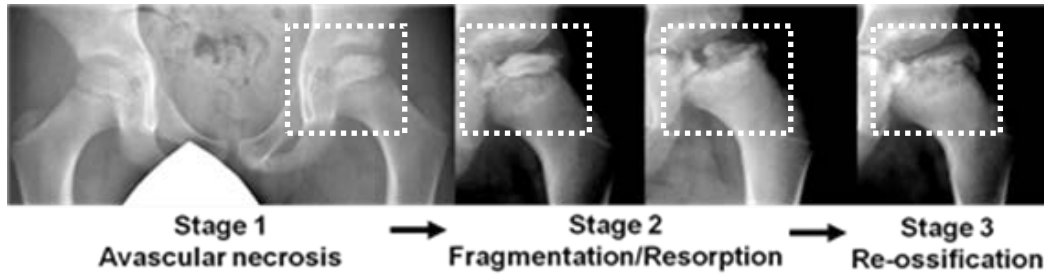


Figure 2.5 The various radiographic stages of the disease with an increasing flattening deformity and resorption/fragmentation over a one to two year period with eventual re-ossification and healing. The boxed regions indicate the affected femoral head. Image reproduced from Texas Scottish Rite Hospital.

Due to the lack of pathological specimens from children, an experimental model of the disease has been used to study the pathology. The experimental model uses a piglet between 4-6 weeks in age with femoral heads in comparable size to a 4-6 year-old child. Figure 2.6 shows the radiographic stages of the disease in the experimental model [5].

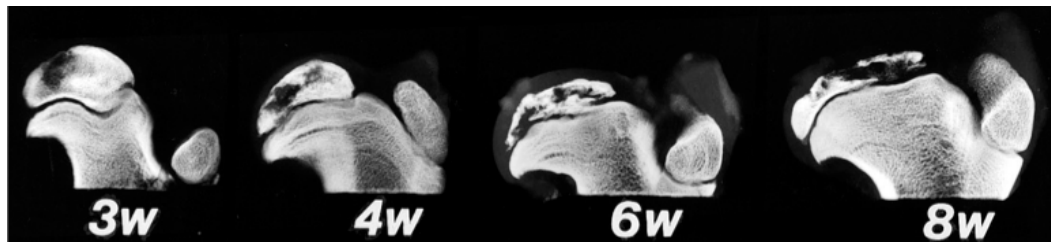


Figure 2.6 The various radiographic stages of increasing flattening deformity and increasing areas of resorption/fragmentation at 3, 4, 6, and 8 weeks post ischemia induction of the femoral head in the experimental model with piglets. The figure was reproduced from [5].

In orthopedics, radiography is commonly used to verify structural abnormalities like fracture or dislocation. While a loss of blood flow is proposed to be the initiating event in LCPD, one of the earliest radiological indicators is increased radiodensity in the affected femoral head [114] and in some cases subchondral fracture [30]. Increased

radiodensity suggests that the X-ray's ability to pass through bone is hindered, and fracture suggests mechanical insufficiency or failure of bone. Taken together, the early radiological findings suggest mechanical and/or compositional changes can occur within the necrotic femoral head.

Previous studies comparing normal versus necrotic bone show differences in the mechanical and compositional properties of normal versus necrotic bone. In the experimental animal model of osteonecrosis, there are decreased macroscale mechanical properties of the infarcted femoral head before any repair from bone resorption [13,14]. Other mechanical studies of necrotic bone from adult patients measured by compressive tests show decreased yield strength and modulus [117], which help substantiate finite element models for prediction of fracture and collapse in the adult femoral head [118,119]. Bone mineral density distributions measuring weight percent of calcium was increased in the necrotic bone at time points of 4 and 8 weeks post ischemia induction in the experimental model with piglets [16]. Increased mineral content is a distinct change in composition that can be further elucidated by recent efforts of material characterizations of bone that involve X-rays, vibrational spectroscopy, and nanomechanical testing.

2.8 Material Characterization Techniques

Bone is a heterogeneous and hierarchal composite structure composed of collagen and calcium phosphate. The material properties of bone are mainly influenced by the composition. Various techniques have been used to assess the composition and mechanical properties of bone that include quantitative backscattered electron microscopy, spectroscopy, and nanoindentation.

2.8.1 Nanomechanical Testing

Nanoindentation is a technique used to assess the mechanical properties of objects at nano- and micro-level scales [6]. The technique has been used on thin film metals [120-123], polymers [124,125], and biological tissues [126-129]. Numerous studies to date have applied nanoindentation to study the mechanical material properties of bone [130-137]. As detailed in Table 1, the nanoindentation technique has been applied to measure the mechanical properties of trabecular bone from varying locations. Due to the heterogeneous and anisotropic nature of bone, the modulus measured by nanoindentation can vary based on location [9]. Other influences on nanoindentation properties include pathological diseases such as osteoporosis where decreased mineral to matrix ratio was coincident with decreased nanoindentation modulus [138]. For osteonecrosis of the femoral head, only one other study has investigated the nanoindentation properties necrotic bone where increased modulus was not found in necrotic bone but in sclerotic regions [139]. However, the study investigated the femoral heads from adult patients with unexplained etiology, and since osteonecrosis in adult patients can be initiated by a variety of risk factors associated with steroid use, sickle cell anemia, and alcoholism, extrapolating results to an immature piglet model of osteonecrosis may be confounding.

The nanoindentation system consists of three key components for load and depth sensing measurements: a tip with a specified geometry, transducer, and controller. The most common tip geometry used for bone is a diamond, the three-sided pyramidal tip, also known as the Berkovich tip. Compared to sharper cubed-corner tips, the Berkovich tip produces more elastic plastic deformation than crack growth/fracture [140]. The controller operates the transducer for accurate force and displacement measurements at the tip, and the volume of material involved in the mechanical response

is based on the depth of the tip indentation [133,141]. An indentation procedure typically consists of three segments forming a trapezoidal function where there is a loading, holding, and unloading segment. Incremental loading segments are used to capture information at increasing depths, where the unloading segment is used to calculate modulus and hardness at corresponding depths.

The hardness and modulus are calculated from force and the displacement unloading curve (Figure 2.7), and the known mechanical properties and geometry of the diamond tip. The unloading portion of the curve provides four measurable parameters unique to the elastic deformation of the material being tested: the initial unloading stiffness, the peak indentation load, and indentation depth. The reduced modulus (1), E_r , is calculated from the initial unloading stiffness, S , and the projected area of the elastic contact of the tip, A . The projected contact area of the Berkovich tip is determined by calibrating the tip at various indentation depths with fused quartz. The reduce modulus is calculated in the following equation where

$$E_r = \frac{\sqrt{\pi}}{2} \frac{S}{\sqrt{A}} \cdot (1)$$

The hardness (2), H , is calculated from the P_{max} , the peak indentation load, and projected area of elastic contact shown in the following equation where,

$$H = \frac{P_{max}}{A} \cdot (2)$$

The reduced modulus and the elastic modulus of the material being tested are related by the following equation,

$$\frac{1}{E_r} = \frac{(1-\nu^2)}{E} + \frac{(1-\nu_i^2)}{E_i},$$

where E is the elastic modulus of the material, ν is the Poisson's ratio of the material, and E_i and ν_i are the elastic modulus and Poisson's ratio of the indentation tip.

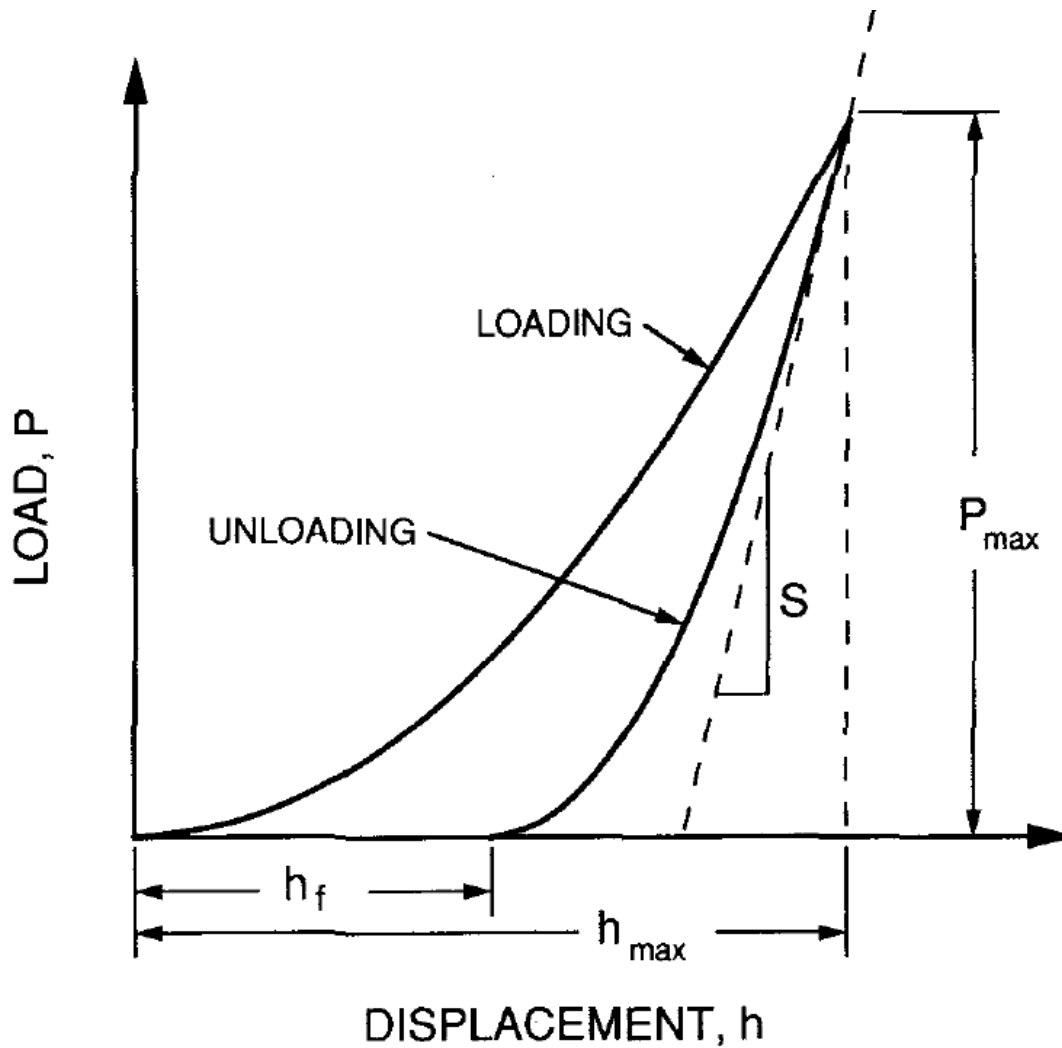


Figure 2.7 The load displacement data from an indentation experiment. The measure parameters shown are P_{max} , the peak indentation load, S , the initial unloading stiffness, h_{max} , the indenter displacement at peak load, and, h_f , the final depth of the contact impression. Reproduced from [6].

2.8.2 Quantitative backscattered electron imaging

Quantitative backscattered electron imaging (qBEI) is a technique that requires the use of a scanning electron microscope with a backscattered electron detector. The technique was validated on the mineralized bone tissue to measure bone mineral density distributions [7]. Prior to this study, qBEI was previously used in the same immature piglet

model of osteonecrosis described in this study, where increased mineral content was measured in necrotic bone at 4 and 8 weeks post ischemia induction [16]. Briefly, the matrix mineral density was determined in multiple regions of the femoral head including the calcified cartilage, the subchondral bone, and the mid epiphyseal region. At eight weeks, all regions showed a significant change in the bone mineral density distribution. This section describes the technique and some of the principles.

Backscattered electrons are produced from elastic scattering from an incident electron beam, and are used for compositional images [142]. Compositional images with backscattered electrons arise from samples with varying chemical composition, more specifically; backscattered electrons are better detected with increasing atomic numbers of the specimen atoms. Images produced by the scanning electron microscope are on a gray scale; less backscattered electrons detected appear darker, and more backscattered electrons appear lighter. In the case of mineralized tissue, hydroxyapatite ($\text{Ca}_{10}(\text{PO}_4)_6(\text{OH})_2$) is a naturally formed apatite that is a common analog to the calcium phosphate found in bone and teeth, where varying amounts of calcium would affect the average atomic number, and thusly the gray level imaged by the scanning electron microscope. In fact, Roscheger et al. calibrated a constant backscattered electron signal with carbon and aluminum standards to maintain a constant brightness and contrast setting to obtain images for the quantification of the weight percent calcium concentration of bone (Figure 2.8).

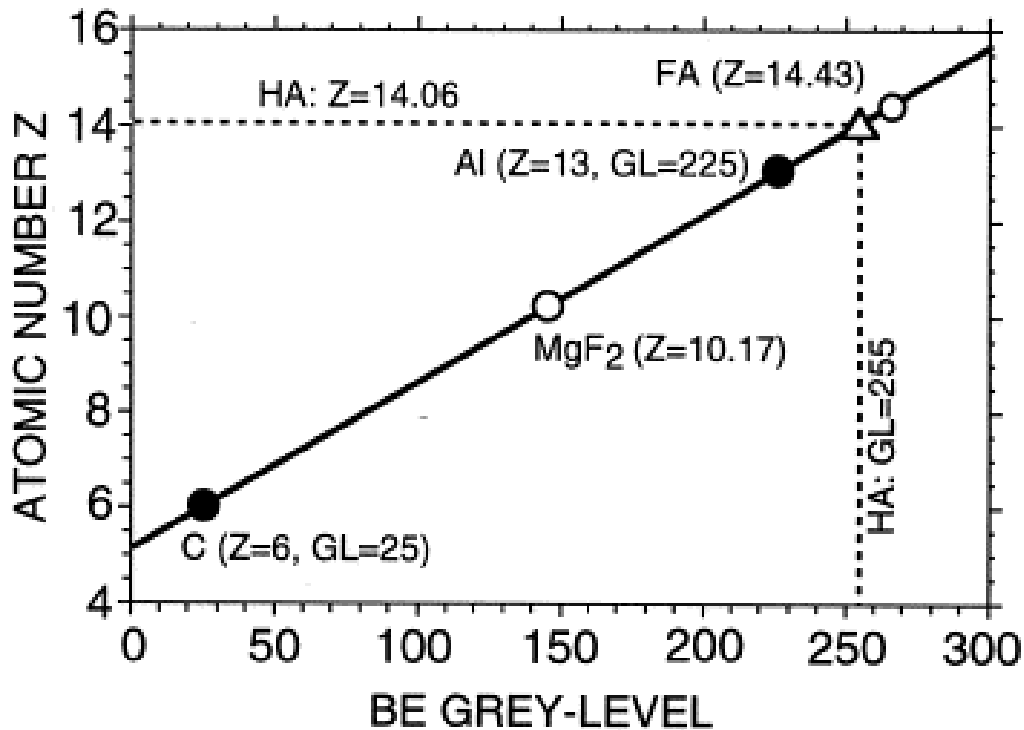


Figure 2.8 The calibration line based on standards of carbon (C) and aluminum (Al). Measured grey levels (GL) were verified with calculated a mean atomic number (Z) for magnesium fluoride (MgF₂), and fluorapatite (FA). Hydroxyapatite = HA, BE=Backscattered Electron. Reproduced from [7].

The weight percent of calcium in pure hydroxyapatite is 39.86%. Roschger et al. used hydroxyapatite as a bone analog for mineralized tissue with the highest weight percent of calcium and the osteoid, which has very low mineral content as 0 wt% of calcium. With correlated standards in carbon, aluminum, and hydroxyapatite at set grey levels, the grey level scale was converted to wt% calcium. The qBEI technique assumes hydroxyapatite to be the best analog to the part of the bone matrix with the highest weight percent calcium; however, mineralized bone was described previously as carbonated apatite due to substitutions within the crystalline structure [143,144]. Detecting these

changes in ionic substitutions can be performed by spectroscopy techniques that can measure molecular bonding and elemental coordination.

2.8.3 Spectroscopy

The mineral composition of bone can also be analyzed by various spectroscopy techniques including Raman and X-ray absorbance near edge structure (XANES) spectroscopy. Prior to this study, the mineral composition of the osteonecrotic trabecular bone in immature piglets measured by Raman and XANES spectroscopy was unknown. Raman spectroscopy is a form of vibrational spectroscopy that uses an incident light source from a laser and measures the change in the wavelength (also known as the Raman shift) due to inelastic scattering [142]. Inelastic scattering occurs when the scattered light from the incident light source has a different frequency. The change in the wavelength detected by Raman spectroscopy is unique to the chemical bonds present in a tested sample. XANES uses an incident X-ray source from synchrotron radiation, which can be used to describe the chemical structures of compounds and the chemistry of an element by providing information on valence, oxidation state, and coordination chemistry. The X-ray source is highly tunable to excite core shell electrons at specific energies that have unique to binding energies in different elements [145]. Both techniques have been applied to assess the mineral composition of bone where Raman spectroscopy can provide information on molecular bonding [146-148], and XANES elemental coordination [149-151].

2.8.3.1 XANES

XANES is sensitive to the chemistry of the absorbing atom, where information about the local geometry, oxidation, and atomic position can be extracted from multiple parts of a XANES spectrum. As described by Bare, the XANES spectrum is composed of a pre-edge, edge, and XANES region (Figure 2.9) [8]. The pre-edge provides information

on local geometry and is dependent on the oxidation state and bonding characteristics. The edge region, also dependent on the oxidation state, can be shifted to higher energies with an increase in the oxidation state. Finally, the XANES region provides information on interatomic distances and bond angles of the absorbing atom.

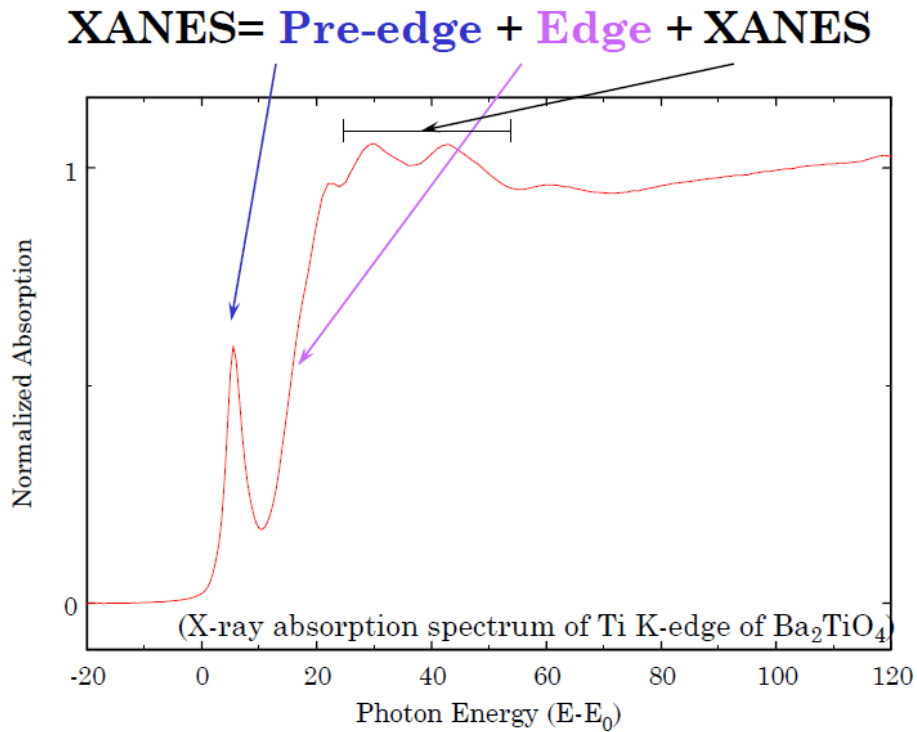


Figure 2.9 An X-ray absorbance near edge structure (XANES) spectrum of Ti K-edge of Ba₂TiO₄ with the pre-edge, edge, and XANES regions identified. Image reproduced from [8].

With the use of a synchrotron facility, where light is produced by electromagnets to accelerate electrons near the speed of light, multiple energy ranges for different elements can be studied. The binding energies for core electrons are unique for different elements and can be detected in the XANES spectrum [145,152]. Specifically, an incident

X-ray with sufficient energy can excite a core electron beyond its energy state leaving the atom “excited” with an empty electronic level. To relax the atom to a ground state, a higher level core electron moves to the empty electronic level and emits fluorescent and Auger electrons that can be detected for total electron yield and fluorescence yield. Therefore, understanding the spectral features of a XANES spectrum would consequently allow compounds with an unknown elemental coordination to be studied by probing specific binding energies to excite core electrons.

To detect shift and peak positions due to incorporation of various elements, model compounds are used often to determine how elements are present within molecular structure. For example, zinc that has been doped in hydroxyapatite can be assessed for its coordination environment by comparing XANES spectra with zinc containing model compounds [153]. Hydroxyapatite and amorphous carbonated calcium phosphate have been used as model compounds to assess the presence of calcium in the surface apatite formation of kidney stone biopsies [154]. Recently, phosphates of bone from various species were compared to hydroxyapatite and beta tri-calcium phosphate [155]. While, model compounds in XANES analysis are useful for chemical fingerprinting of the mineralized component of biological apatite, other techniques have been useful to assess both mineral and matrix components of bone.

2.8.3.2 Raman

Raman spectroscopy is a non-destructive technique that uses a laser to measure the mineral and matrix components of bone simultaneously. The matrix components of a Raman spectrum of bone include all of the collagenous and organic constituents, while the mineral components of a Raman spectrum of bone include measures of carbonate and phosphate. A detailed table by Mandair and Morris shown below describes peaks and bands that can be assessed within the bone matrix [11]. These peaks and bands

can be used to measure the mineral and matrix composition. Measurements include carbonate to phosphate ratios and mineral to matrix ratios. Carbonate-to-phosphate ratios provide information on the amount of the carbonate substitution within the crystal structure of bone, while mineral to matrix ratios provides information on the mineral content.

Table 2.3 Raman Spectroscopy band assignments for mineral and matrix components of bone. Table reproduced from [11].

Raman shift, cm^{-1}	Assignment	Comments
430	$\nu_2\text{PO}_4^{3-}$	Strong band
450	$\nu_2\text{PO}_4^{3-}$	Shoulder on 430 cm^{-1} band
584–590	$\nu_4\text{PO}_4^{3-}$	Multiple partially resolved components
609	$\nu_4\text{PO}_4^{3-}$	Shoulder on 590 cm^{-1} band
668	$\nu(\text{C-S})$	Cysteine
756	$\nu_4\text{CO}_3^{2-}$	B-type carbonate, very weak
853	$\nu(\text{C-C})$	Collagen proline, may include $\delta(\text{C-C-H})$ contribution from tyrosine
872	$\nu(\text{C-C})$	Mostly collagen hydroxyproline
920	$\nu(\text{C-C})$	Shoulder, mostly collagen proline
937	$\nu(\text{C-C})$	Proline and protein backbone
955	$\nu_1\text{PO}_4^{3-}$	Transient bone mineral (P-O) phase, usually seen in immature bone.

Table 2.3—Continued

957	$\nu_1\text{PO}_4^{3-}$	Bone mineral containing extensive HPO_4^{2-} , usually immature
959–962	$\nu_1\text{PO}_4^{3-}$	Bone mineral, mature
1003	$\nu(\text{C}-\text{C})$	Phenylalanine
1035	$\nu_3\text{PO}_4^{3-}$	Overlaps with proline $\nu(\text{C}-\text{C})$ component
1048	$\nu_3\text{PO}_4^{3-}$	
1060	Proteoglycan	Overlaps with lipids, collagen and components of $\nu_3\text{PO}_4^{3-}$
1070	$\nu_1\text{CO}_3^{2-}$	Overlaps with component of $\nu_3\text{PO}_4^{3-}$
1076	$\nu_3\text{PO}_4^{3-}$	Overlaps with component of $\nu_1\text{CO}_3^{2-}$
1176	$\nu(\text{C}-\text{O}-\text{C})$	Tyrosine, phenylalanine
1204	$\omega(\text{CH}_2)$	Tyrosine, hydroxyproline
1242	Amide III	Protein β -sheet and random coils
1272	Amide III	Protein α -helix
1293–1305	$\delta(=\text{CH})$	Lipid band, sometimes seen in fresh untreated bone
1340	Amide III	Protein α -helix, sometimes called CH_2CH_2 wag
1365	Pentosidine	Overlap with lipid 1369, cm^{-1} band
1375	Proteoglycan	Representative of glycosaminoglycans
1446	$\delta(\text{CH}_2)$	Protein CH_2 deformation

Table 2.3—Continued

1585	$\nu(\text{C}-\text{C}-\text{H})$	Weak band, aromatic ring
1609	$\delta(\text{C}=\text{C})$	Phenylalanine, tyrosine
1640	$\nu(\text{C}=\text{C})$	Shoulder to 1660, cm^{-1} band
1660	Amide I	Strongest amide I $\nu(\text{C}=\text{O})$ component, polarization sensitive
1690	Amide I	Shoulder, prominent with immature cross-links The band also relates to β -sheet or disordered secondary structure

Raman, XANES, qBEI, and nanoindentation are useful techniques for assessment of the compositional and mechanical properties of bone. All of which have been previously used to study normal and pathological bone samples to describe bone that has been found to be more brittle [156], hypermineralized [157], or distorted in its crystalline structure[158,159]. Compositional and mechanical measurements of necrotic trabecular bone of a developing femoral head have been limited to macroscale mechanical [13,14] and qBEI assessments [16]. Additional studies in this report detail multiple techniques that are combined, to provide comprehensive information on the pathology of bone material properties following ischemic osteonecrosis of the femoral head, where there is an imbalance in the amount of bone formation and resorption and on the influence of treatment to that aims to restore the balance.

Chapter 3

Microcrack Density and Nanomechanical Properties in the Subchondral Region of the Immature Piglet Femoral Head following Ischemic Osteonecrosis

3.1 Abstract

Development of a subchondral fracture is one of the earliest signs of structural failure of the immature femoral head following ischemic osteonecrosis and this eventually leads to a flattening deformity of the femoral head. The mechanical and mineralization changes in the femoral head preceding possible subchondral fracture have not been elucidated. We hypothesized that ischemic osteonecrosis leads to early material and mechanical alterations in the bone of the subchondral region. The purpose of this investigation was to assess the bone of the subchondral region for changes in the histology of bone cells, microcrack density, mineral content, and nanoindentation properties at an early stage of ischemic osteonecrosis. This piglet model has been shown to develop a subchondral fracture and femoral head deformity resembling juvenile femoral head osteonecrosis. The unoperated, left femoral head of each piglet (n=8) was used as a normal control, while the right side had a surgical ischemia induced by disrupting the femoral neck vessels with a ligature. Hematoxylin and eosin (H&E) staining and TUNEL assay were performed on femoral heads from 3 piglets. Quantitative backscattered electron imaging, nanoindentation, and microcrack assessments were performed on the subchondral region of both control and ischemic femoral heads from 5 piglets. H&E staining and TUNEL assay showed extensive cell death and an absence of osteoblasts in the ischemic side compared to the normal control. Microcrack density in the ischemic side (3.2 ± 0.79 cracks/mm²) was significantly higher compared to the normal side (0.27 ± 0.27 cracks/mm²) in the subchondral region ($p < 0.01$). The weighted mean of the weight percent distribution of calcium (CaMean) also was significantly higher in the

ischemic subchondral region ($p < 0.02$). Furthermore, the nanoindentation modulus within localized areas of subchondral bone was significantly increased in the ischemic side (16.8 ± 2.7 GPa) compared to the normal control (13.3 ± 3.2 GPa) ($p < 0.05$). Taken together, these results support the hypothesis that the nanoindentation modulus of the subchondral trabecular bone is increased in the early stage of ischemic osteonecrosis of the immature femoral head and makes it more susceptible to microcrack formation. We postulate that continued loading of the hip joint when there is a lack of bone cells to repair the microcracks due to ischemic osteonecrosis leads to microcrack accumulation and subsequent subchondral fracture.

3.1 Introduction

Juvenile femoral head osteonecrosis results from a loss of blood flow to the femoral head and leads to a flattening deformity. This disruption of blood flow causes extensive cell death. A lack of bone cells leads to an inability to remodel and repair the damaged bone [160]. Consequently, ischemic osteonecrosis of the immature femoral head can lead to a subchondral fracture and subsequent femoral head collapse [5,15]. Some studies have examined the pathogenesis of subchondral fracture and femoral head deformity following osteonecrosis, but the studies are based on adult patients [161,162]. In a juvenile model of osteonecrosis, one of the mechanisms involved with the pathogenesis of a femoral head deformity is excessive bone resorption [5], which occurs during the revascularization phase of the repair process. During this phase, an increased osteoclastic activity with a decrease in trabecular bone volume is observed. Surprisingly, a significant decrease in the stiffness of the necrotic femoral head and its bony component has been observed in experimental studies even before the revascularization phase when the bone loss occurs [13,14]. In these studies, the whole femoral head was

mounted and indented with a 4 mm spherical indenter. Furthermore, 3.85 mm diameter bone cores with an average length of 4.71 mm that included subchondral and central epiphyseal trabecular bone were removed for uniaxial compressive load testing. The decrease in the mechanical properties was unexpected and prompted an investigation of the material and mechanical properties of necrotic bone before any bone resorption occurs within the femoral head.

Subchondral fracture is one of the earliest radiographic signs seen in patients with juvenile femoral head osteonecrosis [30]. Since it represents the earliest sign of mechanical insufficiency of the infarcted femoral head, it is important to understand the mechanisms underlying the mechanical failure of the subchondral bone that leads to the subchondral fracture. The early mechanical and mineralization changes in the subchondral region have not been elucidated. Several studies have highlighted the role of microdamage in bone homeostasis [160] in the context of metabolic bone disorders, as well as its association with various bone failures [163-165]. The role of microdamage in the development of the femoral head deformity following ischemic osteonecrosis has not been investigated. We hypothesized that ischemic osteonecrosis leads to early mechanical and mineralization alterations in the subchondral region, which predisposes it to fracture. The purpose of this investigation was to assess the subchondral region for changes in histology of bone cells, microcrack number, mineral content, and nanoindentation properties in an early stage of ischemic osteonecrosis (two weeks post ischemia induction) using a well-established large animal (piglet) model of osteonecrosis.

3.3 Materials and Methods

The local Institutional Animal Care and Use Committee (IACUC) approved the study. Eight 5-6-week old Yorkshire male piglets were used. Ischemic osteonecrosis was

induced surgically by transecting the ligamentum teres and placing a ligature tightly around the femoral neck that stops blood flow to the femoral head. The unoperated contralateral side was used as a normal control. All animals were sacrificed at two weeks post ischemia induction when the femoral heads are avascular and no bone resorption is observed [5,13]. Following retrieval, all femoral heads were bisected, fixed in formalin, and stored in 70% alcohol. The femoral heads from five animals were used for microcrack quantification, quantitative backscattered imaging, and nanoindentation testing. Two millimeter sections were obtained from each femoral head of the five piglets. Each section was embedded in methyl methacrylate using standard methods. For nanoindentation and quantitative backscattered imaging, the sections were polished using increasing grades of silicon carbide paper (500, 800, 1200, 2500, and 4000 grit), and polished by 0.25 μm and 0.05 μm diamond suspension. In between each polishing step, the samples were rinsed for 5 minutes in deionized water. The femoral heads from three animals were used for hematoxylin and eosin (H&E) staining and terminal deoxynucleotidyl transferase-mediated dUTP nick end-labelling (TUNEL) assay to assess cell death.

3.3.1 Histological Assessment

Sample preparation for H&E and TUNEL assay have been previously described [166,167]. Briefly, the femoral head samples were decalcified, embedded in paraffin, sectioned 6 μm thick, and stained with H&E or used for a TUNEL assay. Sections from femoral heads pairs, non-operated (left) and operated (right), from three piglets were stained with H&E. DNA fragmentation was detected by performing terminal deoxynucleotidyl transferase-mediated digoxigenin-deoxy-UTP nick end-labelling using the ApopTag Peroxidase In Situ Apoptosis Detection Kit (Intergen, USA). TUNEL

reaction was visualized using diaminobenzidine as peroxidase substrate. Hematoxylin was used as a counterstain. DNase digested cartilage sections were used as positive controls. Normal, unoperated femoral heads from contralateral sides and the sections with omission of terminal deoxynucleotidyl transferase were used as negative controls. Within each section of ischemic femoral head, the unaffected region of the proximal femur, the metaphysis, served as negative internal controls.

3.3.2 Microdamage Assessment

Portions of the femoral head (1.5cm x 1.5 cm x 2 mm thick) were processed for microdamage assessment by bulk staining in calcein [168]. Specimens were transferred from 70% EtOH to 0.9% saline for 5 hours and then soaked in calcein (0.3 gm/100mL saline) for 18 hours under vacuum (20 in Hg). Following calcein staining, bones were washed for 10 minutes with reverse osmosis water and then embedded in methyl methacrylate using standard methods. Central (8 μ m) sections were cut using a Reichert-Jung 2050 microtome (Magee Scientific).

Microdamage quantification was performed using a semiautomatic analysis system (Bioquant OSTEO, Bioquant Image Analysis Co.) attached to a microscope equipped with a florescent light source (Nikon Optiphot 2 microscope, Nikon). Measurements were carried out on two sections per femoral head [169]. A 5 mm² region of interest, located distal to the chondro-osseous junction was used for sampling on each of the two sections resulting in a total tissue area of 10 mm² for each femoral head. Microdamage was assessed using ultraviolet fluorescence. Microcracks were identified by their typical linear shape, relative size (greater than canaliculi, smaller than vascular channels), and positive fluorescence (due to filling of the microcrack with stain), as previously described [170,171]. Microcracks were identified and counted automatically at

100× magnification. Microcrack measurements were performed at 200× magnification. Measurements included crack length (Cr.Le, μm) and crack number (Cr.N), with calculations of crack density (Cr.Dn, $\#/ \text{mm}^2$; Cr.N/bone area) and crack surface density (Cr.S.Dn, $\mu\text{m}/ \text{mm}^2$; Cr.N*Cr.Le/bone area).

3.3.3 Quantitative Backscattered Electron Imaging

A backscattered electron image of the subchondral and calcified cartilage regions was taken at a magnification of 70X for all samples during the same scanning electron microscopy session. An electron beam energy of 25kV and a beam current of 92uA were maintained. The working distance was 10 mm in all cases. The images were used for quantifying distribution of mineralization in bone. The calcified cartilage (0.5mm^2) and subchondral (1 mm^2) regions were analyzed separately. This type of quantification for mineralization in bone has been previously described [7,16]. Briefly, carbon, aluminum, and hydroxyapatite were used as standards to calibrate a bone mineral density distribution (BMDD) from a backscattered electron signal. A calibration line was drawn to correlate the respective gray level values and atomic numbers for each standard. The gray levels were then converted to weight percent of calcium based on the molecular formula of hydroxyapatite, and a BMDD in terms of the weight percent of calcium was generated. The weighted mean of the distribution (CaMean) and the weight percent value with the most frequency (CaPeak) were obtained from each BMDD.

3.3.4 Nanoindentation

The subchondral region of the femoral head bone was identified through an optical microscope and an exposed area of trabecular bone within the region was selected for indentation. A Hysitron Ubi-1 Nanoindenter (Hysitron, Minneapolis, MN) with

a Berkovich tip was used for nanoindentation. A 2x2 mm superolateral area that included the calcified cartilage and subchondral bone regions was consistently identified for all samples for nanoindentation. The location for indentation area was verified by view through the optical camera in the nanoindentation chamber that showed both the Berkovich tip ($r=150$ nm) and the region of interest. A bony structure within the subchondral region was identified. However, the exact location of the indenter tip on the trabecular bone could not be confirmed in relation to its porous structures such as canaliculi and lacunae. A scanning probe microscopy image and respective indentation values were used to verify indentations on subchondral bone (Figure 3.1). The plastic embedding material that surrounded the bone consistently had a reduced modulus less than 7 GPa. The term “reduced” is used to describe the calculation as referenced to the Young’s modulus of the diamond nanoindentation tip. We, thus, analyzed indents above the threshold of 7 GPa. Only indentations with a reduced modulus above 7 GPa were used for statistical analysis as lower moduli were assumed to be indentations in the plastic embedding substrate. One area ($3600 \mu\text{m}^2$) was analyzed per femoral head. At least 21 indentations were analyzed in the area. The following loading function was performed for each indent; ramped to 250 μN at 50 $\mu\text{N/s}$, held for 5 seconds, and then unloaded at 50 $\mu\text{N/s}$. The unloading point of the loading curve was used for reduced modulus (1) and hardness (2) calculations based on the Oliver-Pharr method [6]. The reduced modulus was calculated from

$$E_r = \frac{\sqrt{\pi}}{2} \frac{S}{\sqrt{A_c}}. \quad (1)$$

E_r is defined as the reduced modulus, S as the slope of the most linear part of the upper portion of the unloading curve, and A_c as the projected contact area of the Berkovich tip. The projected contact area of the Berkovich tip was determined by

calibrating the tip at various indentation depths with fused quartz. For hardness, the values are calculated from

$$H = \frac{P_m}{A_c} \quad (2)$$

H is defined as the hardness, which is calculated by the maximum load, P_m , divided by the projected contact area of the Berkovich tip.

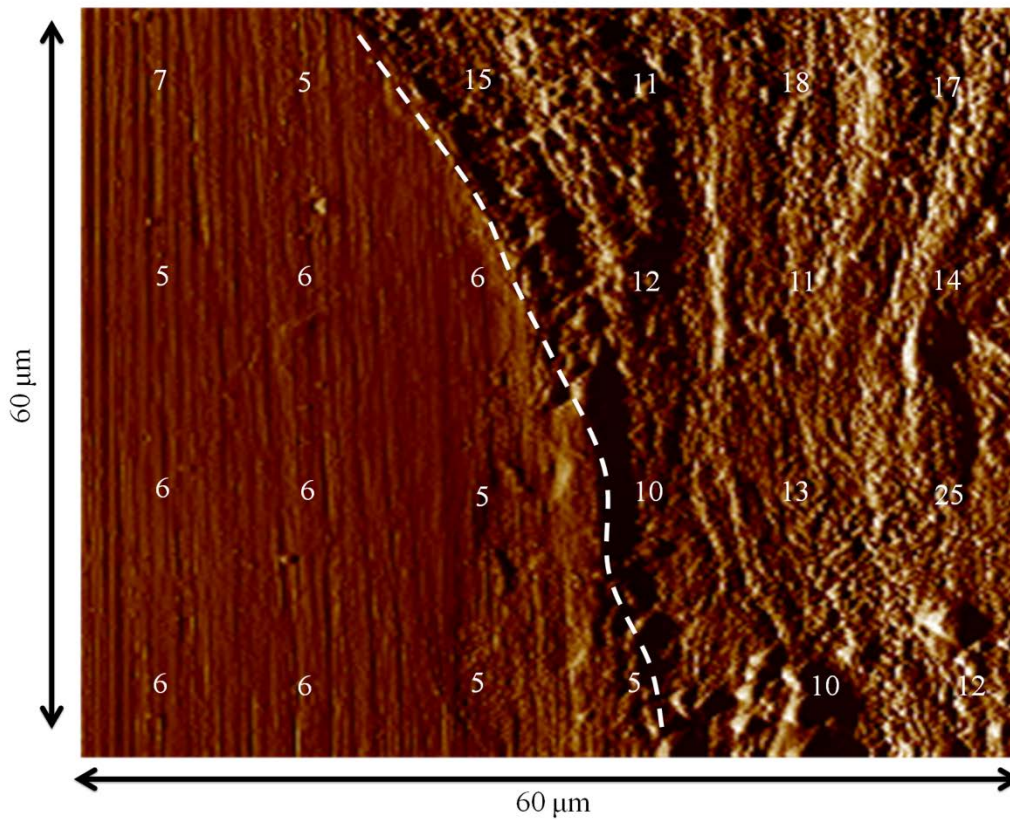


Figure 3.1 A scanning probe microscopy image with a dashed line depicting the plastic-bone interface. The plastic is on the left and the bony area is on the right. The numbers on the image indicate the reduced modulus in GPa units obtained at each respective location.

3.3.5 Statistical Analysis

The crack density (Cr.Dn, $\#/mm^2$) and crack surface density (Cr.S.Dn, $\mu m/mm^2$; Cr.N*Cr.Le/bone area) were averaged for both ischemic (n=5) and normal control (n=5) groups. The averaged reduced modulus of each assessed bony area of the subchondral regions were used to obtain an average for all of the femoral heads in each respective group of ischemic (n=5) and normal control (n=5) femoral heads. More specifically, comparisons were made using averaged nanoindentation values from each head. CaMean and CaPeak values for each respective group were averaged similarly. A Wilcoxon sign-rank test was used. A $p < 0.05$ was defined as being statistically significant.

3.4 Results

Histological comparison of control and ischemic sides (Figure 3.2) showed extensive cell death in the ischemic side with an absence of osteoblasts lining the trabeculae. The finding of extensive cell death in H&E staining was further supported by TUNEL assay which showed diffuse positive staining of the cells in the marrow space and the trabecular bone in the ischemic side compared to the normal control side.

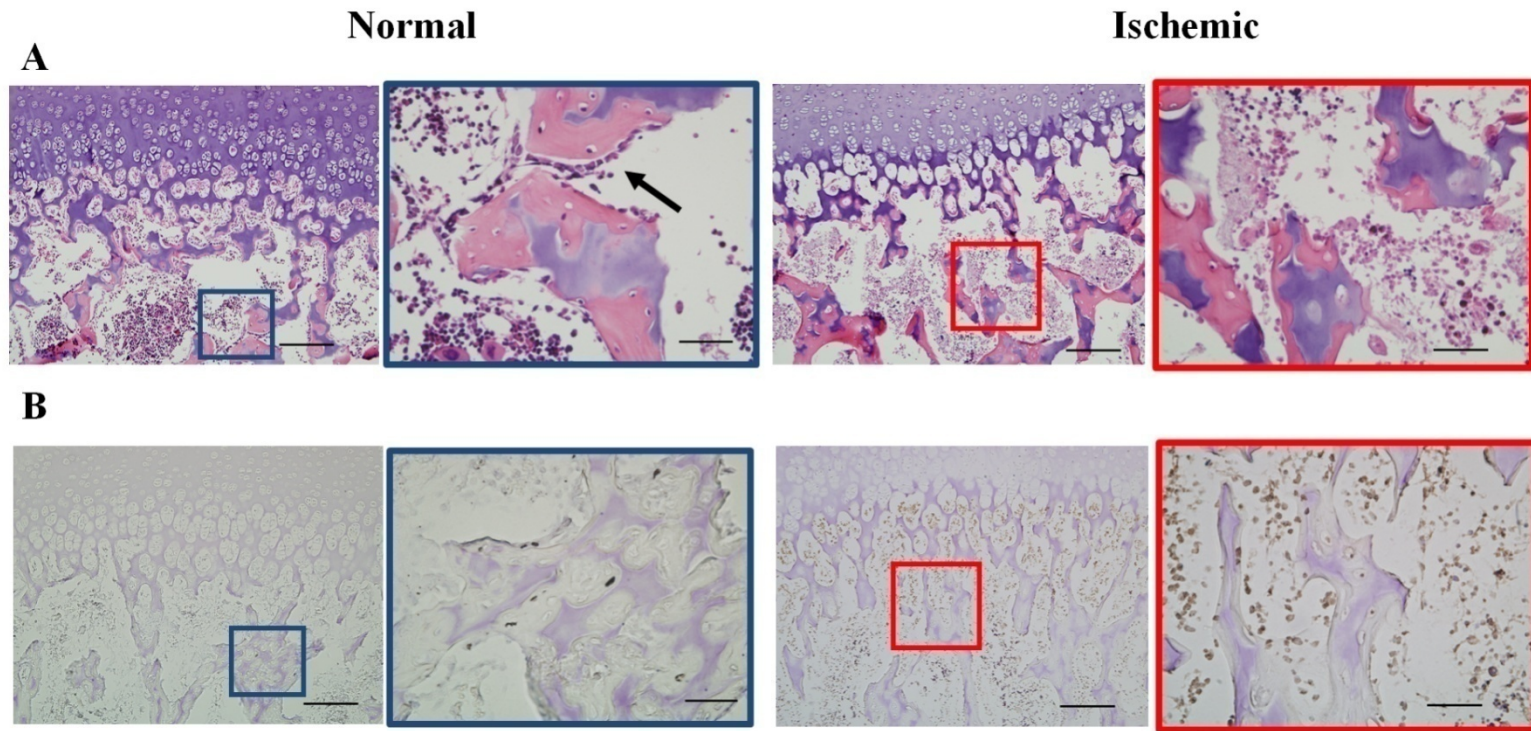


Figure 3.2 (A) The subchondral region of normal and ischemic bone stained with (H&E). An arrow indicates osteoblast lining the trabecular bone of the normal subchondral region. The ischemic side shows a lack of osteoblast lining the trabeculae. B) Normal and ischemic subchondral regions assessed with terminal deoxynucleotidyl transferase mediated dUTP biotin nick end labeling (TUNEL) assay. The normal subchondral region shows a negative TUNEL staining whereas the ischemic bone shows diffuse TUNEL staining of the cells in the bone and the marrow space. The original magnification is 100X (scale bar = 200 μ m). The boxed regions are at 400X magnification (scale bar = 50 μ m).

Microcracks were rarely present in the subchondral region of the normal control sections whereas they were present in significant numbers in the ischemic group (Figure 3.3).

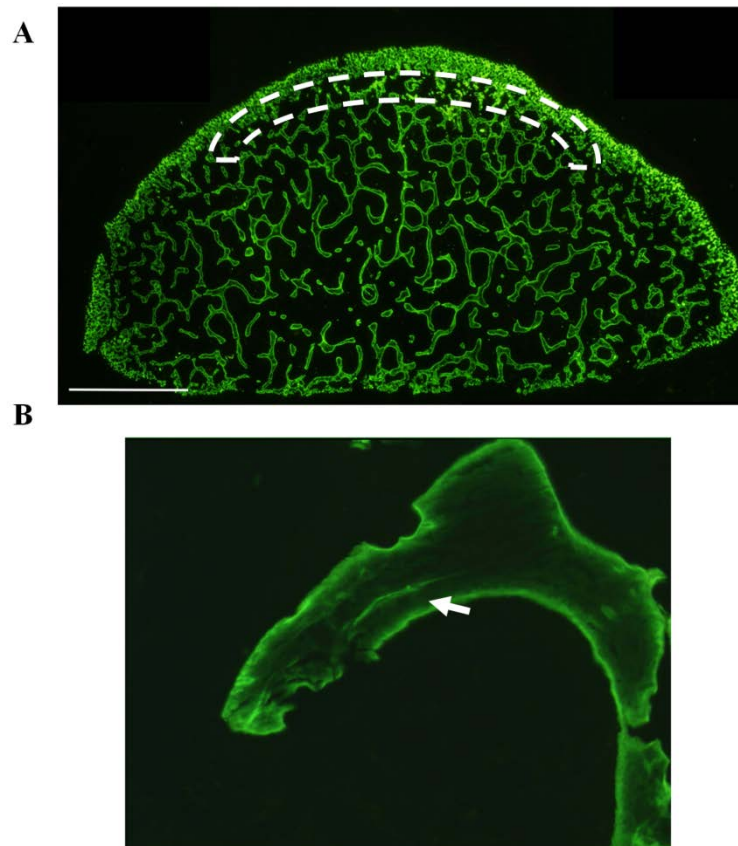


Figure 3.3 (A) Fluorescent microscopy image of the ischemic femoral head stained with calcein captured at 20X magnification. The dashed white line indicates the subchondral region that was assessed for microcracks. (scale bar = 2 mm) (B) shows an image of an individual trabeculae captured at 200X magnification with a microcrack (indicated by an arrow).

The calculated crack density (Cr.Dn, $\#/mm^2$) and the crack surface density (Cr.S.Dn, $\mu m/mm^2$; Cr.N*Cr.Le/bone area) in the subchondral region were significantly increased in the ischemic side compared to the normal control side ($p < 0.01$) (Figure 3.4).

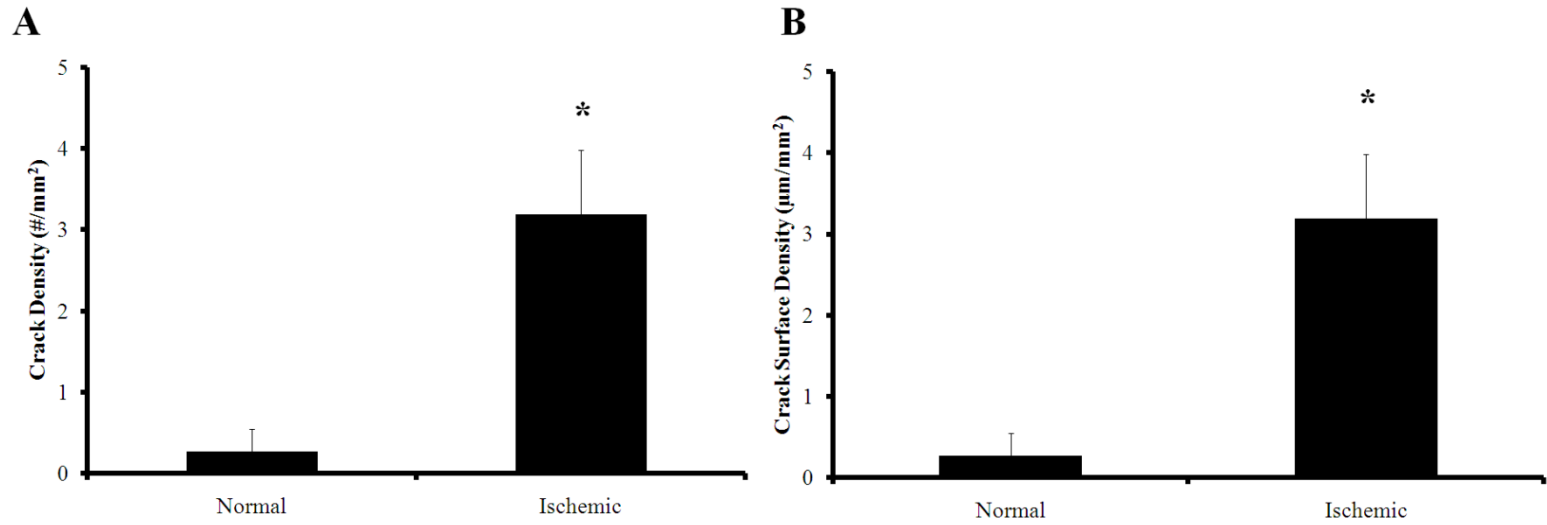


Figure 3.4 Bar graphs showing (A) crack density and (B) crack surface density. These parameters were significantly greater in the ischemic subchondral region compared to the normal side. (*) $p < 0.01$, $n = 5$ per group

Quantitative backscattered imaging showed increased mineralization in the ischemic bone samples. BMDD in each respective pair show a higher calcium weight percent in the ischemic side (Figure 3.5) (Table 3.1). The CaMean was significantly higher in the subchondral ($p < 0.02$) and calcified cartilage regions ($p < 0.0002$) in the ischemic side. The CaPeak was also significantly higher in the calcified cartilage region ($p < 0.0002$) and trends toward significance in the subchondral region ($p = 0.054$).

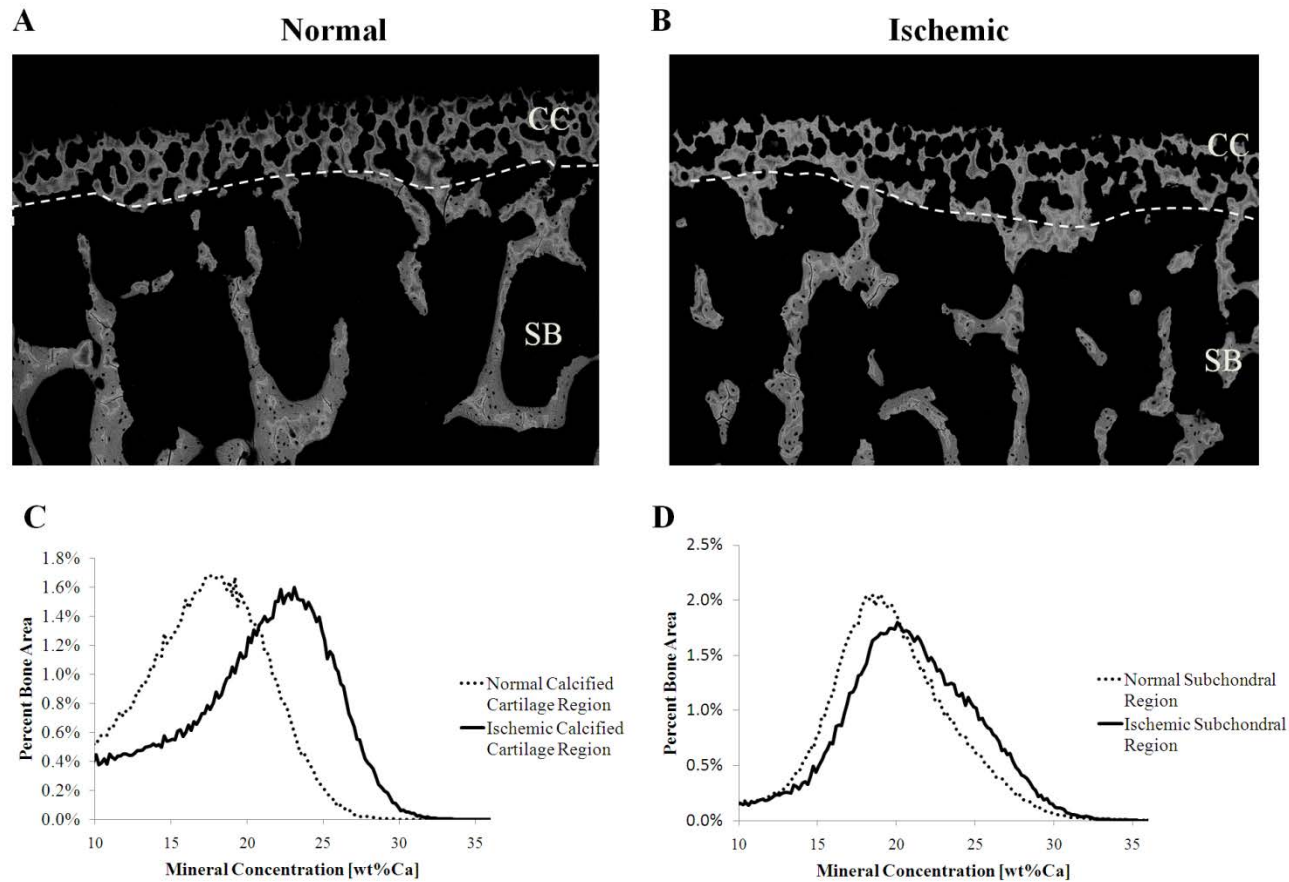


Figure 3.5 (A) Representative normal and (B) ischemic backscattered scanning electron microscopy images. The dashed line in both images separates the calcified cartilage region (CC) and the subchondral bone region (SB). The soft tissue and marrow space was removed by a common threshold and set to a gray level of zero (black). The brightness and contrast of both images were calibrated to show weight percent distribution of calcium. (C) Representative bone mineral density distributions of the calcified cartilage regions and (D) subchondral regions of both normal and ischemic bone.

Table 3.1 The weighted mean of the bone mineral density distribution (CaMean) and the weight percent value with the most frequency (CaPeak) from subchondral bone of each femoral head.

	Calcified Cartilage Region				Subchondral Region			
	CaMean** [wt%Ca]		CaPeak**[wt%Ca]		CaMean*[wt%Ca]		CaPeak†[wt%Ca]	
	Normal	Ischemic	Normal	Ischemic	Normal	Ischemic	Normal	Ischemic
Femoral Head 1	13.8	17.9	17.1	22.1	17.3	18.5	19.2	19
Femoral Head 2	9.1	14.3	14.4	19	16.8	17.3	16.9	17.6
Femoral Head 3	11.5	15.7	15.4	19.2	15.4	18.2	17.2	19.2
Femoral Head 4	14.4	18.2	17.6	23.1	16.9	19.5	18.1	19.4
Femoral Head 5	16	20.4	19.2	23	18.5	19.7	19	20.1
Mean±SD	13.0±2.7	17.3±2.3	16.7±1.9	21.3±2.0	17±1.1	18.7±1.0	18.1±1.0	19.1±0.9

** (p<0.0002)

* (p<0.03)

† (p=0.054)

On average, the penetration depth of the indenter was higher in the normal control (191 ± 11.1 nm) compared to the ischemic nanoindentations (164 ± 16.7 nm) ($p < 0.05$). The load displacement curves of the ischemic subchondral bone showed a shallow penetration depth from indentations when compared to the normal control (Figure 3.6A). Tables 3.2 and 3.3 show averaged reduced modulus and hardness values from each respective femoral head. In both tables, 4 out of 5 ischemic femoral heads showed higher mean values of hardness and reduced modulus. Figure 3.6B shows a typical scatter plot of the reduced moduli found in the subchondral bone. The scatter plot showed a much larger spread in the moduli of the ischemic side (7.2-25.5 GPa) compared to the normal control side (7.1-17.1 GPa). A significant increase in the reduced modulus was found in the subchondral region of the ischemic femoral head compared to the normal femoral head ($p < 0.05$) (Figure 3.6C). The mean hardness value was higher in the ischemic side compared to the normal control side (Figure 3.6D); however, the difference was not statistically significant ($p = 0.13$).

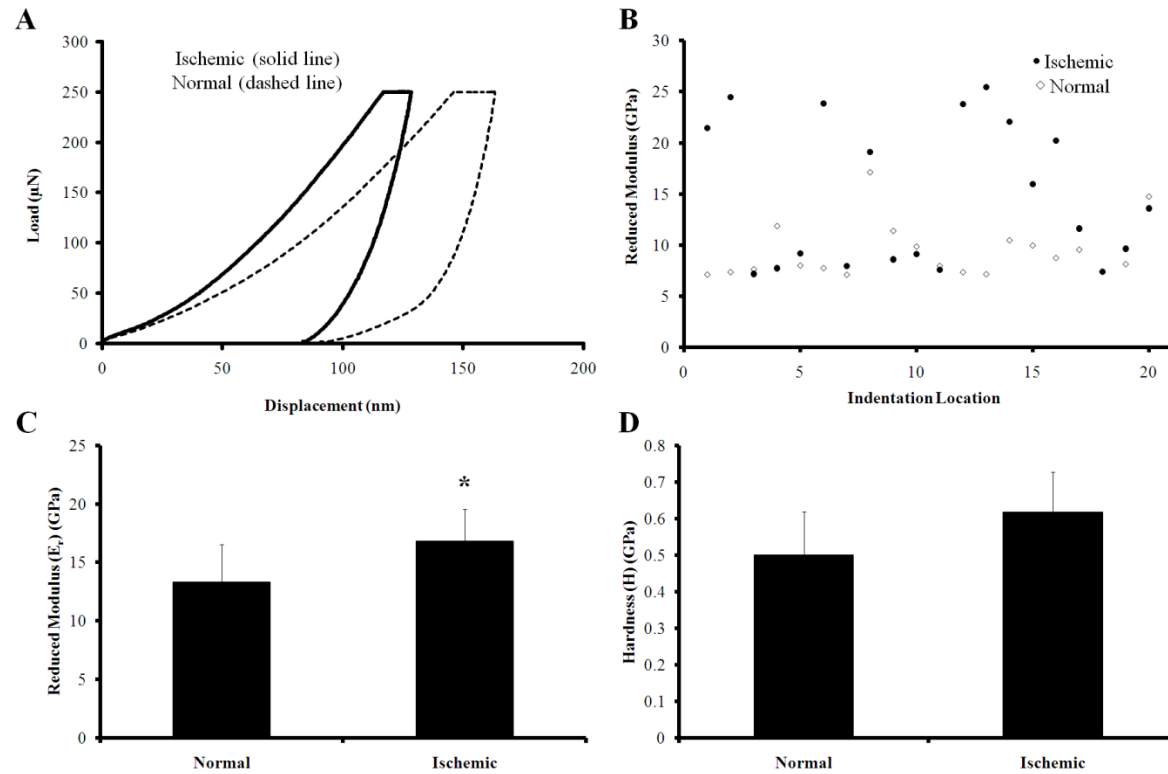


Figure 3.6 (A) A graph showing representative load displacement curves of ischemic (double line) and the normal (single line) bone from the subchondral region. The load displacement curve for normal indentations typically show greater penetration depth compared to the ischemic indentation. (B) A representative scatter plot of the reduced moduli at different locations in both subchondral regions of normal (white diamond) and ischemic bone (black circle). A larger range of moduli is seen in the ischemic bone indentations compared to the normal bone indentations. (C) A graph showing the mean moduli \pm standard deviation of the normal and ischemic groups. The modulus was significantly increased in the ischemic subchondral region compared to the normal side. (*) $p < 0.05$, $n = 5$ per group (D) A graph showing the mean hardness \pm standard deviation of the normal and ischemic groups. The mean hardness was higher in the ischemic side but the difference was not statistically significant.

Table 3.2 The reduced modulus (E_r) from subchondral bone of each femoral head

Femoral Head Pair #	1		2		3		4		5	
	Normal	Ischemic	Normal	Ischemic	Normal	Ischemic	Normal	Ischemic	Normal	Ischemic
Reduced Modulus Mean \pm SD (GPa)	9.3 \pm 2.6	14.6 \pm 6.9	11.4 \pm 2.0	13.7 \pm 4.0	14.0 \pm 4.0	20.3 \pm 6.1	17.8 \pm 5.6	17.9 \pm 7.7	14.0 \pm 3.9	17.8 \pm 6.6
Number of Indents	21	21	22	22	42	42	27	27	50	50
Max	17.1	25.5	15.1	25.3	22.8	38.5	36.4	30.4	23.9	37
Min	7.1	7.2	7.6	7.5	7.1	8.7	10.6	7.3	7.3	8.6

Table 3.3 The hardness (H) from subchondral bone of each femoral head

Femoral Head Pair #	1		2		3		4		5	
	Normal	Ischemic								
Hardness Mean \pm SD (GPa)	0.414 \pm 0.2	0.580 \pm 0.3	0.468 \pm 0.2	0.467 \pm 0.2	0.451 \pm 0.2	0.761 \pm 0.3	0.707 \pm 0.4	0.669 \pm 0.3	0.471 \pm 0.2	0.617 \pm 0.4
Number of Indents	21	21	22	22	42	42	27	27	50	50
Max	1.1	1.28	0.72	0.86	1.02	1.89	2.11	1.42	1.1	1.64
Min	0.2	0.23	0.2	0.21	0.14	0.15	0.29	0.28	0.08	0.13

3.5 Discussion

To date, much of the research on the subchondral region of the femoral head has focused on the specimens from adult patients due to the lack of availability of surgical and pathological specimens from children. Given the scarcity of immature femoral head specimens, the piglet model of femoral head osteonecrosis provided an alternative approach to investigate the early changes in the subchondral region following ischemic osteonecrosis. This study sheds light on the complexity of the mechanical compromise following ischemic osteonecrosis in the immature femoral head which includes increased mineral content, changes in the nanoindentation properties, cell death leading to an inability to repair microdamage, microdamage accumulation, and lack of cells to form new bone. The results of the study support the hypothesis that ischemic osteonecrosis of the immature femoral head leads to an early increase in nanoindentation modulus of the subchondral region and an accumulation of microdamage, resulting in compromise of the mechanical properties of the subchondral region.

The purpose of this investigation was to assess the subchondral region for changes in histologic appearance, microcrack number, mineral content, and nanoindentation properties in an early stage of ischemic osteonecrosis. Histological findings showed diffuse cell death within the marrow space and bone in the subchondral region with an absence of osteoblasts. This region also showed an increased presence of microcracks and increased moduli in the ischemic femoral heads. To our knowledge, this is the first study to describe these findings in the subchondral region of the immature femoral head in an early stage of osteonecrosis. These findings provide further insight into the decrease in the mechanical properties of the femoral head prior to the occurrence of the revascularization phase and bone resorption. They also provide a potential mechanism for the development of a subchondral fracture following ischemic osteonecrosis. Since microcracks develop with normal daily activities, which produce compressive loading of normal cancellous and compact bone [172,173], we believe that daily

loading of the femoral head in absence of bone cells to repair microcracks led to the accumulation of the microcracks and eventual mechanical compromise of the trabecular bone in the infarcted femoral head.

A large accumulation of microdamage in canine femurs has been shown to be associated with a decrease in bone stiffness [163]. In the piglet model of ischemic osteonecrosis, a decrease in the macroindentation stiffness of the infarcted femoral head (indentation measurements using a spherical indenter on the articular surface of the whole femoral head) was found at two weeks post ischemia induction using wet, non-fixed bone [13]. Furthermore, a decrease in the uniaxial compression properties of the bone cores from the infarcted femoral heads was also observed at two weeks post ischemic induction [14]. The reason for the decreases in the mechanical properties, however, was unknown, which prompted us to investigate if an accumulation of microcracks may explain the mechanical compromise. Indeed, the finding of increased presence of microcracks in the subchondral region supports the findings of a decrease in bone stiffness following ischemic osteonecrosis reported in the previous studies [13,14].

Interestingly, the results of nanoindentation testing showed increased nanoindentation modulus of the necrotic trabecular bone in the subchondral region, which seem contrary to the decreased bone stiffness reported previously. The key difference is that the measurements in the previous studies defined the stiffness at a larger scale, testing the regions of the femoral head that included a greater bone volume. The decrease in indentation stiffness in the previous studies was most likely influenced by the presence of microcracks and porosity within the necrotic bony epiphysis. More specifically, the spherical indenter used in the previous study [13] had a much larger interaction volume with the necrotic bony epiphysis due to the size indenter (4mm) and depth of indentation (0.5mm). In this study, the indenter used was many magnitudes smaller and indented at depths reaching ~200 nm in bone. The strain field was limited to the

trabecular bone at a micron scale. In fact, the strain field from nanoindentation of bone has been shown to increase with increasing tip size [174].

The increase in the nanoindentation modulus of the bone is consistent with the finding of increased mineral content of the subchondral bone reported in this study. Similarly, increased mineral content has been reported previously at four and eight weeks post ischemia using the piglet model [16]. An increase in the mineral content of the bone has been shown to be associated with increased stiffness in normal trabecular bone of mandibular condyles in newborn pigs [175], and normal femoral cortical bone in an adult human [176]. Due to increased mineral content in the calcified cartilage and subchondral bone regions relative to the control, higher stress concentrations may be present within the transitional zone of articular cartilage to subchondral bone during normal loading and unloading of the joint.

The reason for increased mineral content can only be speculated. The normal subchondral region has higher cell number to matrix volume due to endochondral ossification. After ischemia induction, the cells in the subchondral region become apoptotic as our results indicate extensive cell death. Apoptotic cells are thought to become more permeable to calcium and phosphate ions leading to cell mineralization [177]. We postulate that higher mineral content of the necrotic bone makes it more prone to microdamage, which may accelerate the process of microdamage accumulation because the bone is less compliant. Positive associations between increased mineral content and microdamage have been observed with both aging and pharmacological treatment [178]. One can further postulate that microcrack accumulation makes the bone more susceptible to fracture in this region. In the piglet model of osteonecrosis, subchondral fractures are observed around four weeks post ischemia induction in some of the animals [15]. Since this study observed the presence of increased microcracks at two weeks post ischemia induction, it is reasonable to speculate that the microcracks will continue to accumulate and eventually lead to a fracture.

This study does have some limitations. Local measurements of nanoindentation properties and microcrack density were done on dehydrated and embedded bone. While dehydration has been shown to increase nanoindentation properties of bone when compared to a hydrated sample of bone [179], this increase in the nanoindentation properties has been shown not to affect comparative trends between samples that are prepared under similar conditions [133]. The samples in both normal and ischemic groups were dehydrated in ethanol and embedded in PMMA under the exact same conditions. While it is unclear whether sample preparation in this study affects ischemic and normal samples similarly, fixation and embedding of samples was assumed to have the same effect on the nanomechanical properties of bone tissue from ischemic femoral heads as it does from normal heads. Furthermore, cracks can possibly develop due to ethanol dehydration [180]. Shrinkage and hardening can occur within the tissue, and without water, internal stresses in the bone may lead to cracking [180]. Again, it is unclear whether the dehydration affects ischemic and normal samples similarly. For the purpose of comparisons, the nanomechanical and microcrack density differences seen between the groups are probable results of ischemic osteonecrosis. We also made sure that the nanoindentations were in a similar location for all samples, and controlled for nanoindentations in the embedding material.

In summary, this study provides new evidence of increased stiffness of the trabecular bone and increased presence of microcracks in the subchondral region of the immature femoral head in the early stage of ischemic osteonecrosis. The results support the hypothesis that early alterations of the material properties of the infarcted femoral head render the subchondral bone more prone to microcrack development, with continued loading of the femoral head leading to microcrack accumulation in the subchondral region and possible fracture.

Chapter 4

Bone Apatite Composition of Necrotic Trabecular Bone in the Femoral Head of Immature Piglets

4.1 Abstract

Ischemic osteonecrosis of the femoral head (IOFH) can lead to excessive resorption of the trabecular bone and collapse of the femoral head as a structure. A well-known mineral component to trabecular bone is hydroxyapatite, which can be present in many forms due to ionic substitution, thus altering chemical composition. Unfortunately, very little is known about the chemical changes to bone apatite following IOFH. We hypothesized that the apatite composition changes in necrotic bone possibly contribute to increased osteoclast resorption and structural collapse of the femoral head. The purpose of this study was to assess the macroscopic and local phosphate composition of actively resorbed necrotic trabecular bone to isolate differences between areas of increased osteoclast resorption and normal bone formation. A piglet model of IOFH was used. Scanning electron microscopy (SEM), histology, X-ray absorbance near edge structure (XANES), and Raman spectroscopy were performed on femoral heads to characterize normal and necrotic trabecular bone. Backscattered SEM, micro computed tomography (μ CT) and histology showed deformity and active resorption of necrotic bone compared to normal. XANES and Raman spectroscopy obtained from actively resorbed necrotic bone and normal bone showed increased carbonate to phosphate content in the necrotic bone. The changes in the apatite composition due to carbonate substitution may play a role in the increased resorption of necrotic bone due to its increase in solubility. Indeed, a better understanding of the apatite composition of necrotic bone could shed light on osteoclast activity and potentially improve therapeutic treatments that target excessive resorption of bone.

4.2 Introduction

Ischemic osteonecrosis of the femoral head can lead to excessive resorption of trabecular bone and collapse of the femoral head as a structure [5,181]. The onset of the

disease results from a lack of blood flow to the femoral head. This deprives the bone cells of the necessary oxygen and nutrients for normal bone formation and causes extensive cell death. We have previously shown in an experimental model of femoral head osteonecrosis, the calcified cartilage and the bone in the subchondral region becomes hypermineralized [16,29]. The absence of viable bone cells for detection and repair of the microcracks in the necrotic head leads to microcrack propagation, accumulation, mechanical weakening and possible subchondral fracture [29]. Indeed, fracture and fragmentation of necrotic bone have been previously described in this experimental animal model [5]. Furthermore, flattening deformities and structural collapse have been shown in other experimental animal models including rats [182], pigs [183], and emus [181]. In addition, at 8 weeks post induction of ischemic osteonecrosis, extensive resorption of necrotic bone and continued weight bearing contribute to the flattening deformity [184].

Along with extensive resorption of necrotic bone, there is some new bone formation. However, newly ossified bone does not form in pace with the extensive resorption of the necrotic bone. To slow down the resorption, targeted treatment of the necrotic bone with bisphosphonates has been shown to decrease osteoclast mediated resorption of necrotic bone relative to non-treated necrotic bone [184], but osteoclast activity in the treated femoral head remains significantly high relative to normal bone. Very little is known about the chemical changes to bone following ischemic osteonecrosis. Hydroxyapatite is a well-known mineral component to trabecular bone and it is known to be present in many forms due to ionic substitution. In fact, various ionic substitutions have been shown to influence osteoclast proliferation [18] and activity [19,20]. A better understanding of the chemistry of necrotic bone could shed light on osteoclast activity and potentially improve therapeutic treatments.

Spectroscopy is commonly used to study the chemistry of materials. For bone apatite, Raman spectroscopy has been used to study mineral crystallinity [185], and compositional variations like carbonate content [186] and carbonate to phosphate ratio [187]. Another

technique known as X-ray absorption near edge structure (XANES) spectroscopy can be used to describe the chemical structures of compounds and the chemistry of an element by providing information on valence, oxidation state, and coordination chemistry, where coordination chemistry can be described as the study of interacting metal ions and ligands. For pathological conditions, XANES has been used to investigate the local environment of Sr^{2+} cations in bone [150], the local environment of Pb and Zn in osteoarthritic cartilage [158,188], and in other pathological conditions [189,190]. XANES has also been used in a study of dried and calcined bone [155] and engineered calcium phosphate bioceramics [191]. Both spectroscopy techniques yield information on composition and structure. We hypothesize that the apatite composition of bone is different in necrotic bone and possibly contribute to excessive resorption and structural collapse of the femoral head. The purpose of this study was to assess the macroscopic and local phosphate composition of actively resorbed necrotic trabecular bone to isolate differences between areas of increased osteoclast resorption and normal bone formation.

4.3 Methods and Materials

4.3.1 Surgical induction of osteonecrosis

The local Institutional Animal Care and Use Committee approved the study. Six piglets (6 to 8 weeks of age, 6 to 8 kg) were used for induction of osteonecrosis. To induce ischemic osteonecrosis of the femoral head, the ligamentum teres of the femoral head was transected and a ligature consisting of #1 Vicryl suture material (Ethicon) was placed tightly around the right femoral neck, as previously described [167]. One and five animals were euthanized respectively at 2 and 8 weeks post surgical induction of osteonecrosis, and the left and right femoral heads were excised and prepared for histology. The left femoral heads were not operated on and served as normal controls.

4.3.2 Histology, Micro-CT and Scanning Electron Microscopy (SEM)

The left and right femoral heads were bisected into anterior and posterior halves, fixed in 10% neutral buffered formalin, dehydrated in increasing grades of alcohol, and embedded in methyl methacrylate (MMA) for sectioning and McNeal tetrachrome staining using standard procedures as previously described [17].

The remaining blocks for two pairs of femoral heads were imaged in the micro-CT and SEM for structural assessment. The blocks were imaged in the micro-CT with a setting of 100kV and 200 μ A at a resolution of 26.6 μ m. A common threshold was used to subtract the soft tissue and plastic embedding media. Furthermore, the blocks were carbon coated for backscattered electron imaging of the subchondral and mid epiphysis of the femoral head. The images were acquired with a setting of 25kV and 93 μ A. A common threshold was also used to subtract the soft tissue and plastic embedding media. The internal lacunar structure of the femoral head at two weeks post surgical induction was analyzed by acid etching and silver sputter coating.

The remaining portion of the embedded bone block of one pair of femoral heads was deplasticized by dissolving the plastic in liquid MMA. After complete dissolution, the portion of the femoral head was transferred to xylene to remove the liquid remnants of MMA, and subsequently transferred between decreasing grades of alcohol from 100% to 70% alcohol where the samples were stored for later use.

4.3.3 X-ray Absorption Near Edge Structure (XANES)

The previously stored samples in 70% alcohol were placed in vacuum chambered desiccators to remove all of the moisture in the samples and to help prevent degassing in the vacuum-sealed chambers of the various beam lines at the Canadian Light Source (CLS). The beam lines include the plane grating monochromator (PGM) for the phosphorous L edge fluorescent yield (FY) XANES spectra, the spherical grating monochromator (SGM) for the oxygen K edge in both total electron yield (TEY) and FY XANES spectra, and finally the soft X-

ray microcharacterization beamline (SXRMB) for the phosphorous K edge TEY XANES spectra. The respective detector, energy range, and step size for spectral acquisition are shown in Table 4.1.

Table 4.1 Experimental setup for spectral acquisition at respective beamlines.

Beamline	Detector	Energy Range	Step Size
Spherical Grating Monochromator (SGM)	Multichannel plate detector	O K-edge: 527 to 552 eV	0.15
Plane Grating Monochromator (PGM)	Multichannel plate detector	P L-edge: 132-154 eV	0.1
Soft X-ray microcharacterization Beamline (SXRMB)	Silicon drift detector	P K-edge: 2140-2190 eV	0.25

The XANES spectra were obtained in the epiphyseal regions of the normal un-operated femoral head, and the necrotic and new ossification (newly formed bone since ischemia induction) regions of the ischemic operated head. To characterize the chemical structure of the femoral head, powdered compounds of known chemical compositions were analyzed to compare to spectra obtained from regions of the femoral head. These model compounds include alpha tricalcium phosphate (α -Ca₃(PO₄)₂), beta tricalcium phosphate (β -Ca₃(PO₄)₂), calcium carbonate (CaCO₃), calcium oxide (CaO), monetite (CaHPO₄), calcium hydrogen phosphate monohydrate (CaHPO₄·H₂O), calcium pyrophosphate (Ca₂P₂O₇), hydroxyapatite (Ca₁₀(PO₄)₆(OH)₂), and chicken bone, which has been previously shown to be an analog to poorly crystalline carbonate containing apatites [155]. The model compounds were chosen to compare distinct features that can be shared with XANES spectra of different regions of the femoral head.

4.3.4 Raman Spectroscopy

Unstained sections on glass slides intended for histological staining were deplasticized in xylene and allowed to dry for mineral characterization in the microspot Raman spectroscopy (DXR, Thermo Scientific, 780 nm, 100 mW, 50 μm slit, 100 \times objective, 30 s exposure). Thirty spectra per location within the trabeculae of normal, necrotic, and newly ossified bone were recorded. Each trabeculae had three locations analyzed avoiding porosities like the lacunae.

4.3.5 Statistical Analysis

The peak intensity ratios of the carbonate (1070 cm^{-1}) to phosphate peaks u_1PO_4 (960 cm^{-1}) and u_2PO_4 (430 cm^{-1}) were averaged for five pairs of femoral heads and grouped under normal, necrotic, and newly ossified bone. A Wilcoxon signed rank test was used to compare the normal and necrotic group, and the newly ossified and normal group. A $p < 0.05$ was considered significant.

4.4 Results

4.4.1 MicroCT, Histology and Scanning Electron Microscopy (SEM)

At two weeks post ischemia induction, the canaliculi structure in the necrotic trabecular bone was discontinuous and lacks interconnectivity between lacunae (Figure 4.1a and 4.1b). At eight weeks, microCT of the necrotic region showed areas of collapse and fragmentation (Figure 4.1c and 4.1d). Indeed, the necrotic region has previously been shown to have significantly decreased trabecular thickness compared to normal trabecular bone and increased bone volume due to continued mechanical loading and compaction compared to non-weight bearing regions [184]. Further analysis by histology of the unoperated contralateral side showed a spherical femoral head with normal bone formation throughout the femoral head (Figure 4.2a). The operated side showed a flattening deformity and resorption of necrotic bone (Figure 4.2b). Higher magnification of the normal bone showed osteoblasts and osteoid which is indicative of

bone formation (Figure 4.2c). Furthermore, the necrotic region of the original epiphysis of the operated side showed trabeculae with large resorption pits and a lack of osteoblasts (Figure 4.2d). However, new ossification within the operated head was noted in the periphery with osteoblasts lining the surface of the bone (Figure 4.2e).

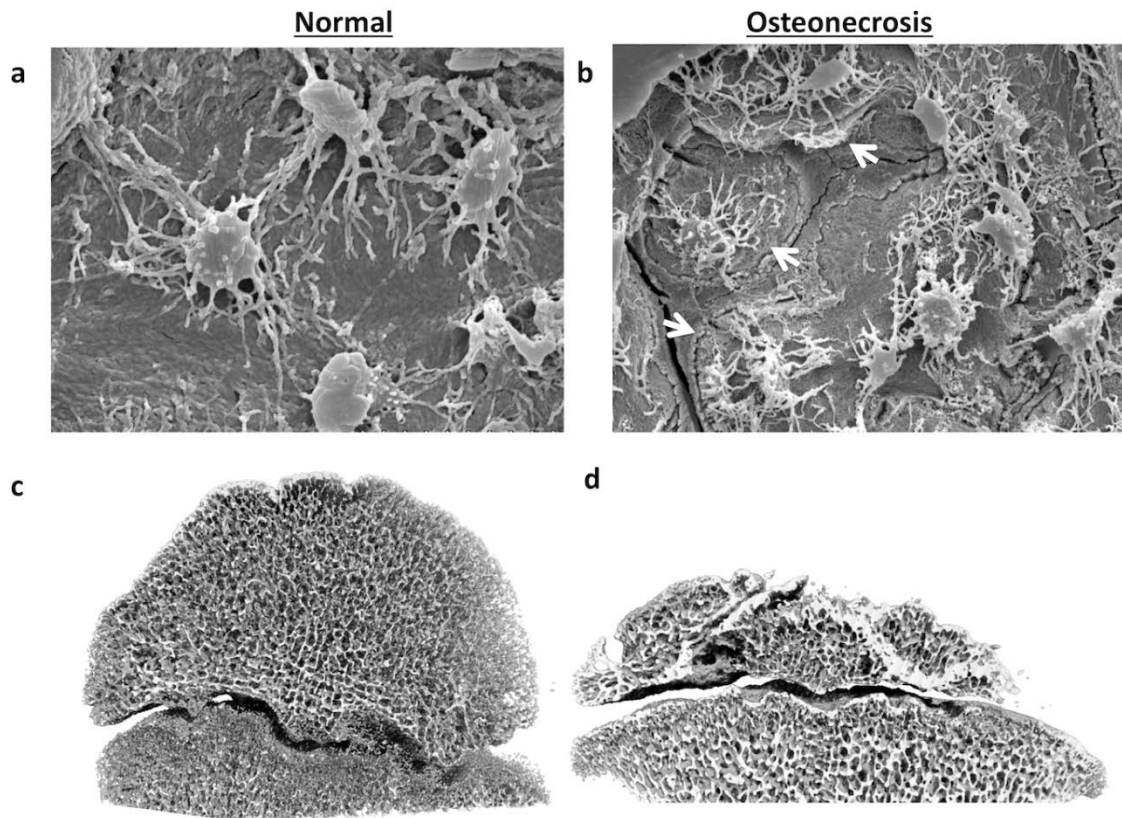


Figure 4.1 Scanning electron microscopy images of (a) normal and (b) necrotic trabecular bone at 2 weeks post-surgical induction of osteonecrosis. The arrows in the necrotic region show discontinuous canaliculi. MicroCT of (c) normal and (d) necrotic femoral head following 8 weeks post ischemia induction.

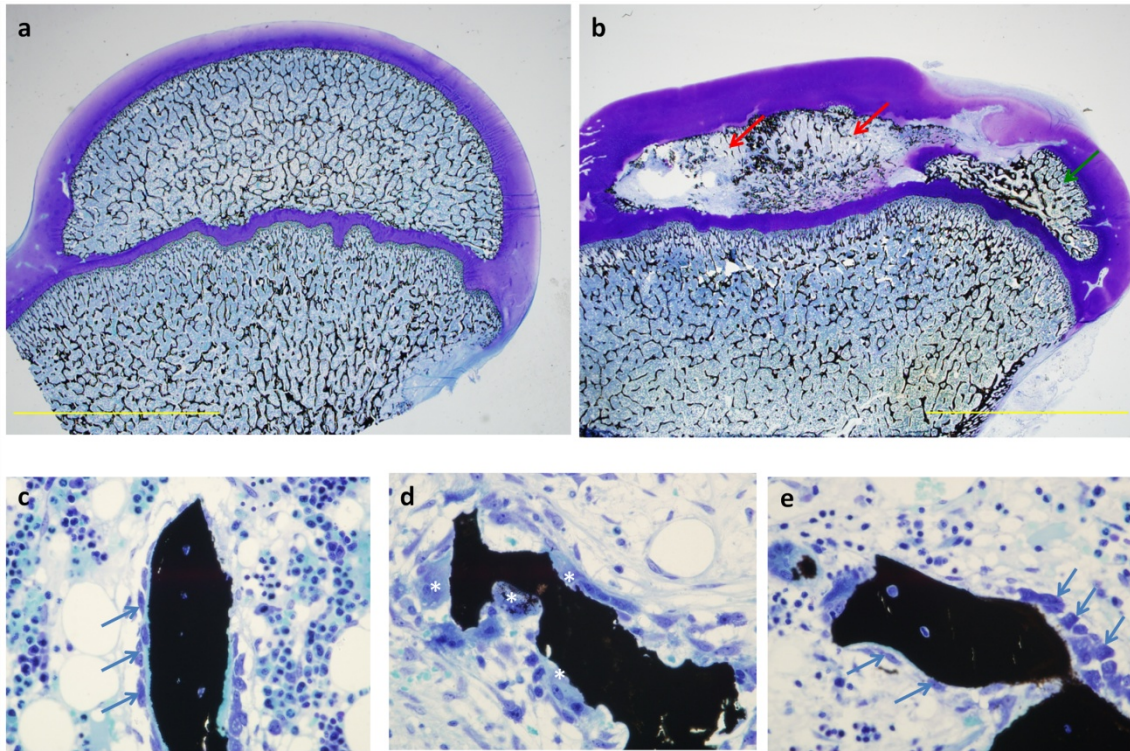


Figure 4.2 Von Kossa and McNeal tetrachrome staining of normal and necrotic bone. (a) The normal coronal section of the femoral head captured at 5X magnification. (b) The necrotic femoral head captured at 5X magnification with resorbed (red arrows) and newly ossified regions (green arrow). Higher magnification of (c) normal trabecular bone with osteoblasts (blue arrows) lining the surface, (d) necrotic trabecular bone with osteoclastic pits (white asterisks), and (e) newly ossified bone with osteoblasts (blue arrows) lining the surface. All higher magnification images were captured at 600X

Backscattered electron imaging showed similar morphometry between the trabecular bone of normal and new ossification (Figure 4.3). However, the necrotic region of the femoral head appeared fragmented with a large separation between other trabeculae. In addition, a higher magnification of the trabeculae in the normal and new ossification regions showed osteoid that is not present in the necrotic fragmented bone.

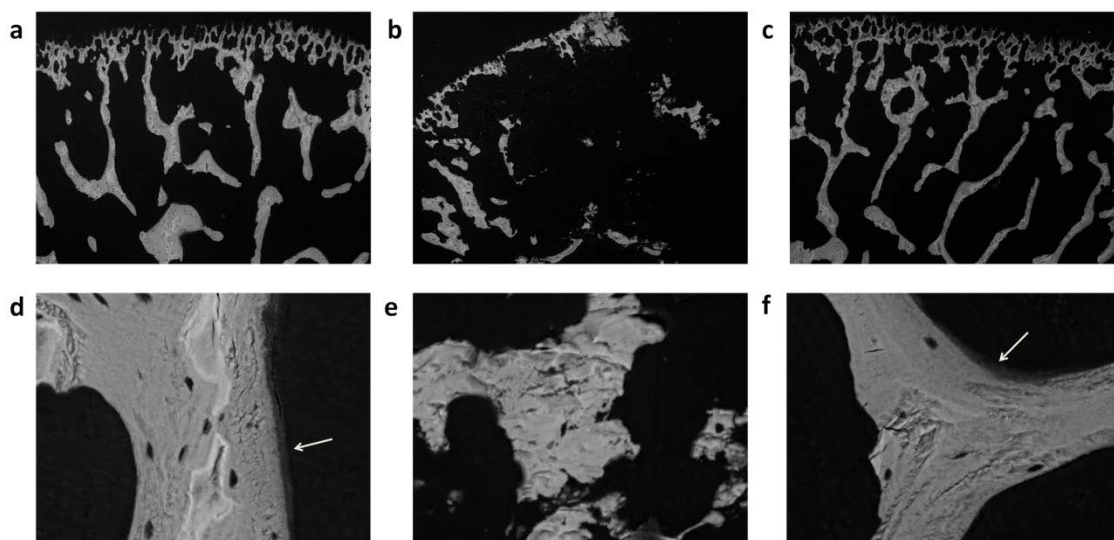


Figure 4.3 Backscattered electron images at 50X magnification of (a) normal femoral head, (b) necrotic portion of the femoral head, and (c) newly ossified regions of the experimental femoral head. Higher magnification images at 550X of (d) normal femoral head, (e) necrotic portion of the femoral head, and (f) newly ossified regions of the necrotic femoral head. The white arrows indicate location of the osteoid seam

4.4.2 XANES analysis

Changes in the chemistry of the different types of bone (normal, necrotic, and newly ossified) were analyzed by X-ray Absorption Near Edge Structure (XANES) spectroscopy. XANES spectra of the normal, necrotic, and newly ossified bone showed contributions of phosphorous and oxygen containing species in the chemical composition of bone. The contributions were assessed by comparing the chemistry of known model compounds with necrotic and normal bone.

4.4.2.1 Phosphorous L-edge FY and K-edge TEY spectra of model compounds and normal, necrotic, and newly ossified regions of the femoral head

The phosphorous L-edge is ideally suited to distinguish between different phosphate compounds of Ca in bone as well as to distinguish between the different cationic species associated with the phosphates [155,191]. The model compounds in Figure 4.4a show pre-edge peaks occurring initially at 136.8 eV for α - $\text{Ca}_3(\text{PO}_4)_2$, followed by the pre-edge peak of β - $\text{Ca}_3(\text{PO}_4)_2$, monetite (CaHPO_4), calcium hydrogen phosphate monohydrate ($\text{CaHPO}_4 \cdot \text{H}_2\text{O}$), calcium pyrophosphate ($\text{Ca}_2\text{P}_2\text{O}_7$), and hydroxyapatite ($\text{Ca}_{10}(\text{PO}_4)_6(\text{OH})_2$). Other features comparing the model compounds between energies 138 and 141 eV show very distinct features for model compounds monetite (CaHPO_4), calcium hydrogen phosphate monohydrate ($\text{CaHPO}_4 \cdot \text{H}_2\text{O}$), and calcium pyrophosphate ($\text{Ca}_2\text{P}_2\text{O}_7$) with secondary pre-edge peaks occurring at varying heights relative to their respective highest peak. In addition, the broad shoulder that was present between energies 141 and 143 eV for $\text{Ca}_{10}(\text{PO}_4)_6(\text{OH})_2$ and β - $\text{Ca}_3(\text{PO}_4)_2$ was absent in remaining model compounds. The normal and necrotic femoral heads were analyzed similarly.

Figure 4.4b shows XANES spectra from regions of the normal and necrotic femoral head. The pre-edge peak occurs at 137.1 eV similar to that of the pre-edge of β - $\text{Ca}_3(\text{PO}_4)_2$. In fact, the overall shape of the XANES spectra from the normal, necrotic, and new ossification regions was similar to that of β - $\text{Ca}_3(\text{PO}_4)_2$. It is important to note that the spectra for all the regions including the normal and necrotic bone have the peak at 148 eV that corresponds to phosphorous coordinated to yield PO_4 anions indicating that even when resorption of bone occurs in necrotic regions the phosphorous remains coordinated as phosphate. Examining the post edge region at 143 eV, the hump in the spectra arises from the promotion of a 2p electron in phosphorous to empty 3d orbitals in Ca and is very prominent in the insoluble phosphates such as β - $\text{Ca}_3(\text{PO}_4)_2$ and hydroxyapatite and less so in more open structured phosphate such as calcium hydrogen phosphates. Hence, it can be concluded that under necrotic conditions the phosphate coordination remains the same and no changes in structure are evident.

The phosphorous K-edge spectra examine the core shell 1s electron and its associated transitions. Other studies in the past have shown that it is well suited to differentiate between different phosphate coordination [155,191]. Figure 4.4c and 4.4d show the phosphorous TEY K-edge XANES spectra of model compounds and regions of the normal and necrotic femoral head. The overall shape between all model compounds shown in Figure 4.4c was generally similar with three peaks at or near 2152.0, 2162.8, and 2170.3 eV. However, most similarities were shared between hydroxyapatite and $\beta\text{-Ca}_3(\text{PO}_4)_2$ due to an additional post-edge peak seen at 2154.8 eV. The spectra from the normal and necrotic regions in Figure 4.4d also appear similar in overall shape and comparable to $\beta\text{-Ca}_3(\text{PO}_4)_2$ and hydroxyapatite, with the necrotic region appearing most comparable to $\beta\text{-Ca}_3(\text{PO}_4)_2$ due to the presence of a post edge shoulder at 2154 eV. This outcome is similar to the phosphorous L-edge spectra that also indicate that there are similarities in the phosphorous coordination in both normal and necrotic regions.

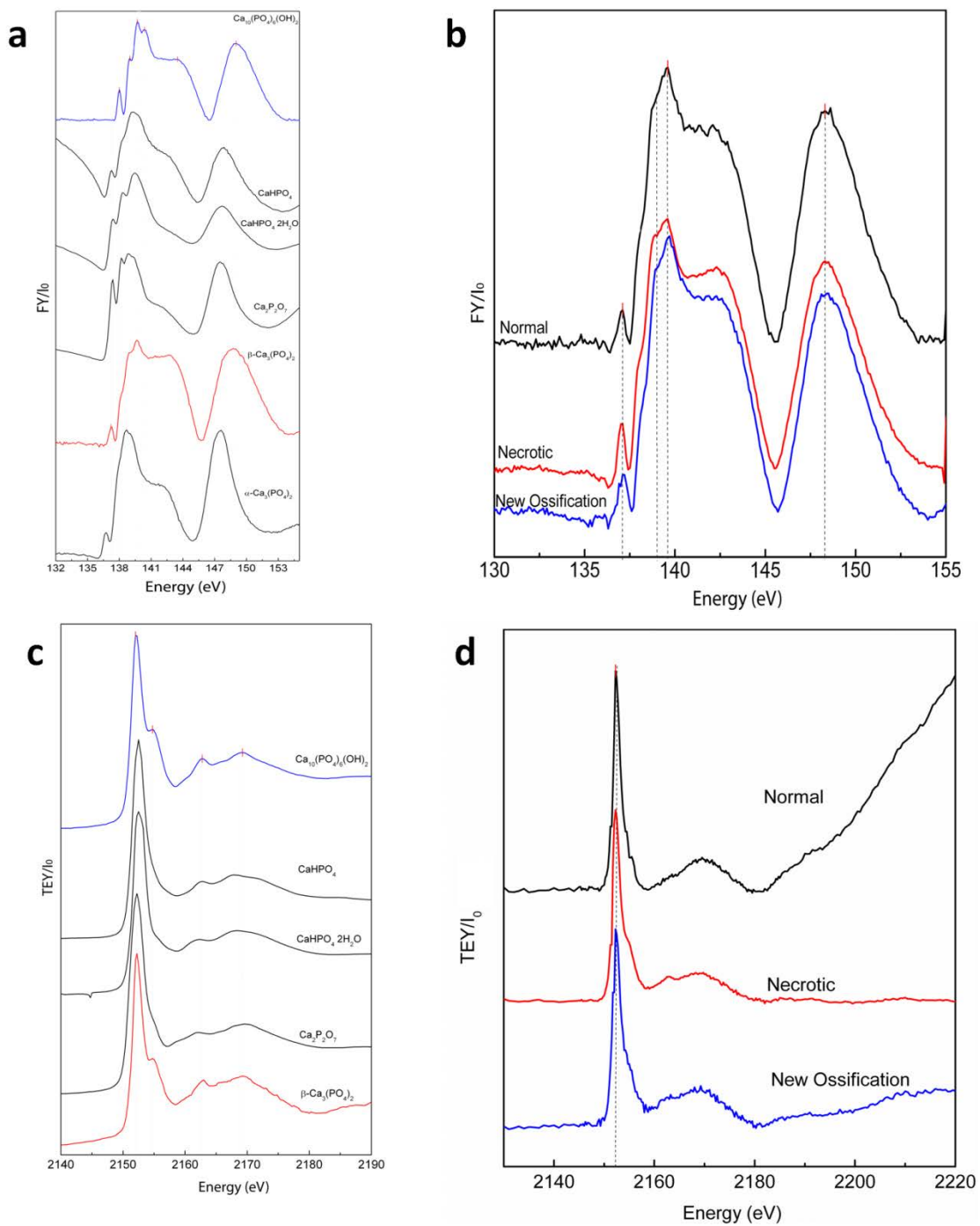


Figure 4.4 (a) Phosphorous TEY L-edge XANES spectra of model compounds. (b) Phosphorous TEY L-edge XANES spectra of normal, necrotic and newly ossified regions of the femoral head. (c) Phosphorous TEY K-edge XANES spectra of model compounds. (d) Phosphorous TEY K-edge XANES spectra of normal, necrotic and newly ossified regions of the femoral head

4.4.2.2 Oxygen K-edge TEY and FY spectra of model compounds and normal, necrotic, and newly ossified regions of the femoral head

The oxygen K-edge spectra are particularly useful to identify the local coordination of oxygen and distinguish between carbonates and phosphates and in particular between different types of phosphates [155]. Figure 4.5a and 4.5b show the oxygen K-edge TEY XANES spectra of model compounds and regions of the normal and necrotic bone. α - $\text{Ca}_3(\text{PO}_4)_2$ and β - $\text{Ca}_3(\text{PO}_4)_2$ in the TEY spectra in figure 4.5a had very similar shape and peak positions, and the same can also be said about the hydroxyapatite except for the peak positions as they generally occurred at higher energies. Other differences include the peak in $\text{Ca}_{10}(\text{PO}_4)_6(\text{OH})_2$ spectra at 534.8, and the 537.3 peak of β - $\text{Ca}_3(\text{PO}_4)_2$ is higher than the 537.3 peak of α - $\text{Ca}_3(\text{PO}_4)_2$ relative to their respective 539.9 peaks. CaCO_3 and CaO have very distinctive features that are absent in the other model compounds. The most significant difference was due to the presence of the first peak at 534.5 eV for CaCO_3 . The chicken bone also had a similar peak shifted 1 eV down at 533 eV. The peak position around 533-534 eV was attributed to the presence of carbonate, and the peak position around 540 eV was attributed to the presence of phosphates. Indeed, the spectra of the normal, necrotic and newly ossified regions in Figure 4.5b show a mixture of carbonate and phosphates. The mixtures were represented as carbonate to phosphate peak height ratios in Table 2, where the necrotic region has the highest carbonate to phosphate ratio.

Figure 4.5c and 4.5d show the model compounds and regions of the normal and necrotic bone respectively in the FY mode. The model compounds shown in Figure 4.5c are very similar to the previously described spectra shown in Figure 4.5a. However, some differences are seen when comparing the spectra from the regions of the femoral head of Figure 5d with Figure 5b. More specifically, the 535.7 eV absorption peak in Figure 4.5b is absent in the FY spectra of Figure 4.5d. Nonetheless, the spectra in Figure 4.5d also show a mixture of carbonate and phosphates, which were represented as carbonate to phosphate peak

height ratios in Table 4.2. The necrotic region has the highest carbonate to phosphate ratio when compared to the normal and newly ossified regions.

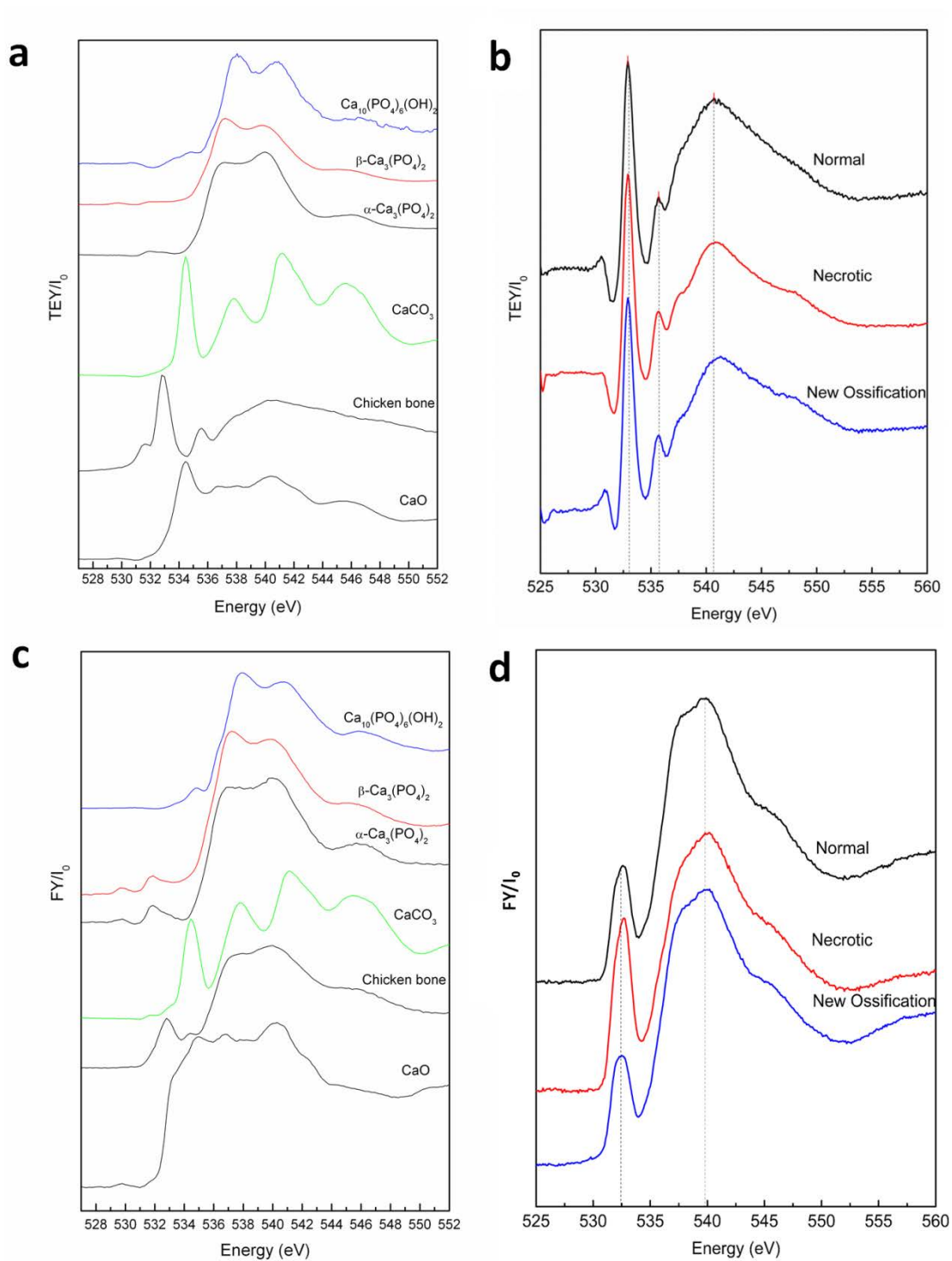


Figure 4.5 (a) Oxygen K-edge TEY XANES spectra of model compounds. (b) Oxygen K-edge TEY XANES spectra of normal, necrotic and newly ossified regions of the femoral head. (c) Oxygen K-edge FY XANES spectra of model compounds. (d) Oxygen K-edge FY XANES spectra of normal, necrotic and newly ossified regions of the femoral head

Table 4.2 Carbonate to phosphate ratios of Total Electron Yield (TEY) and Fluorescent Yield (FY) Oxygen K edge XANES spectra from the Spherical Grating Monochromator Beamline

TEY-Oxygen K-edge	Carbonate to Phosphate Ratio
Normal	1.2
Necrotic	1.4
New Ossification	1.3
FY-Oxygen K-edge	Carbonate to Phosphate Ratio
Normal	0.4
Necrotic	0.7
New Ossification	0.4

4.4.3 Raman Spectroscopy

Raman spectroscopy is particularly suited to study both the soft and hard tissue in bone and has been used extensively in the past to examine hard tissue [192-194]. Normal bone has some carbonate substituted for phosphate in the hydroxyapatite structure and this can be identified by Raman spectroscopy [148]. The carbonate is most likely replacing the phosphate ion in the apatite structure in normal bone and in most cases makes up between 2-6% of the phosphate content [51,195]. In order to determine the extent of substitution of carbonate in the apatite structure the Raman spectroscopy was also used. Figure 4.6a shows representative spectra of normal, necrotic, and newly ossified bone. The peak intensity ratio between the carbonate (1070 cm^{-1}) and phosphate peaks $\nu_1\text{PO}_4$ (960 cm^{-1}) and $\nu_2\text{PO}_4$ (430 cm^{-1}) were used to estimate the relative amounts of carbonates to phosphates and were lowest for newly ossified bone and highest for necrotic bone. In fact, the carbonate to phosphate ratio was

significantly higher in the necrotic versus normal bone and necrotic versus new ossification ($p < 0.05$) (Figure 4.6b and 4.6c).

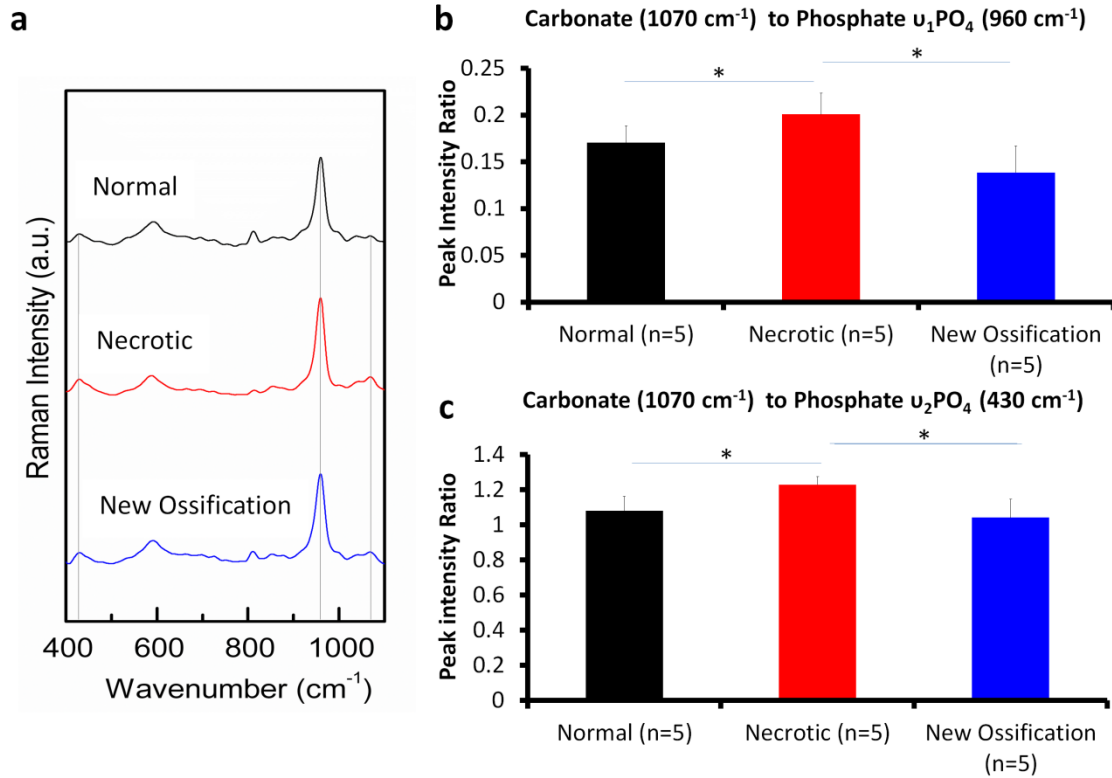


Figure 4.6 Representative Raman spectroscopy of normal, necrotic, and newly ossified bone. (b) Bar graphs of the carbonate (1070 cm^{-1}) to phosphate peaks u_1PO_4 (960 cm^{-1}) and (c) and u_2PO_4 (430 cm^{-1}) ratio pooled from 5 femoral pairs. The data is represented as mean \pm standard deviation. (* $p < 0.05$)

4.5 Discussion

The purpose of this study was to identify differences in the local chemistry of necrotic bone in comparison to the normal bone during the resorptive phase of healing of the necrotic bone. The histological findings highlight the flattening deformity and fracture that occur following 8 weeks of ischemia induction. Furthermore, the histological assessment of the necrotic femoral head showed extensive resorption of the original epiphysis and new ossification in the

periphery. In addition, further analysis of the microstructure by backscattered SEM reveal fragmented and heavily resorbed bone in the original epiphysis. The presence of the osteoid seams in the normal and new ossification regions show some evidence of continuous bone formation, while the necrotic bone undergoes excessive resorption. XANES assessment of the bone chemistry showed no change in the local coordination of phosphorous between the normal, necrotic and newly ossified regions, but an increased contribution of carbonate in the necrotic region.

The carbonate phosphate complex in XANES spectra of bone has been previously analyzed in various bone samples of sheep, deer, bovine, and chicken, by Rajendran et al. They attribute the carbonate phosphate complex to the substitution of phosphate ions by carbonate [155]. They compared the peaks of calcium carbonate standard to the calcined bone samples of animals such as sheep, deer, bovine, and chicken and noted a downward shift in the comparable peaks to lower energies. Indeed, our spectra data is in agreement with the downward peak shifts seen by Rajendran et al when comparing the various regions of the femoral head to the calcium carbonate standard. Based on the model compound standards and likely shifts of peak energies due to the local coordination of oxygen within the bone, the contribution of carbonate and phosphate in the femoral head were unique to the 533 and 540 eV peak, respectively, and provided a relative assessment of the amount of carbonate.

The presence of carbonate in bone has been well studied with Fourier transform Infrared spectroscopy, in which phosphate can be substituted with either the hydroxyl groups or carbonate ions. In aging bone, the phosphate group has been shown to preferentially substitute with the hydroxyl groups at the interface of a growing crystal [143]. However, others have shown that phosphate substitution occurs with carbonate ions [196]. The key differences between the preceding studies lie in structural assessment of bone, which is well discussed by Paschalis. Briefly, one group analyzed homogenized bone whereas the other analyzed single osteons isolating newly formed mineral and older mineral. Our XANES analysis combines a

mixture of the two methods. While our bone samples were not homogenized, we were only able to measure the XANES spectra from specified regions of the femoral head, and we were unable to spectrally resolve the contribution from isolated sites of the trabeculae within the region. In addition, the FY XANES spectra averages more information into the substrate at 1-3 microns, than the TEY XANES spectra which is more surface sensitive at 30 -70 nm into the substrate. Hence, the XANES spectra resolved, showed increased carbonate mostly from the bulk of the identified regions. While carbonate substitution can occur with hydroxyl groups, the FY spectra suggest that it occurs mostly interstitially with phosphate ions.

We used Raman spectroscopy on previously embedded bone to further investigate the presence of carbonate in bone and found increased carbonate to phosphate content in necrotic bone. Previous analysis of carbonate to phosphate ratios have been shown to be unaffected by fixation and embedding with MMA [197]. The embedding and fixation process by Yeni et al. involved obtaining cortical bone from mice, fixation in glycerol, dehydration in ethanol, immersion in xylene, and embedding in PMMA. We similarly processed the samples but use trabecular bone from pigs and a formalin fixative. While the specific effect of the formalin fixation as opposed to glycerol fixation on pig trabecular tissue has not been investigated, we expect similar processing of normal and necrotic tissue samples to affect the bone apatite similarly. More specifically, we believe the increase of carbonate to phosphate content in necrotic bone to be independent of tissue processing.

Increasing carbonate substitution with phosphate ions has been measured with Raman spectroscopy in aging bone [198]. Akkus et al. used cortical bone from young and old rats and found positively correlated changes in increased carbonate substitution with phosphate ions and decreased structural and material level mechanical properties. More specifically, they suggested the carbonate substitution related to shape changes in the crystal structure caused by vacancies [199]. In our study, the carbonate to phosphate ratios was found to be highest in XANES and Raman spectra of necrotic bone. We believe the increased carbonate is likely a

result of the fact that bone is relatively older than other analyzed regions that were undergoing active bone formation. Furthermore, it is reasonable to speculate that the local distortions in the crystal structure due to carbonate substitution are contributing factors to the fracture of necrotic bone.

The fragmentation, separation, and excessive resorption of increased carbonated necrotic bone can only be speculated at this time. In these regions, the bone has been shown to have a significantly large amount of osteoclast activity, and it has been stated that this increase in osteoclast activity produces excessive bone loss, which contributes to the flattening deformity in the face of continued weight bearing. The reason for the preferential osteoclast activity and attachment on the bone as opposed to osteoblast activity is not well understood. However, carbonated apatite as opposed to noncarbonated apatite is more soluble [200], and thus easier to break down. Indeed, the role of carbonate content in bone and dental pathophysiology is evident [144,201,202], where the increase in carbonate content has been hypothesized to be influenced by tissue age, mineral content, and eventual release by osteoclast resorption. Furthermore, in vitro characterization of osteoclast-like activity on carbonated substituted hydroxyapatite was significantly increased when compared to hydroxyapatite and trends higher when the carbonate content is increased [19].

Future studies are needed to investigate the role of carbonate in necrotic bone. Isolating the spectral contribution at specified locations interfacing with osteoclasts and necrotic bone may shed more light on the cellular contributions to increased carbonate. In addition, analysis of necrotic bone at earlier time points preceding excessive resorption and vascular return may also give a clearer picture on the role of carbonate.

4.6 Conclusion

In this study we have examined the changes in the chemistry of normal and necrotic bone in a porcine model using XANES and Raman spectroscopy. We have determined that

there is not much of difference in the phosphorous coordination between normal, necrotic and newly ossified bone and the major difference in chemistry arose from the amount of carbonate that substituted in the apatite structure. Newly ossified bone had the smallest amount of carbonate while the necrotic bone had the largest amounts of carbonate in the apatite structure. Local changes in the apatite structure due to carbonate substitution may play a role in the increased resorption of necrotic bone due to its increase in solubility.

Chapter 5

Material properties of femoral head treated with local administration of anti-resorptive and bone anabolic agents following the induction of ischemic osteonecrosis:

Experimental Investigation in Immature Pigs

5.1 Abstract

Legg-Calvé-Perthes disease (LCPD) is a juvenile hip disorder attributed to the loss of blood flow to the bony epiphysis that causes osteonecrosis (bone death) of the femoral head. A permanent femoral head deformity from fracture, bone fragmentation, and collapse of the femoral head are complications associated with LCPD. Early material changes such as increased mineral content and nanoindentation modulus have been identified in an immature piglet model of ischemic osteonecrosis. Treatment aims to not only retain the sphericity of the femoral head, but also to promote bone healing to help prevent collapse. We hypothesized that treatment with anti-resorptive and anabolic agents will affect the mineral content and nanomechanical properties due to new bone formation and repair. The purpose of this study was to determine the effects of BMP-2 and ibandronate, a well-known bisphosphonate, on the material properties of bone after ischemic osteonecrosis of the femoral head. The right femoral head of twenty piglets (6 to 8 weeks of age, 6 to 8 kg) was used for induction of osteonecrosis. Femoral heads without treatment were compared to ibandronate (IB), bmp-2 (BMP), and BMP+IB treated groups. The left femoral head of the no treatment group was used as a normal control. Histology was used to identify revascularized regions of bone repair. Quantitative backscattered electron imaging (qBEI), Raman spectroscopy, and nanoindentation were used to measure the material changes in mineralization, composition, and mechanical properties. Histological assessment showed revascularized tissue in all groups. New bone in the BMP and BMP+IB groups was identified by McNeal and H&E sections revealing new bone surrounding old necrotic bone, while the IB group showed no osteoblast and the no treatment group showed osteoclastic resorption of necrotic bone. CaMean and CaPeak measured by qBEI were

significantly increased in the no treatment and IB groups compared to normal ($p < 0.03$), and no significant difference was found for BMP and BMP+IB groups compared to normal. Carbonate content measured relative to phosphate and matrix bands showed significantly increased content in the necrotic ($p < 0.01$) and IB groups ($p < 0.005$) compared to normal, and no significant difference was found for the BMP group compared to normal. However, carbonate relative to phosphate band was increased in the BMP+IB group compared to normal ($p < 0.005$). The nanoindentation modulus within the IB treated trabecular bone was significantly increased compared to the normal trabecular bone ($p = 0.024$) with no significant differences seen in the BMP and BMP+IB treated group compared to normal. Hardness measurements in the IB treated group were also significantly increased compared to BMP, and BMP+IB treated groups ($p \leq 0.02$). Taken together, the results support the hypothesis that treatment aided by BMP-2 better normalizes the material properties of bone post ischemia with new bone formation. We postulate new bone formation around the necrotic bone can provide added mechanical strength to help prevent fracture and collapse of the bone during juvenile femoral head osteonecrosis.

5.2 Introduction

Legg-Calvé-Perthes disease (LCPD) is a juvenile hip disorder attributed to the loss of blood flow to the bony epiphysis that causes osteonecrosis of the femoral head. The development of a permanent femoral head deformity is a common complication of LCPD, with half of the patients developing osteoarthritis [111,112]. Due to a lack of pathological specimens, an experimental model of osteonecrosis of the femoral head in piglets has previously been studied [5]. The model develops a moderate to severe flattening deformity that is also present in some patients diagnosed with LCPD. Extensive resorption of necrotic bone has been shown to lead to collapse and deformity of the femoral head; for that reason, balanced bone formation and resorption aided with treatment are expected to help maintain shape of the femoral head during the healing process.

Bisphosphonates and bone morphogenic proteins (BMPs) have previously been used as treatment in experimental models of femoral head ischemia [24,25]. Bone morphogenic proteins are multifunctional growth factors that play a pivotal role in inducing bone formation; their structure, function, signaling, and applications have been reviewed extensively [203,204]. Briefly, there are 20 family members of BMP, of which BMP-2, 4, 5, 6, and 7 have the greatest osteogenic capacity. BMP-2 due to its key role in osteoblastic differentiation has been used in many applications to stimulate bone formation after ischemia [205], necrosis [206], and fracture [207-210]. On the other hand, bisphosphonates bind to bone mineral and deposit where bone is formed and resorbed to help decrease the resorption of bone. Several mechanisms of actions have been reviewed by [211-213]. Briefly, bisphosphonates can reduce bone resorption by performing a number of actions: inhibiting osteoclastic recruitment to the bone surface, inhibiting osteoclastic activity on the bone surface, decreasing the life span of osteoclasts, and changing the bone mineral rate of dissolution by osteoclasts.

Bisphosphonates and BMPs can be used for their respective anti-resorptive and anabolic capabilities. While these treatments have proven beneficial in maintaining bone volume, supporting bone formation, and sphericity in the experimental animal model of osteonecrosis of the femoral head [24,25], appropriate qualifiers are needed to assess the material properties of bone after treatment and to assess certain indicators that are contributors to future problems like microdamage and fracture. Without treatment, the experimental model of osteonecrosis of the femoral head has previously been shown to develop microcracks[29], subchondral fracture[15], and apparent fragmentation of necrotic bone[5], in addition to material changes resulting from increased mineral[16] and carbonate content[31]. With treatment, stimulated bone repair and formation while the bone is revascularized are expected to help maintain shape of the femoral head during the healing process. However, the use of BMP in combination with bisphosphonate on material changes has not been investigated. More specifically, the effect of the combinatory treatment with BMP and bisphosphonates on bone

composition and nanomechanical properties after ischemia has not been investigated. We hypothesized treatment with a bone anti-resorptive agent and/or bone anabolic agent will affect the mineral content and nanomechanical properties due to new bone formation and repair. The purpose of this study was to determine the effects of BMP-2 and ibandronate, a well-known bisphosphonate, on the material properties of bone after ischemic osteonecrosis of the femoral head during the revascularized healing stage of the disease.

5.3 Materials and Methods

5.3.1 Surgical induction of osteonecrosis

Femoral heads were obtained from previously approved IACUC studies. They were femoral heads from twenty animals that were of similar age and weight received surgical induction of osteonecrosis by the same surgeon. The femoral heads were split into four groups (n=5/group): no treatment, ibandronate (IB), bmp-2 (BMP), and BMP+IB. To induce ischemic osteonecrosis of the femoral head, the ligamentum teres of the femoral head was cut and a ligature consisting of #1 Vicryl suture material (Ethicon) was placed tightly around the right femoral neck, as previously described [167]. Animals within the IB, BMP, and BMP+IB groups received an intraosseous injection in the ischemic femoral head. All animals were euthanized 8 weeks post-surgical induction of osteonecrosis when revascularization is expected [5,214]. The right femoral heads were excised and prepared for histology, and the left femoral head of the no treatment group was used as normal controls.

5.3.2 Histology

The femoral heads were bisected into anterior and posterior halves and fixed in 10% neutral buffered formalin. After fixation, the anterior half of the femoral head was decalcified with Ethylenediaminetetraacetic acid (EDTA) and processed for paraffin embedding. The posterior half was dehydrated in increasing grades of alcohol and embedded in methyl methacrylate

(MMA) for sectioning and McNeal tetrachrome staining using standard procedures as previously described [17].

Tissue sections from the anterior half were stained with a hematoxylin and eosin (H&E) stain, as the posterior half was cut into thin sections and stained with von kossa and McNeal tetrachrome stain. Areas of revascularization and bone formation were identified based on the presence of vessels and osteoblasts.

5.3.3 Quantitative Backscattered Electron Imaging (qBEI)

After sectioning of the MMA embedded blocks, the blocks were polished with increasing grades of silicon carbide paper (1200, 2400, and 4000 grit). In between each polishing step, the blocks were rinsed ultrasonically in deionized water. The blocks were polished sequentially with a 0.25 μm and 0.05 μm diamond slurry and carbon coated for SEM imaging. Backscattered electron images of the mid-epiphyseal region of the femoral head was taken at a magnification of 50X for all samples. A beam energy of 20kV and a beam current of 92 μA were maintained. The working distance was 15 mm. The images were used for quantifying distribution of mineralization in bone. Quantification for mineralization in bone has been previously described [7,16]. Briefly, carbon, aluminum, and hydroxyapatite were used as standards to calibrate a bone mineral density distribution (BMDD) from a backscattered electron signal. A calibration line was drawn to correlate the respective gray level values and atomic numbers for each standard. The grey levels were then converted to weight percent of calcium based on the molecular formula of hydroxyapatite, and a BMDD in terms of the weight percent of calcium was generated. The weighted mean of the distribution (CaMean) and the weight percent value with the most frequency (CaPeak) were obtained from each BMDD.

5.3.4 Raman Spectroscopy

After qBEI imaging, the carbon coat was removed with 4000 grit silicon carbide paper. Trabecular bone from revascularized regions was identified with the optical microscope of the Raman microscope using corresponding McNeal slides. Compositional characterization of the trabecular bone was performed with the microspot Raman spectroscopy (DXR, Thermo Scientific, 780 nm, 100 mW, 50 μm slit, 100 \times objective, 30 s exposure). Thirty spectra per location within the trabeculae of normal, necrotic, and treated groups (IB, BMP, and BMP+IB) were recorded between 400 and 2000 cm^{-1} . Across each trabecular cross-section, at least five locations were analyzed avoiding porosities from lacunae. From the spectra, the peak areas of phosphate $\nu_1\text{PO}_4$ (930 - 980 cm^{-1}), carbonate (1050–1100 cm^{-1}), and matrix collagen amide I (1620 - 1700 cm^{-1}) were measured. Ratios of these peak areas resulted in measures of carbonate to phosphate, phosphate to amide I, and carbonate to amide I.

5.3.5 Nanoindentation

Revascularized regions within the epiphysis were identified based on corresponding histological sections. Trabecular bone was identified through an optical microscope, and an exposed area of trabecular bone within the revascularized region was selected for indentation. A Hysitron Ubi-1 Nanoindenter (Hysitron, Minneapolis, MN) with a Berkovich tip was used for nanoindentation. The location for the indentation area was verified by view through the optical camera in the nanoindentation chamber that showed both the Berkovich tip and the region of interest. A bony structure within the revascularized region was identified. However, the exact location of the indenter tip on the trabecular bone could not be confirmed in relation to its porous structures such as the canaliculi and the lacunae. Indentation in embedding material was excluded based on the measured moduli as previously described [29]. Briefly, indentations with a reduced modulus above 7 GPa were used for analysis as lower moduli were indentations in the plastic embedding substrate. An area of at least 3600 μm^2 was analyzed per femoral head.

At least 30 indentations were analyzed in the area. The following loading function was performed for each indentation: 1) ramped to 500 μN at 50 $\mu\text{N/s}$, 2) held for 5 seconds, and then 3) unloaded at 50 $\mu\text{N/s}$. The unloading point of the loading curve was used for reduced modulus (1) and hardness (2) calculations based on the Oliver-Pharr method [6]. The reduced modulus was calculated from

$$E_r = \frac{\sqrt{\pi}}{2} \frac{S}{\sqrt{A_c}}. \quad (1)$$

E_r is defined as the reduced modulus, S as the slope of the most linear part of the upper portion of the unloading curve, and A_c as the projected contact area of the Berkovich tip. For hardness, the values are calculated from

$$H = \frac{P_m}{A_c}. \quad (2)$$

H is defined as the hardness, which is calculated by the maximum load, P_m , divided by the projected contact area of the Berkovich tip.

5.3.6 Statistical Analysis

Peak area ratios of the carbonate (1070 cm^{-1}) to phosphate (961 cm^{-1}), mineral (960 cm^{-1}) to matrix (1665 cm^{-1}), and carbonate (1070 cm^{-1}) to amide I (1665 cm^{-1}) were averaged for the femoral heads and grouped under normal, no treatment (necrotic), BMP, IB, and BMP+IB. The reduced modulus and hardness values from nanoindentation, and CaMean, and CaPeak values from qBEI for each respective group were averaged similarly. All data are presented as mean \pm standard deviation. A one-way ANOVA was used to determine the overall difference among groups. If the difference was significant at $p < 0.05$, a post-hoc Tukey honestly significant difference testing was performed to assess the significance between groups.

5.4 Results

The histological assessment from the femoral heads revealed areas of revascularized tissue in all femoral heads and evidence of bone formation in the BMP and BMP+IB treated groups and excessive bone resorption in the necrotic group. For the normal, BMP, and BMP+IB group, trabeculae were lined with osteoblasts indicating bone formation (Figure 5.1a). However, within the no treatment (necrotic) and ibandronate group areas of revascularized trabecular bone showed a lack of osteoblasts (Figure 5.1a). Additionally, the necrotic group showed trabeculae with osteoclasts and pits caused by osteoclast resorption. Further analysis of the H&E stained slides of the BMP and BMP+IB treated groups revealed new bone formation on the surface of necrotic bone (Figure 5.1b). Necrotic bone was identified based on empty lacunae or pyknotic osteocyte.

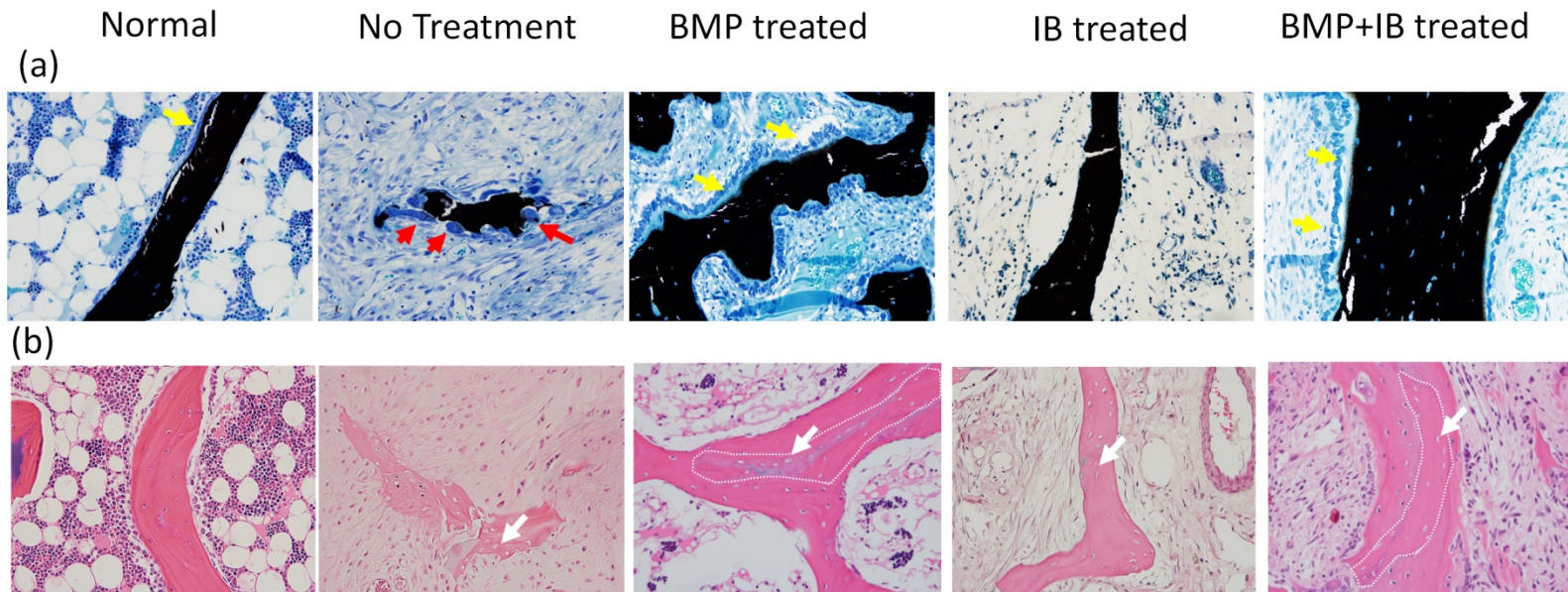


Figure 5.1(a) High magnification von Kossa and McNeal tetrachrome stained photomicrographs captured at 200X magnification of normal, no treatment (necrotic), bone morphogenetic protein-2 (BMP) treated, ibandronate (IB) treated, and BMP+IB treated trabecular bone. Osteoblasts (yellow arrow) line the surface of normal, BMP treated, and BMP+IB treated trabecular bone. Several osteoclasts (red arrow) line the surface of bone in the no treatment image. (b) High magnification hematoxylin and eosin stained photomicrographs captured at 200X of new bone formation surrounding necrotic bone (dotted line) in the BMP and BMP+IB treated trabecular bone. Diminished or absent lacunae staining was present in necrotic bone (white arrow).

Quantitative backscattered electron imaging showed increased mineral content in the no treatment (necrotic) and ibandronate bone groups (Table 5.1). BMDD in the necrotic and ibandronate groups showed a higher calcium weight percent (CaMean) ($p=0.003$, $p=0.007$) and frequency (CaPeak) ($p=0.021$, $p=0.017$) compared to the normal group. Osteoclast pits and fragmented bone were apparent in the revascularized regions of the no treatment (necrotic) femoral head. The contrary was present in the ibandronate group, as bone volume appeared to be maintained (Figure 5.2). Additionally, in similar areas of bone formation and revascularization in the BMP and BMP+IB groups, as indicated by histology, the trabecular bone appeared thicker where new bone formation occurred on the surface of necrotic bone (Figure 5.2).

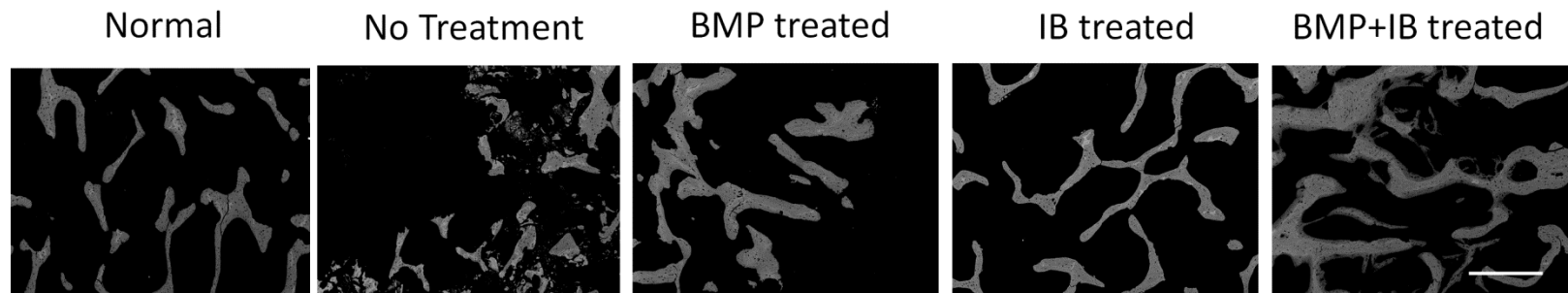


Figure 5.2 Backscattered scanning electron images of normal, no treatment (necrotic), bone morphogenetic protein-2 (BMP) treated, ibandronate (IB) treated, and BMP+IB treated trabecular bone captured at 50X magnification. The BMP and BMP+IB treated trabecular bone appear thicker than the no treatment and IB treated bone. Scale bar = 1 cm.

Raman spectroscopy and nanoindentation were used to measure the compositional and mechanical properties of the trabecular bone. The carbonate content and mineral to matrix ratios were measured by Raman spectroscopy. Specifically, the carbonate to phosphate ratios in the normal group were significantly lower than the no treatment ($p=0.001$), IB ($p=0.001$), and BMP+IB ($p=0.003$) groups, and no significant difference between the BMP and normal group (Figure 5.3a). Differences were seen in the measured carbonate to amide I ratio of the normal group compared to no treatment ($p=0.007$) and IB groups ($p=0.003$), and no significant difference for the BMP and BMP+IB groups compared to normal group (Figure 5.3b). The mineral to matrix ratio in the no treatment group was significantly higher than the normal ($p=0.010$) and the IB group ($p=0.004$), and no significant difference for the BMP and BMP+IB groups compared to normal group (Figure 5.3c). Mechanical properties measured by nanoindentation showed only significant differences of increased moduli and hardness in the trabecular bone of the ibandronate group compared to normal ($p<0.05$) (Figure 5.4). Additionally, increased significantly increased hardness was found in the IB group compared to all other treated groups (BMP and BMP+IB) ($p\leq 0.02$).

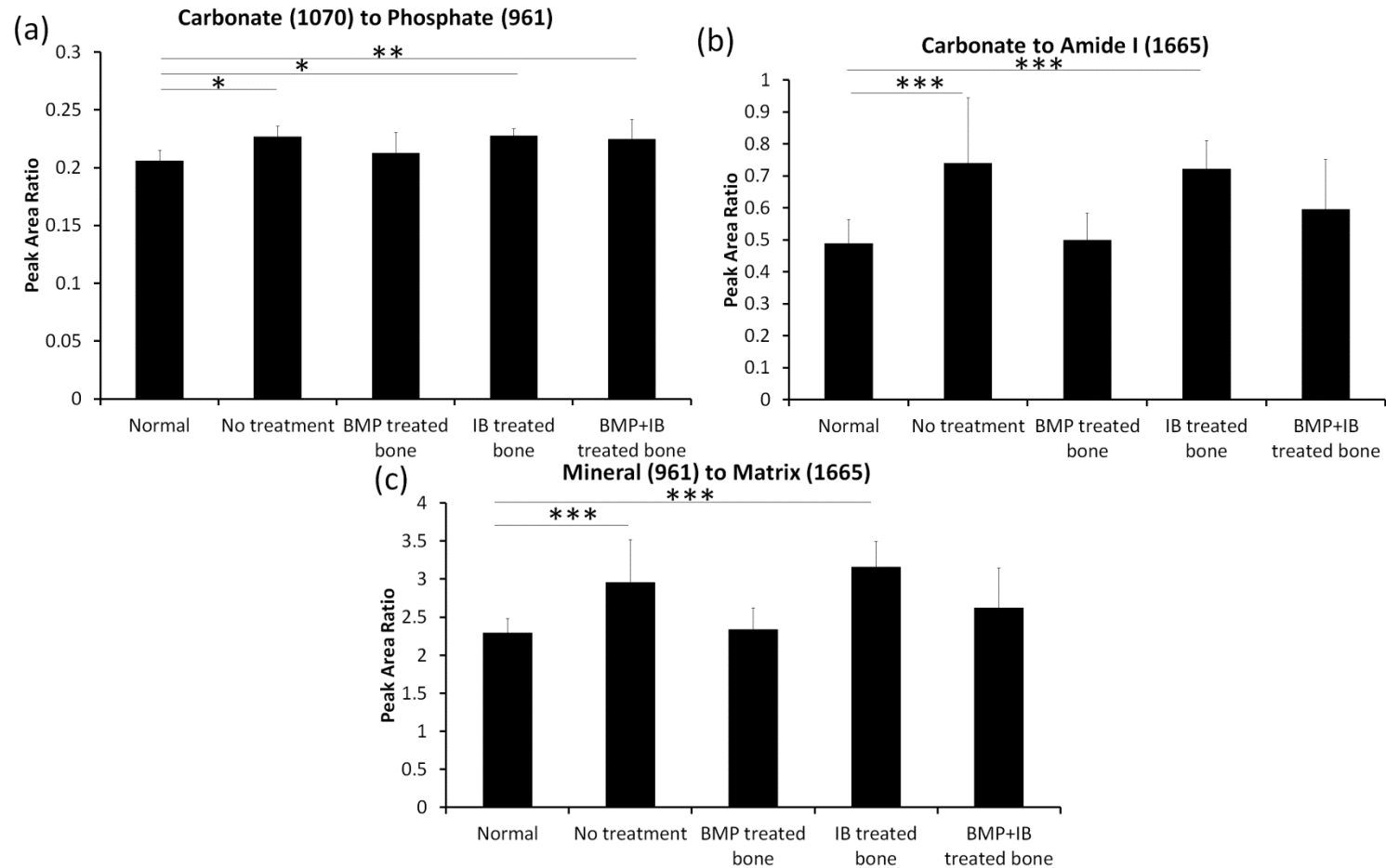


Figure 5.3(a) Carbonate to phosphate peak area ratio of normal trabecular bone was significantly lower than no treatment (necrotic) ($p=0.001$)*, IB (ibandronate) treated ($p=0.001$)*, and BMP+IB (bone morphogenetic protein + IB) treated bone ($p=0.003$)**. (b) Carbonate to Amide I and (c) Mineral to Matrix peak area ratio of the normal group was significantly lower than no treatment ($p\leq 0.01$)*** and IB treated bone ($p\leq 0.004$)***. ($n=5$ per group)

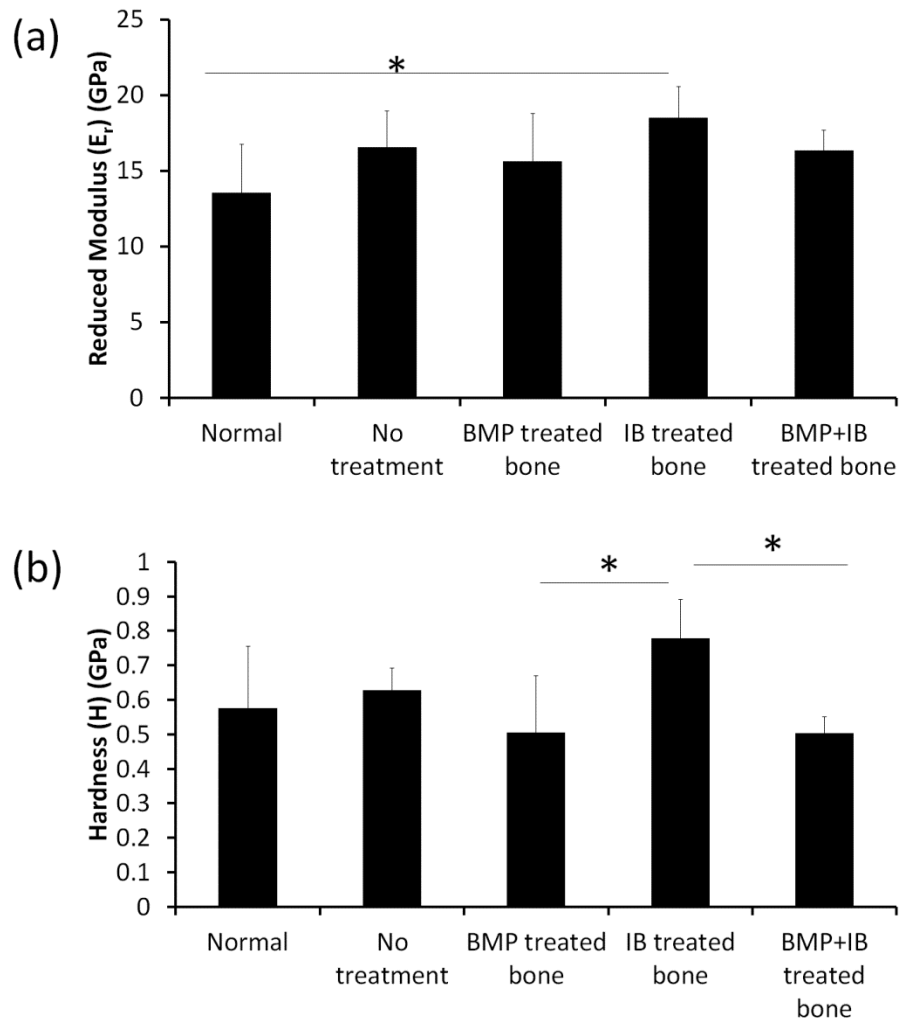


Figure 5.4. Bar graphs of the (a) average reduced modulus and (b) hardness of the normal, no treatment (necrotic), bone morphogenetic protein-2 (BMP) treated, ibandronate (IB) treated, and BMP+IB treated trabecular bone. The reduced modulus of the IB treated bone was significantly higher than normal healthy trabecular bone (* $p=0.024$), and the IB treated group was significantly higher than the BMP and BMP+IB treated groups ($p \leq 0.02$). ($n=5$ per group)

Table 5.1 The mean \pm standard deviation of weight percent calcium and nanomechanical properties of the treatment groups.

	Normal	No Treatment	BMP treated	IB treated	BMP+IB treated
CaMean (wt%Ca)	23.1 \pm 0.9	26.1 \pm 0.7*	22.8 \pm 1.9	26.0 \pm 0.5**	23.3 \pm 1.1
CaPeak (wt%Ca)	23.5 \pm 1.0	26.2 \pm 1.1***	23.0 \pm 2.2	26.3 \pm 0.3****	23.9 \pm 0.9
Reduced Modulus (GPa)	13.5 \pm 3.2	16.5 \pm 2.4	15.6 \pm 3.2	18.5 \pm 2.1#	16.3 \pm 1.3
Hardness (GPa)	0.574 \pm 0.181	0.626 \pm 0.065	0.505 \pm 0.165	0.778 \pm 0.113##	0.503 \pm 0.047

*No treatment vs Normal (p=0.003), BMP (p=0.001), and BMP+IB (p=0.007)

**IB vs Normal (p=0.007), BMP (p=0.003), and BMP+IB (p=0.014)

***No Treatment vs Normal (p=0.021), BMP (p=0.006)

****IB vs Normal (p=0.017), BMP (p=0.005), and BMP+IB (p=0.047)

#Normal vs IB treated (p=0.024)

##IB treated vs. BMP treated (p=0.020) and BMP+IB treated (p=0.019)

5.5 Discussion

Ischemic osteonecrosis of the femoral head has been shown to lead to extensive cell death, increased mineral content, and microcracks [16,29]. It is through normal bone remodeling where old and damaged bone is remodeled and repaired with the appropriate balance of bone formation from osteoblasts and bone resorption from osteoclasts. Without bone remodeling, damage from cracks has been proposed to continue to propagate and lead to fracture. In addition, imbalanced repair from increased osteoclastic resorption and decreased bone formation contributes to the collapse of the femoral head [5].

While treatment with BMP has been previously shown to induce new bone formation post ischemia [24,25], it appears a lack of new bone formation and remodeling, can compound increased mineral content in the no treatment (necrotic) and ibandronate groups compared to normal, BMP, and BMP+IB groups. This was further supported by an increased mineral to matrix ratio in the necrotic and ibandronate groups measured by Raman spectroscopy. Additionally, increased carbonate content was also measured in the necrotic and IB groups. Taken together, treatment post ischemic osteonecrosis produces significantly different material properties of bone.

Bisphosphonates have been used previously to decrease bone resorption and maintain bone volume in osteoporotic and postmenopausal women [215-217], in Paget's disease [218], and in animal models of osteonecrosis to prevent excessive resorption of necrotic bone [21,22,219]. In the piglet model of osteonecrosis, ibandronate, a type of bisphosphonate, was used to decrease the amount of osteoclast activity in the femoral head post ischemia. While there was a decrease in the amount of bone resorption, there was minimal bone formation as defined by the lack of osteoblasts. This has previously been described quantitatively by a significant decrease in the osteoblast surface in the ibandronate treated group compared to a normal group [24]. On other hand, when BMP was used in both BMP and BMP+IB groups,

there was a presence of osteoblasts within the treated epiphysis. In fact, increased bone formation has previously been demonstrated post ischemia in BMP groups when compared to a non-treated necrotic group [25]. The use of bmp-2 can influence bone remodeling by stimulating osteoclast [220] and osteoblast [203] differentiation. While it appears that the use of ibandronate alone maintains bone volume, there is a lack of bone remodeling and formation in the ibandronate treated epiphysis that appears to affect the material properties. Decreased remodeling has been shown previously to increase mineralization of bisphosphonate treated bone of osteoporotic patients [221,222]. Similarly, the mineral content is increased in bisphosphonate treated necrotic bone in this study. While increased mineral content in necrotic bone is associated with bone necrosis, it may be compounded with bisphosphonate treatment.

The mineral content of the necrotic bone in the femoral head has been measured previously by quantitative backscattered imaging, where increased mineral content was present when compared with normal bone formation [16]. The same here is true in this study where increased mineral content is seen in the necrotic group. Furthermore, even after treatment with ibandronate, the mineral content in the IB group was also significantly higher. However, when comparing the BMP and BMP+IB treated groups, the mineral content was significantly lower than the IB and necrotic group and comparable to the normal group. The key difference between the IB and necrotic groups and the BMP and BMP+IB treated groups is the bone remodeling from the bone formation and resorption. In fact, the bone formation by osteoblasts and the resorption by osteoclasts have previously been identified in the BMP and BMP+IB treatment groups [25]. This suggests a lack of balanced remodeling contributing to an increase in mineral content in necrotic and ibandronate treated bone.

The mineral composition of the bone was further analyzed by Raman spectroscopy which revealed increased carbonate content in the necrotic group and IB group, coinciding with the lack of new bone formation and increased mineral content. Necrotic bone that is maintained and unchanged without any remodeling is older the normal bone that continually modeled and

remodeled in the developing femoral head. In fact, increased carbonate content has been linked to aged bone [143,196,198]. Furthermore, the mineral to matrix ratio was also decreased when compared to the necrotic and IB groups. In fact, increased mineral-to-matrix ratios and crystallinity have been attributed to fracture risk [223,224]. For carbonate content, increased carbonate-to-amide I and carbonate-to-phosphate ratios have been attributed to fracture risk in osteoporotic patients [225]. New bone formation after ischemia improves the bone compositional parameters that have been linked to fracture risk.

The increased mineral content associated with the increased nanomechanical properties measured by nanoindentation in the necrotic and IB groups. Oral ibandronate use has been linked to increased hardness in osteoporotic patients [226] and stiffer trabecular bone after bisphosphonate use in severely suppressed bone turnover patients [227]. However, the bone formation in the BMP group and BMP+IB group showed similar nanomechanical properties to normal bone. Few studies have investigated the nanomechanical properties of bmp treated bone [228,229]. One study used an in vitro model of cultured mineralized tissue with BMP-2 and found lower hardness and elastic moduli when compared to calvaria bone [228] while another study used PLLA nanofibers with BMP-2 and found similar hardness and elastic moduli between newly regenerated bone and the host bone of the calvaria [229]. Similar mechanical properties were also found with regenerate bone developed within a bone defect by implanted with genetically modified mesenchymal stem cells that overexpressed BMP-2 [230]. Our study involved new bone formation without the aid of other biomaterials and within the femoral head as opposed to the calvaria. Nonetheless, we believe the new bone formation aided with bmp-2 in the BMP and BMP+IB treatment groups provided similar nanomechanical properties to normal healthy bone. Furthermore, we believe the interstitial, older, necrotic bone provides added nanomechanical properties of increased moduli and hardness.

This study does have some limitations. While qBEI measurements looked at a much larger area of tissue volume ($\geq 50 \text{ mm}^2$) within the mid-epiphysis, Raman and nanoindentation

measurements were captured at smaller scales ($<10000 \mu\text{m}^2$). Nonetheless, measurements were performed in revascularized regions of the epiphysis where bone healing and repair were expected, and the Raman and nanomechanical measurements were indicative of pooled measurements across a trabeculae. The measurements were performed in a similar location for all samples avoiding measurements in the embedding material. Assessment of the material properties only occurred at one time point, later time points may be more informative to assess bone formation that may be delayed in the IB treated group. We chose to perform measurements at a time point; where there was moderate to severe deformity due to extensive resorption in the no treatment group. In addition, macro scale measurements of mechanical properties may provide an overall look at the bone's response to loading and fracture resistance in the femoral head.

In conclusion, treatment of the ischemic osteonecrosis aims to prevent deformity, but what remains unclear is the best approach. This study investigated the compositional and nanomechanical properties of bone treated with bone anabolic and anti-resorptive agents to compare to normal bone without treatment. The findings show that anabolic and combined anabolic and anti-resorptive agents better normalize material properties of bone than sole treatment by an anti-resorptive agent. Mineral content, mineral to matrix, and carbonate to phosphate ratios were found to be increased in necrotic and IB treated bone. Treatment of the femoral head with bone anabolic and anti-resorptive agents post ischemia produces significantly different material properties of bone. We postulate it is the older/necrotic bone that is hypermineralized post ischemia than can contribute to increased fracture risks, while new bone formation aided by bmp-2 can contribute support to the older/necrotic bone and restore compositional equivalencies to normal bone formation. We also postulate new bone formation around the necrotic bone can provide added mechanical strength to help prevent fracture and collapse during juvenile femoral head osteonecrosis.

Chapter 6

Summary and Conclusion

The purpose of this study was to determine the material changes in bone through significant pathological events in ischemic osteonecrosis of the femoral head. The events include fracture, extensive resorption, and collapse of the femoral head. Development of a subchondral fracture is one of the earliest signs of structural failure of the immature femoral head following ischemic osteonecrosis and this eventually leads to a flattening deformity of the femoral head. The macro scale mechanical properties of the infarcted femoral head decreases even before a repair response consisting of bone resorption occurs [13,14]. The reason for the decreases in the mechanical properties was unknown, which prompted an investigation of the material and mechanical changes in the femoral head preceding possible structural failure. We focused on the mechanical and material properties because they are important contributors to the overall mechanical structure. Within the subchondral region, we found extensive cell death and an absence of osteoblasts in the ischemic side compared to the normal control. Microcrack density in the ischemic side was significantly higher compared to the normal side in the subchondral region. The weighted mean of the weight percent distribution of calcium (CaMean) also was significantly higher in the ischemic subchondral region. Furthermore, the nanoindentation modulus within localized areas of subchondral bone was significantly increased in the ischemic side compared to the normal control. The increased mineral content measured by quantitative backscattered imaging was of particular interest, as we were curious as to the possible changes in the mineral chemistry that would be best analyzed by spectroscopy techniques.

The most common analogous mineral component to bone is hydroxyapatite, which can be present in many forms due to ionic substitution thus altering chemical composition. Unfortunately, very little is known about the chemical changes to bone apatite following ischemic osteonecrosis of the femoral head. We assessed the macroscopic and local

phosphate composition of necrotic bone during the repair stage to isolate differences between areas of increased osteoclast resorption and normal bone formation. X-ray absorbance near edge structure and Raman spectroscopy obtained from necrotic bone during the repair stage and normal bone showed increased carbonate to phosphate content in the necrotic bone. The exact mechanism of carbonate substitution in necrotic bone is unknown, but we hypothesize that as cells die through apoptosis the apoptotic bodies incorporate within the bone matrix and are nucleating centers for increased carbonate apatite formation. We believe the changes in the apatite composition due to carbonate substitution may play a role in the increased resorption of necrotic bone due to its increase in solubility. Indeed, a better understanding of the apatite composition of necrotic bone could shed light on osteoclast activity and potentially improve therapeutic treatments that target excessive resorption of bone. This prompted our interest in the material changes of bone following treatment to restore the imbalance caused by excessive bone resorption.

Treatment aims to not only retain the sphericity of the femoral head, but to promote bone healing to help prevent collapse. We determined the effects of an anabolic (bone morphogenetic protein-2, BMP-2) and an anti-resorptive agent (ibandronate, IB), a well-known bisphosphonate, on the material properties of bone after ischemic osteonecrosis of the femoral head. Quantitative backscattered electron imaging, Raman spectroscopy, and nanoindentation were used to measure the material changes in mineral content, composition, and mechanical properties. New bone in the BMP and BMP+IB groups was identified by McNeal and H&E sections revealing new bone surrounding old necrotic bone, while the ibandronate group showed no osteoblast and the necrotic group showed osteoclastic resorption of necrotic bone. CaMean and CaPeak measured by qBEI was significantly increased in the necrotic and IB groups compared to normal. Carbonate content measured relative to phosphate and matrix bands showed significantly increased content in the necrotic and IB groups compared to normal. Indeed, carbonate content has been linked to aged and fractured bone; however,

evidence of collapse and a flattening deformity in the post ischemic femoral head is only seen in the no treatment (necrotic) group [17]. It appears the IB treatment used to prevent bone resorption may mechanically protect the structure of the head from collapse. But still, further research to assess microdamage may provide additional information about the material state in conjunction to macroscale mechanical measurements of IB treated bone. Indeed, the nanoindentation modulus within the IB treated trabecular bone was significantly increased compared to the normal trabecular bone. The increased mineral content and nanomechanical properties show intrinsic changes IB treated bone.

Taken together, the nanoindentation properties of the trabecular bone is increased in the early stage of ischemic osteonecrosis of the immature femoral head and makes it more susceptible to microcrack formation, while balanced repair aided by anabolic and anti-resorptive treatments help restore the material properties of bone to normal bone formation with comparable compositional properties (Figure 6.1). Further studies will need to investigate the macroscale mechanical properties after treatment. However, we believe new bone formation around the necrotic bone can provide added mechanical strength to help prevent fracture and collapse of the bone during juvenile femoral head osteonecrosis.

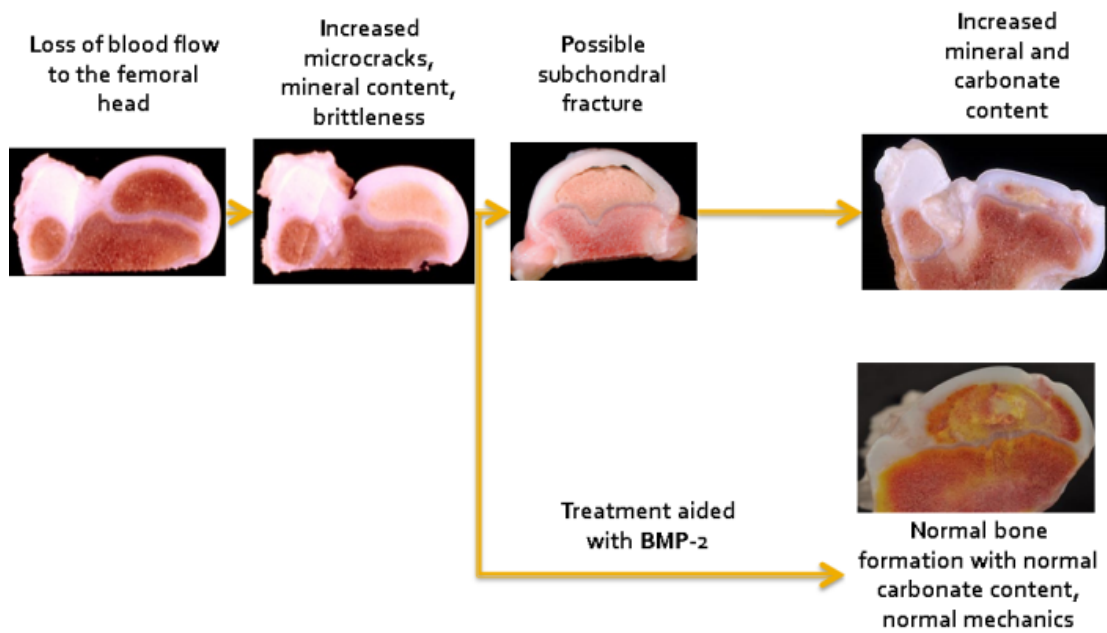


Figure 6.1 Overview of related material changes of necrotic bone with and without treatment aided by BMP-2.

References

- [1] Kim HK. Pathophysiology and new strategies for the treatment of legg-calvé-perthes disease. *The Journal of Bone & Joint Surgery* 2012;94:659-69.
- [2] Cristofolini L, Taddei F, Baleani M, Baruffaldi F, Stea S, Viceconti M. Multiscale investigation of the functional properties of the human femur. *Philos. Trans. A. Math. Phys. Eng. Sci.* 2008;366:3319-41.
- [3] Wegst UG, Bai H, Saiz E, Tomsia AP, Ritchie RO. Bioinspired structural materials. *Nature materials* 2014;.
- [4] Fazzalari NL, Forwood MR, Smith K, Manthey BA, Herreen P. Assessment of cancellous bone quality in severe osteoarthritis: Bone mineral density, mechanics, and microdamage. *Bone* 1998;22:381-8.
- [5] Kim HK, Su PH. Development of flattening and apparent fragmentation following ischemic necrosis of the capital femoral epiphysis in a piglet model. *J. Bone Joint Surg. Am.* 2002;84-A:1329-34.
- [6] Oliver WC, Pharr GM. An improved technique for determining hardness and elastic modulus using load and displacement sensing indentation experiments. *J. Mater. Res.* 1992;7:1564-83.
- [7] Roschger P, Fratzl P, Eschberger J, Klaushofer K. Validation of quantitative backscattered electron imaging for the measurement of mineral density distribution in human bone biopsies. *Bone* 1998;23:319-26.
- [8] Bare SR. XANES measurements and interpretation. University of Chicago 2005;.
- [9] Oftadeh R, Perez-Viloria M, Villa-Camacho JC, Vaziri A, Nazarian A. Biomechanics and mechanobiology of trabecular bone: A review. *J. Biomech. Eng.* 2015;137:010802.
- [10] Derkx P, Nigg A, Bosman F, Birkenhäger-Frenkel D, Houtsmuller A, Pols H et al. Immunolocalization and quantification of noncollagenous bone matrix proteins in

methylmethacrylate-embedded adult human bone in combination with histomorphometry. *Bone* 1998;22:367-73.

[11] Mandair GS, Morris MD. Contributions of raman spectroscopy to the understanding of bone strength. *BoneKEY reports* 2015;4:.

[12] Rho JY, Kuhn-Spearing L, Zioupos P. Mechanical properties and the hierarchical structure of bone. *Med. Eng. Phys.* 1998;20:92-102.

[13] Pringle D, Koob TJ, Kim HK. Indentation properties of growing femoral head following ischemic necrosis. *J. Orthop. Res.* 2004;22:122-30.

[14] Koob TJ, Pringle D, Gedbaw E, Meredith J, Berrios R, Kim HK. Biomechanical properties of bone and cartilage in growing femoral head following ischemic osteonecrosis. *J. Orthop. Res.* 2007;25:750-7.

[15] Park SS, Kim HK. Subchondral fracture after ischemic osteonecrosis of the immature femoral head in piglet model. *J. Pediatr. Orthop. B* 2011;20:227-31.

[16] Hofstaetter JG, Roschger P, Klaushofer K, Kim HK. Increased matrix mineralization in the immature femoral head following ischemic osteonecrosis. *Bone* 2010;46:379-85.

[17] Kim HK, Randall TS, Bian H, Jenkins J, Garces A, Bauss F. Ibandronate for prevention of femoral head deformity after ischemic necrosis of the capital femoral epiphysis in immature pigs. *J. Bone Joint Surg. Am.* 2005;87:550-7.

[18] Capuccini C, Torricelli P, Sima F, Boanini E, Ristoscu C, Bracci B et al. Strontium-substituted hydroxyapatite coatings synthesized by pulsed-laser deposition: In vitro osteoblast and osteoclast response. *Acta Biomaterialia* 2008;4:1885-93.

[19] Spence G, Patel N, Brooks R, Bonfield W, Rushton N. Osteoclastogenesis on hydroxyapatite ceramics: The effect of carbonate substitution. *Journal of Biomedical Materials Research Part A* 2010;92:1292-300.

- [20] Shepherd DV, Kauppinen K, Brooks RA, Best SM. An in vitro study into the effect of zinc substituted hydroxyapatite on osteoclast number and activity. *Journal of Biomedical Materials Research Part A* 2014;.
- [21] Little DG, Peat RA, Mcevoy A, Williams PR, Smith EJ, Baldock PA. Zoledronic acid treatment results in retention of femoral head structure after traumatic osteonecrosis in young wistar rats. *Journal of Bone and Mineral Research* 2003;18:2016-22.
- [22] Little DG, McDonald M, Sharpe IT, Peat R, Williams P, McEvoy T. Zoledronic acid improves femoral head sphericity in a rat model of perthes disease. *Journal of orthopaedic research* 2005;23:862-8.
- [23] Aya-ay J, Athavale S, Morgan-Bagley S, Bian H, Bauss F, Kim HK. Retention, distribution, and effects of intraosseously administered ibandronate in the infarcted femoral head. *Journal of Bone and Mineral Research* 2007;22:93-100.
- [24] Vandermeer JS, Kamiya N, Aya-ay J, Garces A, Browne R, Kim HK. Local administration of ibandronate and bone morphogenetic protein-2 after ischemic osteonecrosis of the immature femoral HeadA combined therapy that stimulates bone formation and decreases femoral head deformity. *The Journal of Bone & Joint Surgery* 2011;93:905-13.
- [25] Kim HK, Aruwajoye O, Du J, Kamiya N. Local administration of bone morphogenetic protein-2 and bisphosphonate during non-weight-bearing treatment of ischemic osteonecrosis of the femoral head: An experimental investigation in immature pigs. *J. Bone Joint Surg. Am.* 2014;96:1515-24.
- [26] Monier-Faugere M, Geng Z, Paschalis EP, Qi Q, Arnala I, Bauss F et al. Intermittent and continuous administration of the bisphosphonate ibandronate in ovariectomized beagle dogs: Effects on bone morphometry and mineral properties. *Journal of Bone and Mineral Research* 1999;14:1768-78.

- [27] Donnelly E, Meredith DS, Nguyen JT, Gladnick BP, Rebolledo BJ, Shaffer AD et al. Reduced cortical bone compositional heterogeneity with bisphosphonate treatment in postmenopausal women with intertrochanteric and subtrochanteric fractures. *Journal of Bone and Mineral Research* 2012;27:672-8.
- [28] Misof BM, Patsch JM, Roschger P, Muschitz C, Gamsjaeger S, Paschalis EP et al. Intravenous treatment with ibandronate normalizes bone matrix mineralization and reduces cortical porosity after two years in male osteoporosis: A paired biopsy study. *Journal of Bone and Mineral Research* 2014;29:440-9.
- [29] Aruwajoye OO, Patel MK, Allen MR, Burr DB, Aswath PB, Kim HKW. Microcrack density and nanomechanical properties in the subchondral region of the immature piglet femoral head following ischemic osteonecrosis. *Bone* 2013;52:632-9.
- [30] Caffey J. The early roentgenographic changes in essential coxa plana: Their significance in pathogenesis. *Am. J. Roentgenol. Radium Ther. Nucl. Med.* 1968;103:620-34.
- [31] Aruwajoye OO, Kim HKW, Aswath PB. Bone apatite composition of necrotic trabecular bone in the femoral head of immature piglets. *Calcif. Tissue Int.* 2015;96:324-34.
- [32] Bergmann G, Graichen F, Rohlmann A. Hip joint loading during walking and running, measured in two patients. *J. Biomech.* 1993;26:969-90.
- [33] Bergmann G, Deuretzbacher G, Heller M, Graichen F, Rohlmann A, Strauss J et al. Hip contact forces and gait patterns from routine activities. *J. Biomech.* 2001;34:859-71.
- [34] Lee MC, Ebersson CP. Growth and development of the child's hip. *Orthop. Clin. North Am.* 2006;37:119-32.
- [35] Chung SM. The arterial supply of the developing proximal end of the human femur. *J. Bone Joint Surg. Am.* 1976;58:961-70.

- [36] Johnson EO, Soultanis K, Soucacos PN. Vascular anatomy and microcirculation of skeletal zones vulnerable to osteonecrosis: Vascularization of the femoral head. *Orthop. Clin. North Am.* 2004;35:285-91.
- [37] H.V. Crock, M.C. Crock, *The blood supply of the lower limb bones in man:(descriptive and applied)*, Churchill Livingstone, 1967.
- [38] Waitches G, Zawin JK, Poznanski AK. Sequence and rate of bone marrow conversion in the femora of children as seen on MR imaging: Are accepted standards accurate? *AJR Am. J. Roentgenol.* 1994;162:1399-406.
- [39] Taccone A, Oddone M, Dell'Acqua A, Occhi M, Ciccone M. MRI "road-map" of normal age-related bone marrow. *Pediatr. Radiol.* 1995;25:596-606.
- [40] Laor T, Jaramillo D. MR imaging insights into skeletal maturation: What is normal? 1. *Radiology* 2009;250:28-38.
- [41] Kuznetsov SA, Mankani MH, Gronthos S, Satomura K, Bianco P, Robey PG. Circulating skeletal stem cells. *J. Cell Biol.* 2001;153:1133-40.
- [42] Eghbali-Fatourehchi GZ, Lamsam J, Fraser D, Nagel D, Riggs BL, Khosla S. Circulating osteoblast-lineage cells in humans. *N. Engl. J. Med.* 2005;352:1959-66.
- [43] Otsuru S, Tamai K, Yamazaki T, Yoshikawa H, Kaneda Y. Bone marrow-derived osteoblast progenitor cells in circulating blood contribute to ectopic bone formation in mice. *Biochem. Biophys. Res. Commun.* 2007;354:453-8.
- [44] Fujikawa Y, Quinn JM, Sabokbar A, McGee JO, Athanasou NA. The human osteoclast precursor circulates in the monocyte fraction. *Endocrinology* 1996;137:4058-60.
- [45] Matayoshi A, Brown C, DiPersio JF, Haug J, Abu-Amer Y, Liapis H et al. Human blood-mobilized hematopoietic precursors differentiate into osteoclasts in the absence of stromal cells. *Proc. Natl. Acad. Sci. U. S. A.* 1996;93:10785-90.

- [46] Shalhoub V, Elliott G, Chiu L, Manoukian R, Kelley M, Hawkins N et al. Characterization of osteoclast precursors in human blood. *Br. J. Haematol.* 2000;111:501-12.
- [47] Blumer MJ, Longato S, Fritsch H. Structure, formation and role of cartilage canals in the developing bone. *Annals of Anatomy-Anatomischer Anzeiger* 2008;190:305-15.
- [48] Blumer MJ, Longato S, Richter E, Pérez MT, Konakci KZ, Fritsch H. The role of cartilage canals in endochondral and perichondral bone formation: Are there similarities between these two processes? *J. Anat.* 2005;206:359-72.
- [49] Burkus JK, Ganey TM, Ogden JA. Development of the cartilage canals and the secondary center of ossification in the distal chondroepiphysis of the prenatal human femur. *Yale J. Biol. Med.* 1993;66:193-202.
- [50] Rho JY, Ashman RB, Turner CH. Young's modulus of trabecular and cortical bone material: Ultrasonic and microtensile measurements. *J. Biomech.* 1993;26:111-9.
- [51] Bigi A, Cojazzi G, Panzavolta S, Ripamonti A, Roveri N, Romanello M et al. Chemical and structural characterization of the mineral phase from cortical and trabecular bone. *J. Inorg. Biochem.* 1997;68:45-51.
- [52] Goodyear SR, Gibson IR, Skakle JM, Wells RP, Aspden RM. A comparison of cortical and trabecular bone from C57 black 6 mice using raman spectroscopy. *Bone* 2009;44:899-907.
- [53] Currey JD. Effects of differences in mineralization on the mechanical properties of bone. *Philos. Trans. R. Soc. Lond. B. Biol. Sci.* 1984;304:509-18.
- [54] Currey JD. The effect of porosity and mineral content on the young's modulus of elasticity of compact bone. *J. Biomech.* 1988;21:131-9.

- [55] Uchiyama T, Tanizawa T, Muramatsu H, Endo N, Takahashi H, Hara T. Three-dimensional microstructural analysis of human trabecular bone in relation to its mechanical properties. *Bone* 1999;25:487-91.
- [56] Kleerekoper M, Villanueva A, Stanciu J, Rao DS, Parfitt A. The role of three-dimensional trabecular microstructure in the pathogenesis of vertebral compression fractures. *Calcif. Tissue Int.* 1985;37:594-7.
- [57] Recker RR. Low bone mass may not be the only cause of skeletal fragility in osteoporosis. *Proc. Soc. Exp. Biol. Med.* 1989;191:272-4.
- [58] Bonucci E. Bone mineralization. *Front. Biosci. (Landmark Ed)* 2012;17:100-28.
- [59] Hodge AJ, Petruska JA. Recent studies with the electron microscope on ordered aggregates of the tropocollagen molecule. *Aspects of protein structure* 1963;289-300.
- [60] White SW, Hulmes DJ, Miller A, Timmins PA. Collagen-mineral axial relationship in calcified turkey leg tendon by X-ray and neutron diffraction. *Nature* 1977;266:421-5.
- [61] Landis WJ, Hodgins KJ, Arena J, Song MJ, McEwen BF. Structural relations between collagen and mineral in bone as determined by high voltage electron microscopic tomography. *Microsc. Res. Tech.* 1996;33:192-202.
- [62] Glimcher MJ. Mechanism of calcification: Role of collagen fibrils and collagen-phosphoprotein complexes in vitro and in vivo. *Anat. Rec.* 1989;224:139-53.
- [63] Glimcher MJ. Bone: Nature of the calcium phosphate crystals and cellular, structural, and physical chemical mechanisms in their formation. *Reviews in Mineralogy and Geochemistry* 2006;64:223-82.
- [64] Hohling HJ, Arnold S, Plate U, Stratmann U, Wiesmann HP. Analysis of a general principle of crystal nucleation, formation in the different hard tissues. *Adv. Dent. Res.* 1997;11:462-6.

- [65] Fujisawa R, Nodasaka Y, Kuboki Y. Further characterization of interaction between bone sialoprotein (BSP) and collagen. *Calcif. Tissue Int.* 1995;56:140-4.
- [66] Wang Y, Azais T, Robin M, Vallée A, Catania C, Legriel P et al. The predominant role of collagen in the nucleation, growth, structure and orientation of bone apatite. *Nature materials* 2012;11:724-33.
- [67] Boskey A, Maresca M, Ullrich W, Doty S, Butler W, Prince C. Osteopontin-hydroxyapatite interactions in vitro: Inhibition of hydroxyapatite formation and growth in a gelatin-gel. *Bone Miner.* 1993;22:147-59.
- [68] Sodek J, Ganss B, McKee MD. Osteopontin. *Crit. Rev. Oral Biol. Med.* 2000;11:279-303.
- [69] Boskey A, Spevak L, Paschalis E, Doty S, McKee M. Osteopontin deficiency increases mineral content and mineral crystallinity in mouse bone. *Calcif. Tissue Int.* 2002;71:145-54.
- [70] Romberg RW, Werness PG, Riggs BL, Mann KG. Inhibition of hydroxyapatite-crystal growth by bone-specific and other calcium-binding proteins. *Biochemistry (N. Y.)* 1986;25:1176-80.
- [71] Doi Y, Okuda R, Takezawa Y, Shibata S, Moriwaki Y, Wakamatsu N et al. Osteonectin inhibiting de novo formation of apatite in the presence of collagen. *Calcif. Tissue Int.* 1989;44:200-8.
- [72] Bianco P, Riminucci M, Silvestrini G, Bonucci E, Termine JD, Fisher LW et al. Localization of bone sialoprotein (BSP) to golgi and post-golgi secretory structures in osteoblasts and to discrete sites in early bone matrix. *J. Histochem. Cytochem.* 1993;41:193-203.
- [73] Ganss B, Kim RH, Sodek J. Bone sialoprotein. *Crit. Rev. Oral Biol. Med.* 1999;10:79-98.

- [74] Qin C, Baba O, Butler WT. Post-translational modifications of sibling proteins and their roles in osteogenesis and dentinogenesis. *Crit. Rev. Oral Biol. Med.* 2004;15:126-36.
- [75] Baht GS, Hunter GK, Goldberg HA. Bone sialoprotein–collagen interaction promotes hydroxyapatite nucleation. *Matrix Biology* 2008;27:600-8.
- [76] Hauschka PV, Lian JB, Cole D, Gundberg CM. Osteocalcin and matrix gla protein: Vitamin K-dependent proteins in bone. *Physiol. Rev.* 1989;69:990-1047.
- [77] Ducy P, Desbois C, Boyce B, Pinero G, Story B, Dunstan C et al. Increased bone formation in osteocalcin-deficient mice. 1996;.
- [78] Boskey A, Gadaleta S, Gundberg C, Doty S, Ducy P, Karsenty G. Fourier transform infrared microspectroscopic analysis of bones of osteocalcin-deficient mice provides insight into the function of osteocalcin. *Bone* 1998;23:187-96.
- [79] Mochida Y, Duarte WR, Tanzawa H, Paschalis EP, Yamauchi M. Decorin modulates matrix mineralization in vitro. *Biochem. Biophys. Res. Commun.* 2003;305:6-9.
- [80] Mochida Y, Parisuthiman D, Pornprasertsuk-Damrongsri S, Atsawasuan P, Sricholpech M, Boskey AL et al. Decorin modulates collagen matrix assembly and mineralization. *Matrix Biology* 2009;28:44-52.
- [81] Corsi A, Xu T, Chen X, Boyde A, Liang J, Mankani M et al. Phenotypic effects of biglycan deficiency are linked to collagen fibril abnormalities, are synergized by decorin deficiency, and mimic Ehlers-Danlos-Like changes in bone and other connective tissues. *Journal of Bone and Mineral Research* 2002;17:1180-9.
- [82] Urist MR. Bone: Formation by autoinduction. *Science* 1965;150:893-9.
- [83] Yu YY, Lieu S, Lu C, Colnot C. Bone morphogenetic protein 2 stimulates endochondral ossification by regulating periosteal cell fate during bone repair. *Bone* 2010;47:65-73.

- [84] Uludag H, D'Augusta D, Golden J, Li J, Timony G, Riedel R et al. Implantation of recombinant human bone morphogenetic proteins with biomaterial carriers: A correlation between protein pharmacokinetics and osteoinduction in the rat ectopic model. *J. Biomed. Mater. Res.* 2000;50:227-38.
- [85] Yuan H, De Bruijn J, Zhang X, Van Blitterswijk C, De Groot K. Use of an osteoinductive biomaterial as a bone morphogenetic protein carrier. *J. Mater. Sci. Mater. Med.* 2001;12:761-6.
- [86] Kokubo S, Mochizuki M, Fukushima S, Ito T, Nozaki K, Iwai T et al. Long-term stability of bone tissues induced by an osteoinductive biomaterial, recombinant human bone morphogenetic protein-2 and a biodegradable carrier. *Biomaterials* 2004;25:1795-803.
- [87] Kokubo S, Nozaki K, Fukushima S, Takahashi K, Miyata K, Fujimoto R et al. Recombinant human bone morphogenetic protein-2 as an osteoinductive biomaterial and a biodegradable carrier in a rabbit ulnar defect model. *J. Bioact. Compatible Polym.* 2008;23:348-66.
- [88] Deckers MM, van Bezooijen RL, van der Horst G, Hoogendam J, van der Bent C, Papapoulos SE et al. Bone morphogenetic proteins stimulate angiogenesis through osteoblast-derived vascular endothelial growth factor A. *Endocrinology* 2002;143:1545-53.
- [89] Boonrungsiman S, Gentleman E, Carzaniga R, Evans ND, McComb DW, Porter AE et al. The role of intracellular calcium phosphate in osteoblast-mediated bone apatite formation. *Proc. Natl. Acad. Sci. U. S. A.* 2012;109:14170-5.
- [90] Bonewald LF. The amazing osteocyte. *Journal of Bone and Mineral Research* 2011;26:229-38.

- [91] Cowin SC, Moss-Salentijn L, Moss ML. Candidates for the mechanosensory system in bone. *J. Biomech. Eng.* 1991;113:191-7.
- [92] Weinbaum S, Cowin S, Zeng Y. A model for the excitation of osteocytes by mechanical loading-induced bone fluid shear stresses. *J. Biomech.* 1994;27:339-60.
- [93] Burger EH, Klein-Nulend J. Mechanotransduction in bone--role of the lacuno-canalicular network. *FASEB J.* 1999;13 Suppl:S101-12.
- [94] Verborgt O, Gibson GJ, Schaffler MB. Loss of osteocyte integrity in association with microdamage and bone remodeling after fatigue in vivo. *Journal of Bone and Mineral Research* 2000;15:60-7.
- [95] Taylor AF, Saunders MM, Shingle DL, Cimbala JM, Zhou Z, Donahue HJ. Mechanically stimulated osteocytes regulate osteoblastic activity via gap junctions. *Am. J. Physiol. Cell. Physiol.* 2007;292:C545-52.
- [96] Nakashima T, Hayashi M, Fukunaga T, Kurata K, Oh-hora M, Feng JQ et al. Evidence for osteocyte regulation of bone homeostasis through RANKL expression. *Nat. Med.* 2011;17:1231-4.
- [97] Boyle WJ, Simonet WS, Lacey DL. Osteoclast differentiation and activation. *Nature* 2003;423:337-42.
- [98] Hadjidakis DJ, Androulakis II. Bone remodeling. *Ann. N. Y. Acad. Sci.* 2006;1092:385-96.
- [99] Kennedy OD, Herman BC, Laudier DM, Majeska RJ, Sun HB, Schaffler MB. Activation of resorption in fatigue-loaded bone involves both apoptosis and active pro-osteoclastogenic signaling by distinct osteocyte populations. *Bone* 2012;50:1115-22.
- [100] Kennedy OD, Laudier DM, Majeska RJ, Sun HB, Schaffler MB. Osteocyte apoptosis is required for production of osteoclastogenic signals following bone fatigue in vivo. *Bone* 2014;64:132-7.

- [101] Burr DB, Forwood MR, Fyhrie DP, Martin RB, Schaffler MB, Turner CH. Bone microdamage and skeletal fragility in osteoporotic and stress fractures. *Journal of Bone and Mineral Research* 1997;12:6-15.
- [102] Hoshaw S, Cody D, Saad A, Fyhrie D. Decrease in canine proximal femoral ultimate strength and stiffness due to fatigue damage. *J. Biomech.* 1997;30:323-9.
- [103] Green JO, Wang J, Diab T, Vidakovic B, Guldborg RE. Age-related differences in the morphology of microdamage propagation in trabecular bone. *J. Biomech.* 2011;44:2659-66.
- [104] Burr DB, Stafford T. Validity of the bulk-staining technique to separate artifactual from in vivo bone microdamage. *Clin. Orthop. Relat. Res.* 1990;(260):305-8.
- [105] Martin RB. Fatigue microdamage as an essential element of bone mechanics and biology. *Calcif. Tissue Int.* 2003;73:101-7.
- [106] Wu Z, LaNeve AJ, Niebur GL. In vivo microdamage is an indicator of susceptibility to initiation and propagation of microdamage in human femoral trabecular bone. *Bone* 2013;55:208-15.
- [107] Legg AT. An obscure affection of the hip-joint. *The Boston Medical and Surgical Journal* 1910;162:202-4.
- [108] CALVÉ J. On a particular form of pseudo-coxalgia associated with a characteristic deformity of the upper end of the femur. *Clin. Orthop.* 1980;150:4-7.
- [109] PERTHES GC, Peltier LF. Concerning arthritis deformans juvenilis. *Clin. Orthop.* 1981;158:5-9.
- [110] Wingstrand H. Significance of synovitis in legg-calve-perthes disease. *Journal of Pediatric Orthopaedics B* 1999;8:156-60.
- [111] McAndrew MP, Weinstein S. A long-term follow-up of legg-calvé-perthes disease. *J Bone Joint Surg [Am]* 1984;860-9.

- [112] Larson AN, Sucato DJ, Herring JA, Adolphsen SE, Kelly DM, Martus JE et al. A prospective multicenter study of legg-calvé-perthes Disease Functional and radiographic outcomes of nonoperative treatment at a mean follow-up of twenty years. *The Journal of Bone & Joint Surgery* 2012;94:584-92.
- [113] Shah H. Perthes disease: Evaluation and management. *Orthop. Clin. North Am.* 2014;45:87-97.
- [114] Waldenström H. The definite form of the coxa plana. *Acta Radiol.* 1922;384-94.
- [115] Waldenström H. The first stages of coxa plana. *The Journal of Bone & Joint Surgery* 1938;20:559-66.
- [116] Kim HK, Herring JA. Pathophysiology, classifications, and natural history of perthes disease. *Orthop. Clin. North Am.* 2011;42:285-95.
- [117] BROWN TD, WAY ME, FERGUSON AB. Mechanical characteristics of bone in femoral capital aseptic necrosis. *Clin. Orthop.* 1981;156:240-7.
- [118] Brown T, Hild G. Pre-collapse stress redistributions in femoral head osteonecrosis—a three-dimensional finite element analysis. *J. Biomech. Eng.* 1983;105:171-6.
- [119] Yang J, Koo K, Lee M, Yang P, Noh MD, Kim S et al. Mechanics of femoral head osteonecrosis using three-dimensional finite element method. *Arch. Orthop. Trauma Surg.* 2002;122:88-92.
- [120] Pharr G, Oliver W. Measurement of thin film mechanical properties using nanoindentation. *MRS Bull* 1992;17:28-33.
- [121] Nix WD. Elastic and plastic properties of thin films on substrates: Nanoindentation techniques. *Materials Science and Engineering: A* 1997;234:37-44.

- [122] Gouldstone A, Koh H, Zeng K, Giannakopoulos A, Suresh S. Discrete and continuous deformation during nanoindentation of thin films. *Acta Materialia* 2000;48:2277-95.
- [123] Saha R, Nix WD. Effects of the substrate on the determination of thin film mechanical properties by nanoindentation. *Acta Materialia* 2002;50:23-38.
- [124] Briscoe B, Fiori L, Pelillo E. Nano-indentation of polymeric surfaces. *J. Phys. D* 1998;31:2395.
- [125] VanLandingham M.R., J.S. Villarrubia, W.F. Guthrie, G.F. Meyers, Nanoindentation of polymers: An overview. 167 (2001) 15-44.
- [126] Ebenstein DM, Pruitt LA. Nanoindentation of biological materials. *Nano Today* 2006;1:26-33.
- [127] Oyen ML. Nanoindentation hardness of mineralized tissues. *J. Biomech.* 2006;39:2699-702.
- [128] Franke O, Durst K, Maier V, Göken M, Birkholz T, Schneider H et al. Mechanical properties of hyaline and repair cartilage studied by nanoindentation. *Acta Biomaterialia* 2007;3:873-81.
- [129] McKee CT, Last JA, Russell P, Murphy CJ. Indentation versus tensile measurements of young's modulus for soft biological tissues. *Tissue Engineering Part B: Reviews* 2011;17:155-64.
- [130] Rho JY, Tsui TY, Pharr GM. Elastic properties of human cortical and trabecular lamellar bone measured by nanoindentation. *Biomaterials* 1997;18:1325-30.
- [131] Zysset PK, Guo XE, Hoffer CE, Moore KE, Goldstein SA. Elastic modulus and hardness of cortical and trabecular bone lamellae measured by nanoindentation in the human femur. *J. Biomech.* 1999;32:1005-12.

- [132] Hengsberger S, Kulik A, Zysset P. A combined atomic force microscopy and nanoindentation technique to investigate the elastic properties of bone structural units. *Eur Cell Mater* 2001;1:12-7.
- [133] Hengsberger S, Kulik A, Zysset P. Nanoindentation discriminates the elastic properties of individual human bone lamellae under dry and physiological conditions. *Bone* 2002;30:178-84.
- [134] Hoffler CE, Guo XE, Zysset PK, Goldstein SA. An application of nanoindentation technique to measure bone tissue lamellae properties. *J. Biomech. Eng.* 2005;127:1046-53.
- [135] Milovanovic P, Potocnik J, Djonic D, Nikolic S, Zivkovic V, Djuric M et al. Age-related deterioration in trabecular bone mechanical properties at material level: Nanoindentation study of the femoral neck in women by using AFM. *Exp. Gerontol.* 2012;47:154-9.
- [136] Albert C, Jameson J, Toth JM, Smith P, Harris G. Bone properties by nanoindentation in mild and severe osteogenesis imperfecta. *Clin. Biomech.* 2013;28:110-6.
- [137] Maruyama N, Shibata Y, Mochizuki A, Yamada A, Maki K, Inoue T et al. Bone micro-fragility caused by the mimetic aging processes in α -klotho deficient mice: In situ nanoindentation assessment of dilatational bands. *Biomaterials* 2015;47:62-71.
- [138] Kim G, Cole JH, Boskey AL, Baker SP, van der Meulen, Marjolein CH. Reduced tissue-level stiffness and mineralization in osteoporotic cancellous bone. *Calcif. Tissue Int.* 2014;95:125-31.
- [139] Wang C, Wang X, Xu X, Yuan X, Gou W, Wang A et al. Bone microstructure and regional distribution of osteoblast and osteoclast activity in the osteonecrotic femoral head. *PloS one* 2014;9:e96361.

- [140] Mullins L, Sassi V, McHugh P, Bruzzi M. Differences in the crack resistance of interstitial, osteonal and trabecular bone tissue. *Ann. Biomed. Eng.* 2009;37:2574-82.
- [141] Zysset PK. Indentation of bone tissue: A short review. *Osteoporos. Int.* 2009;20:1049-55.
- [142] Y. Leng, *Materials characterization: Introduction to microscopic and spectroscopic methods*, John Wiley & Sons, 2009.
- [143] Rey C, Collins B, Goehl T, Dickson I, Glimcher M. The carbonate environment in bone mineral: A resolution-enhanced fourier transform infrared spectroscopy study. *Calcif. Tissue Int.* 1989;45:157-64.
- [144] Rey C, Renugopalakrishnan V, Collins B, Glimcher MJ. Fourier transform infrared spectroscopic study of the carbonate ions in bone mineral during aging. *Calcif. Tissue Int.* 1991;49:251-8.
- [145] Penner-Hahn JE. X-ray absorption spectroscopy. eLS.
- [146] Smith R, Rehman I. Fourier transform raman spectroscopic studies of human bone. *J. Mater. Sci. Mater. Med.* 1994;5:775-8.
- [147] Freeman J, Wopenka B, Silva M, Pasteris J. Raman spectroscopic detection of changes in bioapatite in mouse femora as a function of age and in vitro fluoride treatment. *Calcif. Tissue Int.* 2001;68:156-62.
- [148] Wopenka B, Pasteris JD. A mineralogical perspective on the apatite in bone. *Materials Science and Engineering: C* 2005;25:131-43.
- [149] Reiche I, Chalmin E. Synchrotron radiation and cultural heritage: Combined XANES/XRF study at mn K-edge of blue, grey or black coloured palaeontological and archaeological bone material. *J. Anal. At. Spectrom.* 2008;23:799-806.

- [150] Bazin D, Daudon M, Chappard C, Rehr J, Thiaudiere D, Reguer S. The status of strontium in biological apatites: An XANES investigation. *Journal of synchrotron radiation* 2011;18:912-8.
- [151] Frankær CG, Raffalt AC, Stahl K. Strontium localization in bone tissue studied by X-ray absorption spectroscopy. *Calcif. Tissue Int.* 2014;94:248-57.
- [152] Newville M. Fundamentals of XAFS. *Reviews in Mineralogy and Geochemistry* 2014;78:33-74.
- [153] Tang Y, Chappell HF, Dove MT, Reeder RJ, Lee YJ. Zinc incorporation into hydroxylapatite. *Biomaterials* 2009;30:2864-72.
- [154] Carpentier X, Bazin D, Jungers P, Reguer S, Thiaudière D, Daudon M. The pathogenesis of randall's plaque: A papilla cartography of ca compounds through an ex vivo investigation based on XANES spectroscopy. *Journal of synchrotron radiation* 2010;17:374-9.
- [155] Rajendran J, Gialanella S, Aswath PB. XANES analysis of dried and calcined bones. *Materials Science and Engineering: C* 2013;33:3968-79.
- [156] Nyman JS, Lynch CC, Perrien DS, Thiolloy S, O'Quinn EC, Patil CA et al. Differential effects between the loss of MMP-2 and MMP-9 on structural and tissue-level properties of bone. *Journal of Bone and Mineral Research* 2011;26:1252-60.
- [157] Carpentier VT, Wong J, Yeap Y, Gan C, Sutton-Smith P, Badiei A et al. Increased proportion of hypermineralized osteocyte lacunae in osteoporotic and osteoarthritic human trabecular bone: Implications for bone remodeling. *Bone* 2012;50:688-94.
- [158] Meirer F, Pemmer B, Pepponi G, Zoeger N, Wobrauschek P, Sprio S et al. Assessment of chemical species of lead accumulated in tidemarks of human articular cartilage by X-ray absorption near-edge structure analysis. *Journal of synchrotron radiation* 2011;18:238-44.

- [159] Imbert L, Aurégan J, Pernelle K, Hoc T. Mechanical and mineral properties of osteogenesis imperfecta human bones at the tissue level. *Bone* 2014;65:18-24.
- [160] Taylor D, Hazenberg JG, Lee TC. Living with cracks: Damage and repair in human bone. *Nat. Mater.* 2007;6:263-8.
- [161] Nishii T, Sugano N, Ohzono K, Sakai T, Sato Y, Yoshikawa H. Significance of lesion size and location in the prediction of collapse of osteonecrosis of the femoral head: A new three-dimensional quantification using magnetic resonance imaging. *J. Orthop. Res.* 2002;20:130-6.
- [162] Volokh KY, Yoshida H, Leali A, Fetto JF, Chao EY. Prediction of femoral head collapse in osteonecrosis. *J. Biomech. Eng.* 2006;128:467-70.
- [163] Burr DB, Turner CH, Naick P, Forwood MR, Ambrosius W, Hasan MS et al. Does microdamage accumulation affect the mechanical properties of bone? *J. Biomech.* 1998;31:337-45.
- [164] Nagaraja S, Lin AS, Guldborg RE. Age-related changes in trabecular bone microdamage initiation. *Bone* 2007;40:973-80.
- [165] Chapurlat RD, Delmas PD. Bone microdamage: A clinical perspective. *Osteoporos. Int.* 2009;20:1299-308.
- [166] Kothapalli R, Aya-ay JP, Bian H, Garces A, Kim HKW. Ischaemic injury to femoral head induces apoptotic and oncotic cell death. *Pathology* 2007;39:241-6.
- [167] Kim HKW, Su PH, Qiu YS. Histopathologic changes in growth-plate cartilage following ischemic necrosis of the capital femoral epiphysis. an experimental investigation in immature pigs. *J. Bone Joint Surg. Am.* 2001;83-A:688-97.
- [168] Lee TC, Arthur TL, Gibson LJ, Hayes WC. Sequential labelling of microdamage in bone using chelating agents. *J. Orthop. Res.* 2000;18:322-5.

- [169] Martin RB, Yeh OC, Fyhrie DP. On sampling bones for microcracks. *Bone* 2007;40:1159-65.
- [170] Allen MR, Iwata K, Phipps R, Burr DB. Alterations in canine vertebral bone turnover, microdamage accumulation, and biomechanical properties following 1-year treatment with clinical treatment doses of risedronate or alendronate. *Bone* 2006;39:872-9.
- [171] Allen MR, Iwata K, Sato M, Burr DB. Raloxifene enhances vertebral mechanical properties independent of bone density. *Bone* 2006;39:1130-5.
- [172] Wenzel TE, Schaffler MB, Fyhrie DP. In vivo trabecular microcracks in human vertebral bone. *Bone* 1996;19:89-95.
- [173] Schaffler MB, Choi K, Milgrom C. Aging and matrix microdamage accumulation in human compact bone. *Bone* 1995;17:521-5.
- [174] Paietta RC, Campbell SE, Ferguson VL. Influences of spherical tip radius, contact depth, and contact area on nanoindentation properties of bone. *J. Biomech.* 2011;44:285-90.
- [175] Mulder L, Koolstra JH, den Toonder JM, van Eijden TM. Intratrabecular distribution of tissue stiffness and mineralization in developing trabecular bone. *Bone* 2007;41:256-65.
- [176] Gupta HS, Stachewicz U, Wagermaier W, Roschger P, Wagner HD, Fratzl P. Mechanical modulation at the lamellar level in osteonal bone. *J. Mater. Res.* 2006;21:1913-21.
- [177] Huitema LF, Vaandrager AB. What triggers cell-mediated mineralization? *Front. Biosci.* 2007;12:2631-45.
- [178] Allen MR, Burr DB. Mineralization, microdamage, and matrix: How bisphosphonates influence material properties of bone. *IBMS BoneKEy* 2007;4:49-60.

- [179] Bushby AJ, Ferguson VL, Boyde A. Nanoindentation of bone: Comparison of specimens tested in liquid and embedded in polymethylmethacrylate. *J. Mater. Res.* 2004;19:249 <last_page> 259.
- [180] Boyde A. The real response of bone to exercise. *J. Anat.* 2003;203:173-89.
- [181] Conzemius MG, Brown TD, Zhang Y, Robinson RA. A new animal model of femoral head osteonecrosis: One that progresses to human-like mechanical failure. *Journal of Orthopaedic Research* 2002;20:303-9.
- [182] Norman D, Reis D, Zinman C, Misselevich I, Boss JH. Vascular deprivation-induced necrosis of the femoral head of the rat. an experimental model of avascular osteonecrosis in the skeletally immature individual or legg-perthes disease. *Int. J. Exp. Pathol.* 1998;79:173-81.
- [183] Rowe SM, Lee JJ, Chung JY, Moon ES, Song EK, Seo HY. Deformity of the femoral head following vascular infarct in piglets. *Acta orthopaedica* 2006;77:33-8.
- [184] Kim HKW, Aruwajoye O, Stetler J, Stall A. Effects of non-weight-bearing on the immature femoral head following ischemic OsteonecrosisAn experimental investigation in immature pigs. *The Journal of Bone & Joint Surgery* 2012;94:2228-37.
- [185] Yerramshetty JS, Akkus O. The associations between mineral crystallinity and the mechanical properties of human cortical bone. *Bone* 2008;42:476-82.
- [186] Awonusi A, Morris MD, Tecklenburg MM. Carbonate assignment and calibration in the raman spectrum of apatite. *Calcif. Tissue Int.* 2007;81:46-52.
- [187] Morris MD, Mandair GS. Raman assessment of bone quality. *Clinical Orthopaedics and Related Research* 2011;469:2160-9.
- [188] Dessombz A, Nguyen C, Ea H, Rouzière S, Foy E, Hannouche D et al. Combining μ X-ray fluorescence, μ XANES and μ XRD to shed light on Zn^{2+} cations in cartilage and

meniscus calcifications. *Journal of Trace Elements in Medicine and Biology* 2013;27:326-33.

[189] Bazin D, Chappard C, Combes C, Carpentier X, Rouzière S, André G et al. Diffraction techniques and vibrational spectroscopy opportunities to characterise bones. *Osteoporosis Int.* 2009;20:1065-75.

[190] Bazin D, Daudon M, Combes C, Rey C. Characterization and some physicochemical aspects of pathological microcalcifications. *Chem. Rev.* 2012;112:5092-120.

[191] Demirkiran H, Hu Y, Zuin L, Appathurai N, Aswath PB. XANES analysis of calcium and sodium phosphates and silicates and hydroxyapatite–Bioglass® 45S5 co-sintered bioceramics. *Materials Science and Engineering: C* 2011;31:134-43.

[192] Crane NJ, Morris MD, Ignelzi MA, Yu G. Raman imaging demonstrates FGF2-induced craniosynostosis in mouse calvaria. *J. Biomed. Opt.* 2005;10:031119-0311198.

[193] Draper ER, Morris MD, Camacho NP, Matousek P, Towrie M, Parker AW et al. Novel assessment of bone using Time-Resolved transcutaneous raman spectroscopy. *Journal of Bone and Mineral Research* 2005;20:1968-72.

[194] Pasteris JD, Wopenka B, Freeman JJ, Rogers K, Valsami-Jones E, van der Houwen, Jacqueline AM et al. Lack of OH in nanocrystalline apatite as a function of degree of atomic order: Implications for bone and biomaterials. *Biomaterials* 2004;25:229-38.

[195] Driessens F. The mineral in bone, dentin and tooth enamel. *Bulletin des sociétés chimiques belges* 1980;89:663-89.

[196] Paschalis E, DiCarlo E, Betts F, Sherman P, Mendelsohn R, Boskey A. FTIR microspectroscopic analysis of human osteonal bone. *Calcif. Tissue Int.* 1996;59:480-7.

- [197] Yeni Y, Yerramshetty J, Akkus O, Pechey C, Les C. Effect of fixation and embedding on raman spectroscopic analysis of bone tissue. *Calcif. Tissue Int.* 2006;78:363-71.
- [198] Akkus O, Adar F, Schaffler MB. Age-related changes in physicochemical properties of mineral crystals are related to impaired mechanical function of cortical bone. *Bone* 2004;34:443-53.
- [199] Penel G, Leroy G, Rey C, Bres E. MicroRaman spectral study of the PO₄ and CO₃ vibrational modes in synthetic and biological apatites. *Calcif. Tissue Int.* 1998;63:475-81.
- [200] Ito A, Maekawa K, Tsutsumi S, Ikazaki F, Tateishi T. Solubility product of OH-carbonated hydroxyapatite. *J. Biomed. Mater. Res.* 1997;36:522-8.
- [201] Sydney-Zax M, Mayer I, Deutsch D. Carbonate content in developing human and bovine enamel. *J. Dent. Res.* 1991;70:913-6.
- [202] Sa Y, Liang S, Ma X, Lu S, Wang Z, Jiang T et al. Compositional, structural and mechanical comparisons of normal enamel and hypomaturation enamel. *Acta biomaterialia* 2014;10:5169-77.
- [203] Xiao Y, Xiang L, Shao J. Bone morphogenetic protein. *Biochem. Biophys. Res. Commun.* 2007;362:550-3.
- [204] Bragdon B, Moseychuk O, Saldanha S, King D, Julian J, Nohe A. Bone morphogenetic proteins: A critical review. *Cell. Signal.* 2011;23:609-20.
- [205] Zhou L, Yoon SJ, Jang KY, Moon YJ, Wagle S, Lee KB et al. COMP-Angiopoietin1 potentiates the effects of bone morphogenic protein-2 on ischemic necrosis of the femoral head in rats. 2014;.
- [206] Simank H, Manggold J, Sebald W, Ries R, Richter W, Ewerbeck V et al. Bone morphogenetic protein-2 and growth and differentiation factor-5 enhance the healing of necrotic bone in a sheep model. *Growth Factors* 2001;19:247-57.

- [207] Welch RD, Jones AL, Bucholz RW, Reinert CM, Tjia JS, Pierce WA et al. Effect of recombinant human bone morphogenetic protein-2 on fracture healing in a goat tibial fracture model. *Journal of Bone and Mineral Research* 1998;13:1483-90.
- [208] Bax B, Wozney J, Ashhurst D. Bone morphogenetic protein-2 increases the rate of callus formation after fracture of the rabbit tibia. *Calcif. Tissue Int.* 1999;65:83-9.
- [209] Schmidmaier G, Wildemann B, Cromme F, Kandziora F, Haas N, Raschke M. Bone morphogenetic protein-2 coating of titanium implants increases biomechanical strength and accelerates bone remodeling in fracture treatment: A biomechanical and histological study in rats. *Bone* 2002;30:816-22.
- [210] Einhorn TA, Majeska RJ, Mohaideen A, Kagel EM, Bouxsein ML, Turek TJ et al. A single percutaneous injection of recombinant human bone morphogenetic protein-2 accelerates fracture repair. *J. Bone Joint Surg. Am.* 2003;85-A:1425-35.
- [211] Rodan GA, Fleisch HA. Bisphosphonates: Mechanisms of action. *J. Clin. Invest.* 1996;97:2692.
- [212] Fleisch H. Bisphosphonates: Mechanisms of action. *Endocr. Rev.* 1998;19:80-100.
- [213] Drake M.T., B.L. Clarke, S. Khosla, Bisphosphonates: Mechanism of action and role in clinical practice. 83 (2008) 1032-45.
- [214] Kim, HKW., Bian, H., Aya-ay, J., Garces, A., Morgan, E. F., & Gilbert, S. R. . Hypoxia and HIF-1 α expression in the epiphyseal cartilage following ischemic injury to the immature femoral head. *Bone* 2009;45:280-8.
- [215] Liberman UA, Weiss SR, Bröll J, Minne HW, Quan H, Bell NH et al. Effect of oral alendronate on bone mineral density and the incidence of fractures in postmenopausal osteoporosis. *N. Engl. J. Med.* 1995;333:1437-44.
- [216] Fleisch H. Bisphosphonates: Mechanisms of action and clinical use in osteoporosis-an update. *Horm. Metab. Res.* 1997;29:145-50.

- [217] Black DM, Delmas PD, Eastell R, Reid IR, Boonen S, Cauley JA et al. Once-yearly zoledronic acid for treatment of postmenopausal osteoporosis. *N. Engl. J. Med.* 2007;356:1809-22.
- [218] Langston AL, Campbell MK, Fraser WD, MacLennan GS, Selby PL, Ralston SH. Randomized trial of intensive bisphosphonate treatment versus symptomatic management in paget's disease of bone. *Journal of Bone and Mineral Research* 2010;25:20-31.
- [219] Astrand J, Aspenberg P. Systemic alendronate prevents resorption of necrotic bone during revascularization. A bone chamber study in rats. *BMC Musculoskelet. Disord.* 2002;3:19.
- [220] Kaneko H, Arakawa T, Mano H, Kaneda T, Ogasawara A, Nakagawa M et al. Direct stimulation of osteoclastic bone resorption by bone morphogenetic protein (BMP)-2 and expression of BMP receptors in mature osteoclasts. *Bone* 2000;27:479-86.
- [221] Boivin G, Chavassieux P, Santora A, Yates J, Meunier P. Alendronate increases bone strength by increasing the mean degree of mineralization of bone tissue in osteoporotic women. *Bone* 2000;27:687-94.
- [222] Borah B, Ritman EL, Dufresne TE, Jorgensen SM, Liu S, Sacha J et al. The effect of risedronate on bone mineralization as measured by micro-computed tomography with synchrotron radiation: Correlation to histomorphometric indices of turnover. *Bone* 2005;37:1-9.
- [223] Gourion-Arsiquaud S, Faibish D, Myers E, Spevak L, Compston J, Hodsman A et al. Use of FTIR spectroscopic imaging to identify parameters associated with fragility fracture. *Journal of bone and mineral research* 2009;24:1565-71.
- [224] Gourion-Arsiquaud S, Lukashova L, Power J, Loveridge N, Reeve J, Boskey AL. Fourier transform infrared imaging of femoral neck bone: Reduced heterogeneity of

mineral-to-matrix and carbonate-to-phosphate and more variable crystallinity in treatment-naive fracture cases compared with fracture-free controls. *Journal of Bone and Mineral Research* 2013;28:150-61.

[225] McCreddie BR, Morris MD, Chen T, Sudhaker Rao D, Finney WF, Widjaja E et al. Bone tissue compositional differences in women with and without osteoporotic fracture. *Bone* 2006;39:1190-5.

[226] Bala Y, Kohles J, Recker RR, Boivin G. Oral ibandronate in postmenopausal osteoporotic women alters micromechanical properties independently of changes in mineralization. *Calcif. Tissue Int.* 2013;92:6-14.

[227] Tjhia CK, Odvina CV, Rao DS, Stover SM, Wang X, Fyhrie DP. Mechanical property and tissue mineral density differences among severely suppressed bone turnover (SSBT) patients, osteoporotic patients, and normal subjects. *Bone* 2011;49:1279-89.

[228] Shibata Y, Suzuki D, Yamada A, Maruyama N, Fujisawa N, Kamijo R et al. Lysyl oxidase like-2 reinforces unsatisfactory ossification induced by bone morphogenetic protein-2: Relating nanomechanical properties and molecular changes. *Nanomedicine: Nanotechnology, Biology and Medicine* 2013;9:1036-47.

[229] Madhurakkat Perikamana SK, Lee J, Ahmad T, Jeong Y, Kim D, Kim K et al. Effects of immobilized BMP-2 and nanofiber morphology on in vitro osteogenic differentiation of hMSCs and in vivo collagen assembly of regenerated bone. *ACS applied materials & interfaces* 2015;7:8798-808.

[230] Tai K, Pelled G, Sheyn D, Bershteyn A, Han L, Kallai I et al. Nanobiomechanics of repair bone regenerated by genetically modified mesenchymal stem cells. *Tissue Engineering Part A* 2008;14:1709-20.

Biographical Information

Olumide Aruwajoye received his Bachelor of Science in Biomedical Engineering from Tulane University in New Orleans, Louisiana and later a Master of Science in Biomedical Engineering at the University of Texas at Arlington. He began his PhD studies in Materials Science and Engineering in a collaborative effort between Texas Scottish Rite Hospital and University of Texas at Arlington. His research interests include orthopedic and biomaterials research.